Characterization of the TJ-Monopix2 Depleted Monolithic Active Pixel Sensor for High-Energy Physics Experiments

Dissertation
zur
Erlangung des Doktorgrades (Dr. rer. nat.)
der
Mathematisch-Naturwissenschaftlichen Fakultät
der
Rheinischen Friedrich-Wilhelms-Universität Bonn

vorgelegt von
Christian Bespin Valero
aus
Mechernich

Bonn 2024

Angefertigt mit Genehmigung der Mathematisch-Naturwissenschaftlichen Fakultät
der Rheinischen Friedrich-Wilhelms-Universität Bonn

Gutachter/Betreuer: Prof. Dr. Jochen Dingfelder
Gutachter: Prof. Dr. Florian Bernlochner

Tag der Promotion: 17. Oktober 2024
Erscheinungsjahr: 2024

Contents

1 Introduction

The quest for understanding the fundamental building blocks of the universe and their interactions has been a constant motivation in the field of particle physics. The Standard Model of particle physics has developed over time and categorizes the known elementary constituents of matter and their interactions. While it has been validated with high precision in many measurements, it does not include observed physical phenomena such as neutrino masses and oscillations, and the extent of matter-antimatter asymmetry. After the discovery of the Higgs boson, the Standard Model is the most accurate and consistent theory up to high energies. A significant part of modern particle physics involves probing the Standard Model with increasing precision and searching for *physics beyond the Standard Model* (BSM). To date, no BSM physics have been observed on the probed energy scale, and further studies require an expansion of the energy frontier to well above 1 TeV. At the same time, the observation of rare processes can challenge the Standard Model at the lower end of the energy scale but demands high-intensity particle beams for measurements at very high precision.

The largest accelerator to date is the Large Hadron Collider (LHC), situated at the European Organization for Nuclear Research (CERN). Protons are accelerated and brought to collision, and in four large experiments, the properties of the final state particles are measured. This includes their trajectory, energy, and momentum. To increase the energy range and intensity of particle accelerators, upgrades to existing facilities (High-Luminosity LHC) and the construction of new accelerators (Future Circular Collider or Circular Electron Positron Collider) are proposed.

The operating conditions at accelerator experiments pose strict requirements for the detector components. Pixel detectors, which are typically located close to the interaction point, are subject to the harshest environments in terms of particle rate and the level of radiation. Their objective is tracking particles to reconstruct the production and decay vertices. Semiconductor detectors offer a large and fast signal and high granularity compared with gaseous detectors, resulting in better separation of particle tracks in space and time. They can be engineered to achieve tolerance to the high radiation levels close to the interaction point of the particle beams and are the state-of-the-art solution for tracking detectors at collider experiments.

So-called hybrid pixel detectors that employ a readout ASIC (application specific integrated circuit) in a separate entity from the charge-sensitive silicon bulk with an electrically conducting interconnection are today's standard for the harshest environments concerning particle rates and radiation, such as at the ATLAS and CMS experiments at CERN. The progress in semiconductor

technologies has fueled efforts to combine the aforementioned components of a pixel detector in one entity. These monolithic pixel detectors do not require a cost-intensive interconnection step and use less material. This reduces the influence on the energy and trajectory of the particle due to reduced energy loss and scattering in insensitive material. The monolithic approach also facilitates the tracking of very low-energy particles that was previously not possible. A great deal of effort is necessary to design such devices for levels of radiation hardness expected after the high-luminosity upgrade of the LHC (HL-LHC), while offering high granularity, low power consumption, and fast readout speed.

TJ-Monopix is a series of prototypes of monolithic pixel detectors, originally designed for the ATLAS Inner Tracker (ITk) outer pixel layer for the HL-LHC phase, planned to start in 2029. The prototypes are produced in a commercial CMOS imaging technology offering large-volume production and fast turnaround time. Both TJ-Monopix1 and TJ-Monopix2 use a depleted high-resistive silicon substrate for enhanced charge collection, and electronics integrated in each pixel, rendering it a *depleted monolithic active pixel sensor* (DMAPS). Charge collection by drift in depleted silicon enhances the radiation hardness and yields a fast response. The sensor geometry of TJ-Monopix minimizes the input capacitance of the readout circuitry, which facilitates a low power consumption of the electronics. Special care has been taken to establish a tolerance to the radiation levels of the ITk outer pixel layer. This work investigates the radiation hardness of TJ-Monopix1 with an optimized sensor geometry and characterizes the latest prototype, TJ-Monopix2, for usage in high-energy collider experiments. It includes the design of the digital periphery of TJ-Monopix2 and the development of the custom data acquisition system on hardware, firmware, and software levels.

Chapter 2 introduces the principles of particle interactions with matter and semiconductor fundamentals. Additionally, an overview of the causes of radiation damage and the observable effects in silicon pixel detectors is given. Different semiconductor particle detector concepts are introduced in Chapter 3, ranging from microstrip detectors to depleted monolithic active pixel sensors. The design of TJ-Monopix2 is presented in Chapter 4, highlighting the analog circuitry in the pixel as well as the digital periphery that was designed within this work. The chapter concludes with an overview of the developed data acquisition system. Test beam campaigns are an integral part of this thesis and their measurement principle is discussed in Chapter 5, before results on the radiation hardness of the current TJ-Monopix sensor geometry are shown in Chapter 6. The characterization of TJ-Monopix2 is addressed in Chapter 7, ranging from studies on its power consumption to the front-end performance and showing hit detection efficiencies of different non-irradiated samples. Finally, the timing performance of the analog front-end as well as the overall time resolution as measured in the laboratory and in particle beams is presented. Chapter 8 gives a conclusion of the studied performance of TJ-Monopix2 and an outlook into further research and development of its design.

2 Principles of silicon pixel detectors

To understand the working principles of silicon pixel detectors, this chapter starts with an introduction to the interaction of particles with matter and how measurable signals are produced. The working principles of semiconductor particle detectors with pn junctions are presented in Section 2.2, and the generation of measurable signals is discussed. At the end of this chapter, radiation damage mechanisms that affect the detector characteristics and pose a challenge for operation in high-rate environments, such as collider experiments are introduced.

2.1 Interaction of particles with matter

Charged and neutral particles are detected through their interactions with matter. Different interaction processes play roles in the detection process: charged particles can ionize and excite atoms, scatter, or produce bremsstrahlung when passing through the electric field of an atomic nucleus. In contrast, photons interact via scattering, absorption, and conversion.

2.1.1 Energy loss of charged particles

Charged particles lose energy when passing through matter due to ionization and excitation of the atoms in the medium, which is the predominant contribution to the energy loss up to very high velocities. Since the energy loss is a consequence of many interactions, it will be described as an average loss per path length with the *Bethe-Bloch formula* [1, 2]. The energy loss depends on the cross section σ_A of the interaction process in the material and the mass M and velocity β of the particle:

$$\left\langle \frac{\mathrm{d}E}{\mathrm{d}x} \right\rangle = n_e \int_{T_\mathrm{min}}^{T_\mathrm{max}} T \frac{\mathrm{d}\sigma_A}{\mathrm{d}T} \left(M, \beta, T\right) \mathrm{d}T \,. \tag{2.1}$$

In the above formula, T denotes the energy transfer to the atom and n_e the target electron density. Often, the energy loss is divided by the mass density of the material and then referred to as *stopping power*. Its unit is $\mathrm{MeV\,cm^2\,g^{-1}}$, which can be used to distinguish actual energy loss and stopping power since the designation $\left\langle \frac{\mathrm{d}E}{\mathrm{d}x} \right\rangle$ is commonly used for both quantities. The relevant interaction is of an electromagnetic nature between the incident particle and the atoms of the material. Up to the first order, the interaction process can be described as Rutherford scattering off a shell electron, which leads to both ionization and excitation. Inserting the cross

section into formula (2.1) yields [3]:

$$\left\langle \frac{\mathrm{d}E}{\mathrm{d}x} \right\rangle = 4\pi N_A r_e^2 m_e c^2 \cdot \frac{Z}{A}\rho\frac{z^2}{\beta^2}\left[\frac{1}{2}\ln\frac{2m_e c^2\beta^2\gamma^2 T_{\max}}{I^2} - \beta^2 - \frac{\delta(\beta\gamma)}{2} - \frac{C(\beta\gamma, I)}{Z}\right]. \quad (2.2)$$

The variables are defined as follows:

r_e, m_e	Classical electron radius and mass
Z, A	Atomic number and mass number of the material
ρ	Mass density of the material
z, β	Charge and velocity of the traversing particle
I	Mean excitation energy of the material
$T_{\max}$	Maximum possible energy transfer to the shell electron
δ, C	Density and shell correction functions, relevant for high energies and small β, respectively

The stopping power for electrons and protons in silicon, depending on $\beta\gamma = \frac{p}{m}$, is shown in Figure 2.1. Since the period during which a particle can interact with the shell electron depends

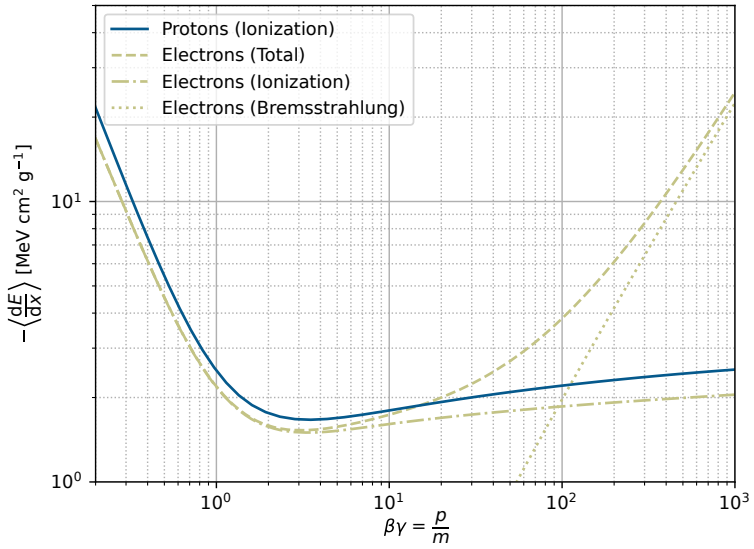

Figure 2.1: Energy loss for protons and electrons in silicon. Proton data is calculated according to (2.2) without shell corrections. The density correction parameterization is taken from [4]. Electron data is taken from ESTAR [5]. Also depicted is the contribution from radiative losses (bremsstrahlung) to the stopping power of electrons.

on its velocity, the average energy loss initially drops proportionally to $1/\beta^2$ until $\beta\gamma = 3 - 4$, where it reaches a minimum of about $1-2\,\mathrm{MeV\,cm^2\,g^{-1}}$. Particles in this energy range are referred to as *minimum-ionizing particles* (MIP). After this minimum with, increasing energy,

the energy loss increases due to (1) the increase of $T_{\max}$ and (2) an increase of the transverse electric field that extends the interaction range of the projectile and shell electron. However, the latter is damped by the screening effect of atomic shells that is included in the density correction function δ in (2.2). Due to the relatively small increase of the energy loss at $\beta\gamma \gtrsim 4$, all particles in this regime are usually also referred to as minimum-ionizing particles. For interactions of electrons and positrons in matter, one has to include spin effects and the nature of the interacting particles (e^-e^-, e^+e^-), among others. Additionally, positrons can undergo annihilation with the shell electrons. A modified Bethe-Bloch formula for the corresponding energy loss, taking into account all these effects, can be found in [3].

2.1.1.1 Bremsstrahlung and δ-electrons

Another mechanism of energy loss is bremsstrahlung, which occurs when a charged particle scatters off the Coulomb field of the nucleus and emits photons. In this process, the energy loss scales with $Z^2 \frac{E}{m^2}$ [6] and becomes relevant at high $\beta\gamma$ and for light particles, such as electrons and positrons. It is well visible in Figure 2.1, where the different contributions for ionization and bremsstrahlung to the energy loss of electrons are depicted. The radiative energy loss by bremsstrahlung can be quantified as:

$$\left(\frac{\mathrm{d}E}{\mathrm{d}x}\right)_{\mathrm{rad}} = -\frac{E}{X_0}\,, \tag{2.3}$$

where X_0 is the radiation length. Integration yields an exponential function:

$$E\,(x) = E_0\,\exp\left(-\frac{x}{X_0}\right)\,, \tag{2.4}$$

indicating that X_0 is defined as the length after which a particle's energy is reduced to $\frac{1}{e}\,E_0$. The energy at which bremsstrahlung losses start to dominate is defined as the *critical energy* and depends mainly on the nucleus, with roughly $E_{\mathrm{crit}} \propto Z^{-1}$ [4]. Since the high-energy photon emitted in bremsstrahlung has a small absorption probability in thin ($\mathcal{O}\,(100\,\mu\mathrm{m})$) silicon sensors, the deposited energy from that process is very small. If the energy transfer T to the atom is large ($T \gg I$), so-called δ-electrons can be produced. These *high-energy knock-on electrons* are mainly emitted at a large (90°) angle to the incident particle track. As the energy of δ-electrons is in the order of keV, they have a high energy loss along their path and can worsen the spatial resolution of fine-segmented silicon detectors.

2.1.1.2 Restricted energy loss

δ-electrons escaping the detector volume and the small absorption probability of bremsstrahlung photons lead to a loss in detected energy. Therefore, the Bethe-Bloch formula (2.2) is modified

by introducing a maximum energy transfer, $T_{\text{cut}} < T_{\max}$ [3]:

$$\left.\frac{\mathrm{d}E}{\mathrm{d}x}\right|_{W<T_{\text{cut}}} = K\frac{Z}{A}\frac{z^2}{\beta^2}\left[\frac{1}{2}\ln\frac{2m_e c^2\beta^2\gamma^2 T_{\text{cut}}}{I^2} - \frac{\beta^2}{2}\left(1+\frac{T_{\text{cut}}}{T_{\max}}\right) - \frac{\delta\left(\beta\gamma\right)}{2} - \frac{C\left(\beta\gamma, I\right)}{Z}\right] \tag{2.5}$$

with

$$K = 4\pi N_A r_e^2 m_e c^2 \rho\,. \tag{2.6}$$

For high $\beta\gamma$, the energy loss reaches the so-called *Fermi plateau* [7]. Due to their minimal energy loss, minimum-ionizing particles are used for detector characterization and testing, as they represent the majority of particles in high-energy physics experiments and reflect the worst-case scenario for energy deposition.

2.1.1.3 Distribution of energy loss

Although the energy loss is defined as an average energy loss per path length, the actual interaction is a statistical process with many energy transfers that are subject to fluctuations in both the number of transfers N and the individual energy transferred E_n:

$$\delta E = \sum_{n=1}^{N} E_n\,. \tag{2.7}$$

While in thin detectors the number fluctuations are governed by Poisson statistics, the energy fluctuations follow the distribution obtained from the Rutherford cross section that is used in the derivation of (2.2) [8]:

$$\frac{\mathrm{d}\sigma}{\mathrm{d}T} = \frac{2\pi z^2\alpha^2\hbar^2}{\beta^2 m_e}\frac{1}{T^2}\,. \tag{2.8}$$

The cross section exhibits a $1/T^2$ dependency, according to which the most probable transferred energy is close to the minimum one. A small fraction of interactions transfer large energies that lead to a long tail in the energy loss distribution. As high-energy particles can escape the detection volume, it is difficult to sample the end of the tail to gain knowledge of the maximum energy required to calculate the average energy loss described above. The *most probable value* (MPV) of the charge distribution is usually a more useful value to characterize the energy deposition capabilities of a tracking detector. This charge distribution can be described by shifting and scaling a probability distribution function developed by Landau [9]:

$$p(x) = \frac{1}{\pi}\int_0^\infty \exp\left(t\ln t - t\lambda\right)\,\sin\left(\pi t\right)\,\mathrm{d}t \tag{2.9}$$

with:

$$\lambda = \lambda\left(\Delta E_{\text{mpv}}, \xi\right) = \frac{\Delta E - \Delta E_{\text{mpv}}}{\xi} - 0.222\,78\,. \tag{2.10}$$

The parameter λ is a function that relates the energy loss ΔE to the most probable energy loss ΔE_{mpv} and ξ, which is the prefactor in front of the logarithm in (2.2) multiplied by the path length Δx:

$$\xi = \frac{1}{2} K \frac{Z}{A} \frac{z^2}{\beta^2} \Delta x\,. \tag{2.11}$$

With these definitions, the most probable value of the Landau distribution is at $\lambda = -0.222\,78$ and its full width at half maximum is $4.018\,\xi$. A Landau distribution with most probable and average value marked is shown in Figure 2.2. For thin detectors, the shape of the energy

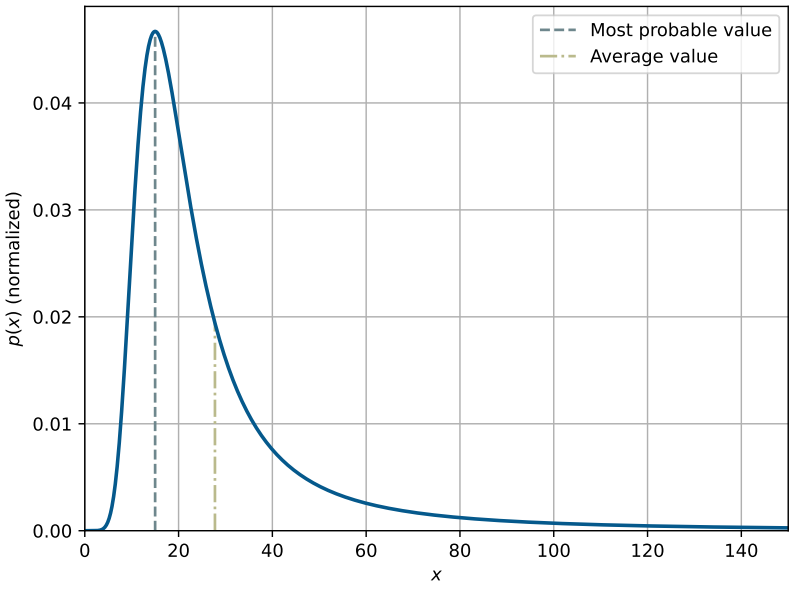

Figure 2.2: Landau probability density function for energy loss fluctuations of ionizing particles. Dashed lines indicate the most probable and average values.

distribution broadens and can no longer be described with a function of the form as in (2.9), but can be approximated well enough for most applications by a convolution of (2.9) with a Gaussian distribution. In silicon pixel detectors, the most probable value of this distribution is generally used to characterize the charge measurements of minimum-ionizing particles.

2.1.2 Energy loss of photons

In the field of particle detection, three different interaction processes of photons with matter are relevant and are discussed in the following. Photons are either absorbed or scattered away from their original direction. Defining an absorption coefficient μ, the number of photons N in a medium can be described with:

$$N(x) = N_0 e^{-\mu x}\,, \tag{2.12}$$

where N_0 is the number of incident photons and x is the depth in the medium. Consequently, the number of photons decreases exponentially when traversing a medium. The underlying processes are:

Photoelectric effect Total energy transfer to an atom with emission of a shell electron

Compton effect Scattering of the photon off an electron

Pair production Conversion into an electron-positron pair in the field of a nucleus

The individual contributions to the total absorption coefficient are plotted in Figure 2.3. In the

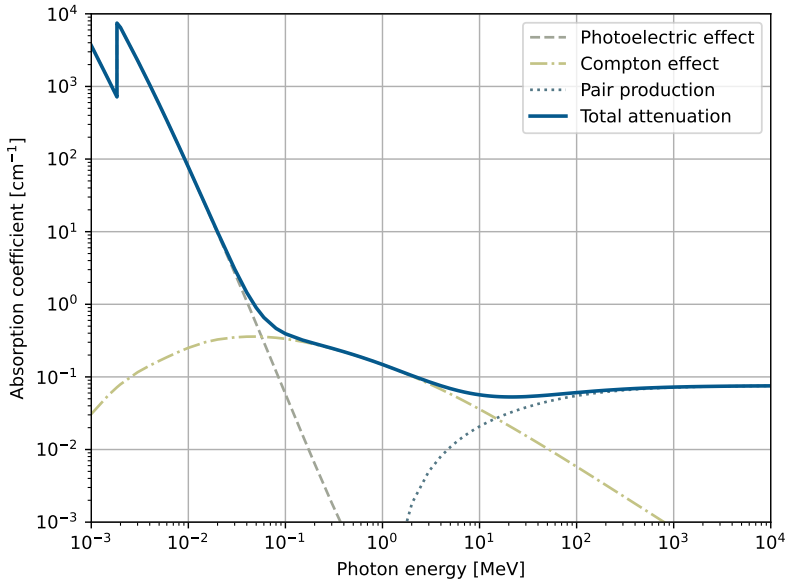

Figure 2.3: Absorption coefficient for photons in silicon with individual contributions from photoelectric effect, Compton effect and pair production. Data from [10].

following, the basic interaction principles and their dependence on photon energy and absorber material are discussed.

2.1.2.1 Photoelectric effect

The photoelectric effect describes the emission of an electron from an atom when a photon is absorbed. In order to release the electron, the photon energy must be higher than the binding energy of the electron, which makes the photoelectric effect the dominant interaction of photons with matter in the $\mathcal{O}\,(\mathrm{keV})$ regime. The emitted electron creates a vacancy in the shell that can be filled by an electron of higher energy which emits a photon with a characteristic energy corresponding to the energy difference of the two electron shells. Those X-ray fluorescence photons can be used for identification of the element or because of their known characteristic energy for calibration purposes.

The characteristics of the photoelectric effect will be discussed in the following. A detailed treatment can be found in [6]. As depicted in Figure 2.4, the cross section for different target

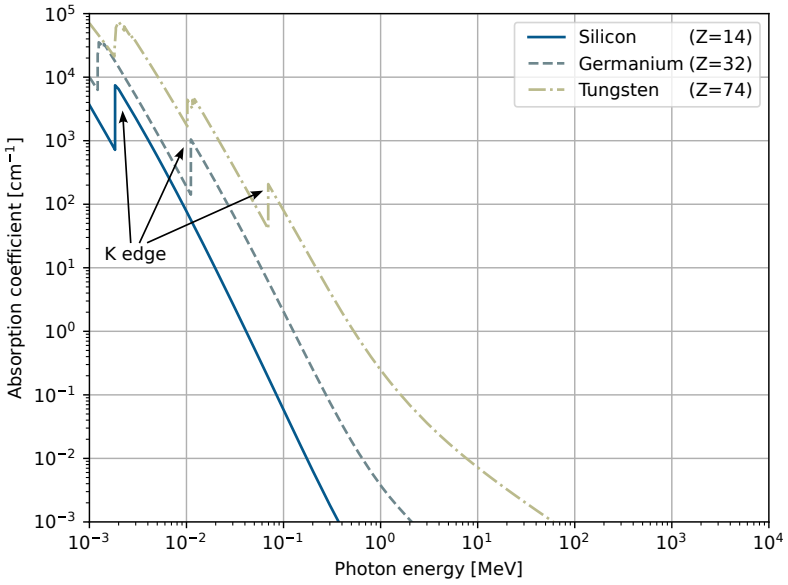

Figure 2.4: Absorption coefficients from photoelectric effect for different target materials with varying atomic number. Data from [10].

materials decreases with increasing photon energy and increases with the atomic number of the target at a fixed photon energy. Sharp edges in the cross section are due to the photon energy exceeding the binding energy of the electron in an inner shell. The energy and Z dependence when treating photon absorption in the K-shell only are:

$$\sigma_{\mathrm{p.e.}} \propto E_\gamma^{-m}\, Z^n \approx E_\gamma^{-3.5}\, Z^{(4-5)}\,. \tag{2.13}$$

Exact values for the exponents m, n depend on the ratio of the binding energy in the K-shell to the transferred kinetic energy. For very high photon energies $E_\gamma \gg m_e$, the dependencies

change to [4]:

$$\sigma_{\text{p.e.}} \propto E_\gamma^{-1} Z^5 \,. \tag{2.14}$$

However, it should be noted from Figure 2.3 that Compton effect and pair production are the dominant interaction processes above $\mathcal{O}(0.1\,\text{MeV})$ where (2.14) holds (see Figure 2.3).

2.1.2.2 Compton effect

The scattering of a photon off a (quasi-)free electron is called the Compton effect. In this process, the electron is kicked out of an atom which results in energy loss and directional change of the photon due to momentum and energy conservation. At low energies, the electron can also stay bound in the atom, which takes the recoil energy and leaves the photon with almost all of its initial energy, independent of the scattering angle.

Following from energy and momentum conservation, the energy of the scattered photon $E_{\gamma,\text{f}}$ depends on the scattering angle θ_γ [4]:

$$E_{\gamma,\text{f}} = \frac{E_{\gamma,\text{i}}}{1 + \frac{E_{\gamma,\text{i}}}{m_e c^2}\,(1 - \cos\theta_\gamma)} \,. \tag{2.15}$$

For a single free electron, the cross section of this process is obtained from quantum electrodynamics (*Klein-Nishina formula*) and is given in [11]. Notably, for incoming photon energies $E_{\gamma,\text{i}} \gg m_e c^2$, the energy dependence of this cross section reduces to:

$$\sigma_C \propto \frac{1}{E_{\gamma,\text{i}}} \,. \tag{2.16}$$

As this relation is derived for a single free electron, it does not take bound electrons in atoms into account. These electrons can only be considered free if the photon energy is substantially larger than the binding energy of the electron. In the case of photon energies higher than the highest binding energy, all the atom's electrons can be considered free. Thus, the cross section per atom scales with the atomic number Z of the element:

$$\sigma_C^{\text{atom}} = \sigma_C Z \,. \tag{2.17}$$

2.1.2.3 Pair production

A photon can convert into an electron-positron pair if it carries enough energy. Because of energy and momentum conservation, the process can only happen in a Coulomb field, where the creating body absorbs the energy. Except for very light elements, pair production usually takes place in the field of a nucleus, and in that case, the recoil can be neglected due to the mass difference. The threshold photon energy for pair production then reduces to two times

the rest mass of an electron and positron:

$$E_\gamma \gtrsim 2m_e c^2 \,. \tag{2.18}$$

Pair production is closely related to the process of bremsstrahlung discussed in Section 2.1. By exchanging the positron in the diagram in Figure 2.5 for a photon, the processes can be

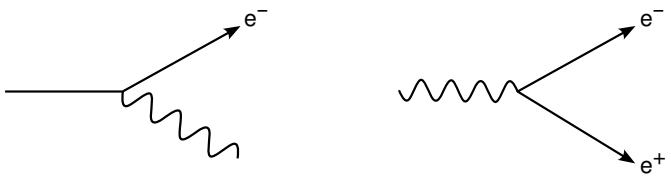

Figure 2.5: Schematic depiction of the bremsstrahlung (left) and pair production (right) processes. The required nucleus is not included.

transformed into each other. Both effects are treated together in [12] and referred to as *Bethe-Heitler processes*. The resulting cross section for pair production can be approximated to [4]:

$$\sigma_{\text{p.p.}} \approx \frac{7}{9}\frac{1}{X_0}\frac{A}{N_A\,\rho}\,, \tag{2.19}$$

where X_0 is the radiation length introduced in (2.3). The formula contains an implicit Z^2 dependence that follows from the coherent sum of Z nucleon charges. As the recoil energy transferred to the nucleus stays small even for large photon energies, most of it is transformed into kinetic energy of the electron and positron. The energy dependence is constant for large E_γ.

2.1.3 Multiple scattering

As described in Section 2.1.1, the interaction of charged particles with matter can be described by Rutherford scattering. The angular characteristics of this scattering process will be discussed in the following. Due to the high energy $E \gg m_e c^2$, the scattering angle in each interaction is small. Multiple interactions during the passage through matter add a statistical effect that describes the angle of the particles afterward. The process is illustrated in Figure 2.6. The angular distribution of the particles behind the scattering material can be described by Molière theory [13]. The angular distribution can be approximated for small angles by a Gaussian function, the width of which describes the projected scattering angle θ_{ms} (onto a plane perpendicular to the incident particle trajectory). A good approximation for θ_{ms} is given by [14]:

$$\theta_{\text{ms}} \approx \frac{13.6\,\text{MeV}}{\beta c p}\, z\sqrt{\frac{x}{X_0}}\left[1 + 0.038\ln\left(\frac{x}{X_0}\frac{z^2}{\beta^2}\right)\right]\,. \tag{2.20}$$

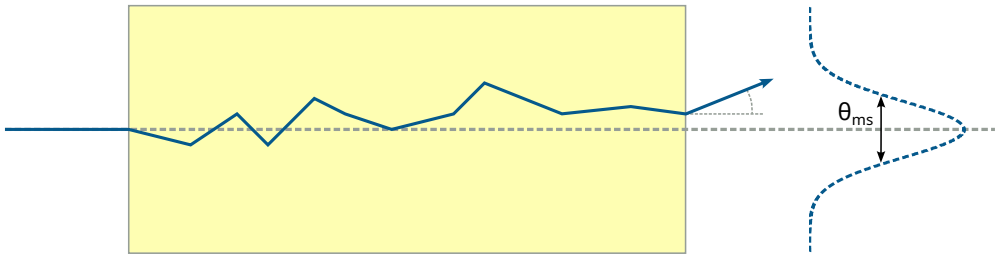

Figure 2.6: Passage of a particle through matter with multiple Coulomb scattering. The probability distribution for the projected angle is approximated by a Gaussian function with width θ_{ms}.

Here, X_0 is the radiation length as defined in (2.3), x is the thickness of the scattering material and z, βc, and p are the charge number, velocity, and momentum of the incident particle. The deflection of the particle must be taken into account for track reconstruction as it worsens the position resolution, particularly for low momenta and high radiation lengths.

2.2 Semiconductor particle detectors

Since the development of microelectronics, complex particle detectors with electronic readout have replaced cloud or bubble chambers as tracking detectors in high-energy physics experiments with high hit rates and requirements on spatial resolution. Ongoing research and developments due to advances in silicon processing technologies establish the position of semiconductor particle detectors as the state-of-the-art solution for the aforementioned purposes.

This section focuses on the materials and detection principle as well as signal formation in semiconductor particle detectors. Additionally, an overview of damages created from exposure to ionizing and non-ionizing radiation is given.

2.2.1 Semiconductor materials

Semiconductor materials are typically crystalline structures, meaning the atoms form a periodic pattern. The Pauli exclusion principle prohibits more than two electrons (of opposite spin) from occupying a single energy level. Due to the periodically overlapping potential wells, each (fully occupied) energy level is shifted by roughly $1 \times 10^{-22}\,\mathrm{eV}$ [15] to satisfy the Pauli exclusion principle. These so-called energy *bands* can be considered as a continuum of allowed energies with forbidden energy gaps in between. Due to the overlapping potential wells, loosely bound electrons can move throughout the crystal along their energy band (see Figure 2.7 (left)). While the lowest band contains tightly bound electrons, the highest one contains no electrons at all. The highest band that still contains electrons is called *valence band* and the lowest one that contains no electrons (at $T = 0\,\mathrm{K}$) *conduction band* [15]. The forbidden energy band between those is referred to as band gap with a gap energy E_g characteristic for each material. From thermal excitations with sufficient energy to overcome the band gap, electrons can move from

the valence band to the conduction band and move freely along the crystal (see Figure 2.7 (right)). The removal of an electron in the valence band leaves a *hole*, which is not a physical

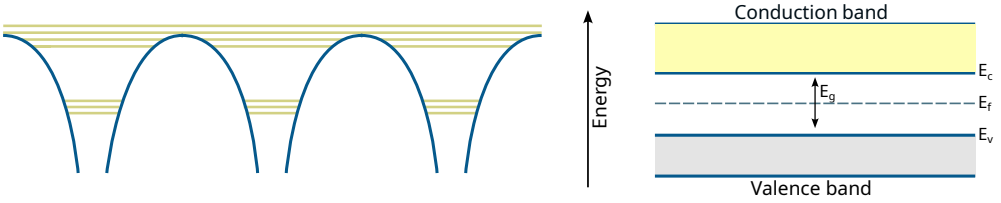

Figure 2.7: Left: energy band structure from overlapping potential wells. Right: naming conventions of energy levels in semiconductors. E_C is the lower edge of the conduction band and E_V the upper edge of the valence band. $E_g = E_C - E_V$ is the gap energy and E_f denotes the Fermi energy. The energy scale is not the same in the left and right figure.

particle but a concept of a missing electron and can also move along the band, carrying a charge of $+e$.

In contrast to metals, the band gap in a semiconductor has a gap energy $E_g > 0$ in the order of $\mathcal{O}(1\,\text{eV})$ [15], e.g. 1.12 eV in silicon or 0.66 eV in germanium at 300 K [4]. Materials with a larger band gap are considered insulators if the thermal excitation at room temperature is not large enough to move an electron across the band gap. In addition to intrinsic semiconductors, combinations of elements, such as SiC or GaAs, can form semiconductors. Most semiconductor devices are fabricated from silicon, which is of essential importance for this work.

To study the electrical characteristics of semiconductors, it is useful to know the electron density n in the conduction band. It can be calculated from the number of allowed states $N(E)$ and the probability $f(E)$ that these are occupied:

$$n = \int_{E_C}^{\infty} N(E) f(E)\,\mathrm{d}E\,, \tag{2.21}$$

where E_C is the energy of the conduction band. The energy at which the occupation probability is 50 % is defined as *Fermi energy* E_f and lies, for silicon at 0 K, in the middle of the band gap between the valence and conduction band. The general occupation probability $f(E)$ for electrons in the conduction band is [16]:

$$f(E) = \frac{1}{1 + e^{(E-E_f)/k_B T}}\,. \tag{2.22}$$

From the effective densities of states N_c and N_v in the conduction and valence bands, respectively, one can calculate the intrinsic charge carrier concentration n_i [17]:

$$n_i = \sqrt{N_c\,N_v}\,e^{-\frac{1}{2}\frac{E_g}{k_B T}}\,. \tag{2.23}$$

2.2.2 Charge creation in a pn junction

The electrical properties of semiconductors can be modified by introducing additional elements in the crystal structure. For silicon, typical elements of those so-called *dopants* are boron, aluminum, phosphorus, or arsenic, which stem from the main groups III and V in the periodic table of elements, next to group IV in which silicon resides. Atoms in group III have one less electron participating in a bond to a neighboring silicon atom. This dangling bond can capture an electron, subsequently leaving a hole behind in the lattice, which can contribute to electrical conduction. Due to the electron-capturing behavior, this type of atom added to the silicon lattice is called *acceptor* and the semiconductor is called *p-doped*. Accordingly, atoms of main group V are called *donors* and introduce an additional electron into the lattice, which can be loosened from the shell by small thermal excitations. They can move freely through the lattice and contribute to electrical conduction. This kind of doping is referred to as *n-type doping*. Donors and acceptors create additional energy levels slightly below the conduction band and slightly above the valence band, respectively.

Bringing n-doped and p-doped silicon into contact with each other creates a *pn junction* with characteristics that make charge detection possible. This chapter only treats so-called homojunctions, where the same semiconductor material is brought into contact, namely silicon. The pn junction produces a diode with rectifying capabilities as it allows for current flow in one direction but not in the other, depending on the sign of the voltage applied to the p- and n-side. With a more positive potential applied at the p-side, the current follows an exponential behavior [18]:

$$I = I_S \left[\exp\left(\frac{eV_{\text{ext}}}{k_B T} \right) - 1 \right] , \tag{2.24}$$

where k_B is the Boltzmann constant and V_{ext} is the externally applied voltage between p and n, and I_S is a constant (reverse saturation current) in the order of $10^{-9} - 10^{-3}$ mA. As described in Section 2.2.1, the Fermi level is constant in thermal equilibrium, which results in a bending of the energy bands at the junction, depicted in Figure 2.8. Due to the electron and hole density gradients between p-type and n-type silicon, the former diffuse into the p-region, while the latter diffuse into the n-region. Electrons and holes recombine around the junction, forming a so-called *depletion region* that is free of mobile charge carriers. As there are no free charge carriers near the boundary, the remaining ions in the lattice create a space charge region and, therefore, an electric field due to opposing charges in the n- and p-type silicon. This leads to a built-in potential difference $\phi = V_{\text{bi}}$ across the junction of approximately 0.6 V in silicon [4]. The diffusion process and the drift in the electric field compensate each other in thermal equilibrium, and no net current is observed across the junction, which leads to the neutrality condition [4]:

$$N_A x_p = N_D x_n \, . \tag{2.25}$$

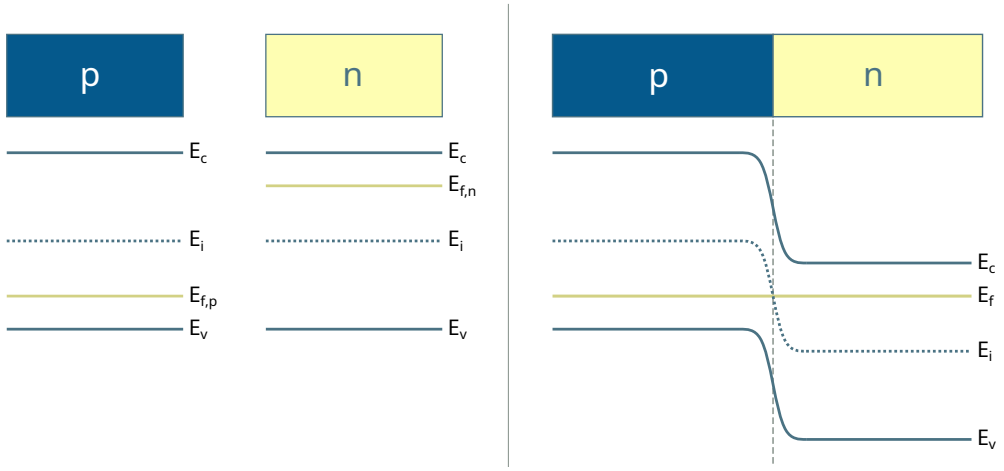

Figure 2.8: Energy levels in p and n doped semiconductor with identical doping concentration. At contact, the energy bands bend in order to adjust for a continuously flat Fermi energy. Adapted from [15].

N_A and N_D are the acceptor and donor concentrations, respectively, and x_p and x_n are the width of the p and n part. The charge density $\rho(x)$ for the four regions is given by [15]:

$$\rho(x) = \begin{cases} 0 & -\infty < x < -x_p\,, \\ -eN_A & -x_p < x < 0\,, \\ eN_D & 0 < x < x_n\,, \\ 0 & x_n < x < \infty\,. \end{cases} \tag{2.26}$$

The junction position is centered at $x = 0$ with the p-type region in the negative x-direction. The same convention is used in Figure 2.9. From (2.26), the electric field in the respective region can be calculated according to Maxwell's equation using the permittivity ϵ:

$$E(x) = \begin{cases} -e\frac{N_A}{\epsilon\epsilon_0}\,(x + x_p) & -x_p < x < 0\,, \\ e\frac{N_D}{\epsilon\epsilon_0}\,(x - x_n) & 0 < x < x_n\,. \end{cases} \tag{2.27}$$

For the other cases in (2.26), the electric field is by definition 0. Integrating the electric field over the whole junction yields the built-in voltage V_{bi} [17]:

$$V_{\mathrm{bi}} = \frac{e}{2\epsilon\epsilon_0}\left(N_D x_n^2 + N_A x_p^2\right)\,. \tag{2.28}$$

The size of the depleted region on the p- and n-side of the junction, respectively, follows from (2.28):

$$x_p = \sqrt{\frac{2\epsilon}{e}\frac{N_D\,V_{\mathrm{bi}}}{N_A\,(N_D + N_A)}}\,, \quad x_n = \sqrt{\frac{2\epsilon}{e}\frac{N_A\,V_{\mathrm{bi}}}{N_D\,(N_D + N_A)}}\,. \tag{2.29}$$

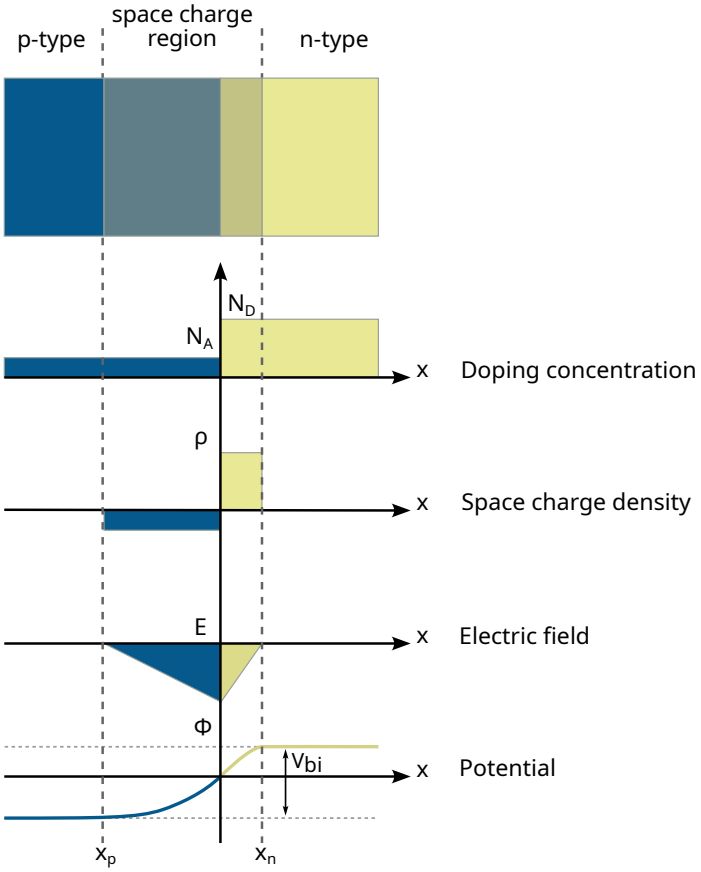

Figure 2.9: Space charge density, electric field, and potential for a pn junction with different doping concentration in the p- and n-type. V_{bi} is the built-in voltage. Adapted from [4].

For charge detection with semiconductor devices, the doping concentrations between p- and n-doping differ significantly, usually by several orders of magnitude. In a typical scenario with an n-doped charge collection electrode, the donor concentration N_D is usually at least six orders of magnitude higher than the acceptor concentration N_A in the p-doped bulk. In that case, the depletion depth d follows from (2.29):

$$d = x_p + x_n \approx x_p \,, \tag{2.30}$$

and, using the effective doping concentration $N_{\mathrm{eff}} = N_D - N_A$, it can be expressed as:

$$d \approx \sqrt{\frac{2\epsilon\epsilon_0}{e\,|N_{\mathrm{eff}}|}\,V_{\mathrm{bi}}}\,. \tag{2.31}$$

An external voltage V_{ext} can be applied to the pn junction which results in $V_{\mathrm{bi}} \to V_{\mathrm{bi}} + V_{\mathrm{ext}}$ and an increase of the depletion depth.

Despite the rectifying behavior, charge carriers generated in the depletion region, for example, from thermal excitation, create a small current over the junction referred to as *leakage current*.

2.2.3 Charge carrier transport in semiconductor materials

Charge transport in the (depleted) silicon material is governed by two main mechanisms: diffusion and drift.

Drift In the presence of an electric field, the charge carries are accelerated in or against the direction of the electric field, depending on their charge. The charge carriers undergo scattering off lattice atoms and impurities among other effects. Focusing on a p-type semiconductor, the net current can be described by [16]:

$$I = qpv_D A \tag{2.32}$$

with q the charge, p the hole density, A the plane through which the current flows and v_D the drift velocity of the charge carriers. The latter is proportional to the applied electric field E with the proportionality constant μ that is referred to as mobility and is characteristic for the charge carrier and type of semiconductor:

$$v_D = \mu(E)\, E\,. \tag{2.33}$$

Notably, mobility itself depends on the electric field. From experimental observations, an empirical relation between mobility and electric field was developed in [19] that describes the increase of the mobility with the electric field and is different for electrons and holes. For a wide range of electric field strengths, the mobility is roughly constant with [4]:

$$\mu(E) = \frac{\mu_0}{\left[1 + \left(\frac{\mu_0 E}{v_{\mathrm{sat}}}\right)^{\beta}\right]^{1/\beta}}\,. \tag{2.34}$$

Here, μ_0 is the so-called *low-field mobility* and v_{sat} is the saturation drift velocity reached in very high fields. In silicon, the parameter β is roughly 1 for holes and 2 for electrons [19]. A detailed discussion of the slight dependence on doping and temperature can be found in [16]. The electron and hole mobilities in silicon at room temperature are approximately [4, 16, 19]:

$$\mu_e \approx 1400\,\tfrac{\mathrm{cm}^2}{\mathrm{V\,s}} \quad \text{and} \quad \mu_h \approx 500\,\tfrac{\mathrm{cm}^2}{\mathrm{V\,s}}\,. \tag{2.35}$$

Diffusion Diffusion processes arise from a concentration gradient and thermal motion and are not limited to charge carriers. In silicon, the diffusing entities are charged, which gives rise to a current. Following Fick's law [20], the current in a simple, one-dimensional case can be expressed as:

$$I = -qAD_p \frac{\mathrm{d}p}{\mathrm{d}z}\,. \tag{2.36}$$

The quantities q, p, and A are the same as in (2.32); D_p is the diffusion constant for holes and the (one-dimensional) derivative is the hole density gradient. In the case of electrons, the sign of the derivative changes due to the concentration gradient in the opposite direction. Together with the opposing charge, the current flows in the same direction for both electrons and holes. The diffusion constant is related to mobility according to the Einstein relation [21]:

$$D = \mu \, k_B T \, . \tag{2.37}$$

Charge clouds Multiple charges created as one charge *cloud* are subject to a diffusion process which broadens its size over time. Following from Fick's law and the continuity condition, i.e., no charge carriers are lost nor new ones created, one arrives at a differential equation that can be solved by a Gaussian function. A derivation can be found in [4]. The width of the charge cloud is then:

$$\sigma = \sqrt{2Dt} \, . \tag{2.38}$$

If the width σ is in the order of or larger than the pixel size, the charge signal is not only recorded by a single readout electrode but by multiple, creating so-called (charge) clusters. A detailed explanation and possible consequences are given in Chapter 3.2.

2.2.4 Creation of charge signal at the readout electrode

Charges created in the (depleted) pn junction are subject to drift and diffusion, as described before. In reverse-bias operation, electrons drift towards n-doped regions, while holes drift towards p-doped regions in the silicon. The movement of charges induces a signal on the readout electrodes, which can be processed in a next stage. The principle described by Shockley [22] and Ramo [23] considers a system of electrodes, as in a segmented semiconductor detector, and is referred to as the *Shockley-Ramo theorem*.

It states that the induced current i on an electrode in the one-dimensional case is [23]:

$$i = q E_w v_D \tag{2.39}$$

with q the moving charge, v_D its velocity, and E_w the weighting field. The latter is the electric field in direction of v_D if the charge q were not present and unit potential is applied to the electrode under consideration while all others are grounded. Equation (2.39) can be generalized for the three-dimensional case as:

$$i_i = q \vec{E}_{\mathrm{w},i} \vec{v}_D \, . \tag{2.40}$$

The index i denotes electrode i in a system with multiple electrodes and $\vec{v}_D$ is the drift velocity defined in (2.33). Diffusion is neglected in the processes described in this section. Related to

the weighting field is the weighting potential $\phi_{\mathrm{w},i}$ with:

$$\vec{E}_{\mathrm{w},i} = -\vec{\nabla}\phi_{\mathrm{w},i} \,. \tag{2.41}$$

It obeys the Laplace equation and can be calculated by setting the potential at electrode i to 1 and that of all other electrodes to 0. The weighting potential and corresponding field lines for a simple structure with one-dimensionally segmented electrodes are shown in Figure 2.10. The electrodes are shown in red, with only the central one under consideration, which is set to unit potential such that all field lines are aligned towards that electrode. From (2.40), the total

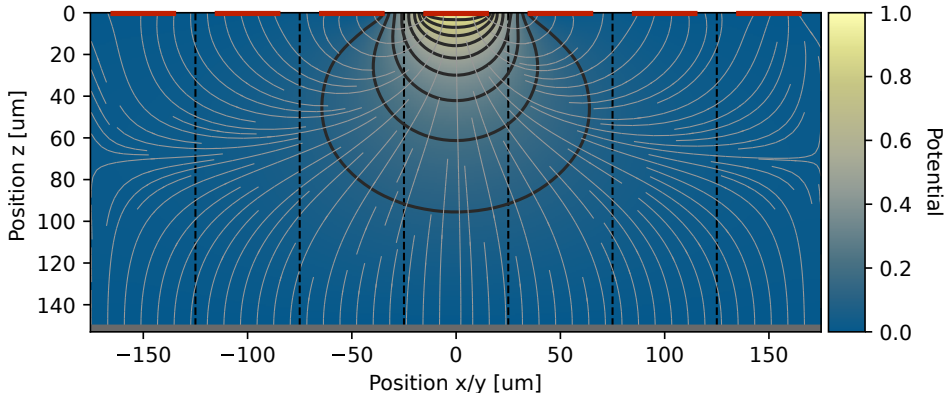

Figure 2.10: Weighting potential and field of a single electrode in a segmented structure. Unit potential is only applied to the central electrode while all others are set to ground potential. The field lines are visualized in gray, the potential is shown in color. Simulated using [24].

charge induced on electrode i from a charge carrier moving from $\vec{x}_0$ to $\vec{x}_1$ can be calculated by integration [25]:

$$Q_i = \int_{\vec{x}_0}^{\vec{x}_1} q\vec{E}_{\mathrm{w},i}\,\mathrm{d}\vec{x} = -q\left[\phi_{\mathrm{w},i}(\vec{x}_1) - \phi_{\mathrm{w},i}(\vec{x}_0)\right] \,. \tag{2.42}$$

If the sensor volume is depleted, as is usually the case in a semiconductor pixel detector, an additional space charge is present in the charge-sensitive volume. As long as this space charge is constant, it does not contribute to the charge induced on the electrodes.

2.3 Radiation damage

Apart from charge creation, incident particles can alter the performance and characteristics of a semiconductor pixel detector. Since these changes are typically irreversible, they will be referred to as *radiation damage*. High-energy physics experiments typically exhibit significant levels of radiation that all the detector components have to withstand. Radiation damage can be separated into two mechanisms [26]:

Ionization processes This type of damage arises from interaction with atomic electrons mostly in the silicon oxide (SiO_2) on the surface, boundaries, and interfaces (Si-SiO_2). Consequently, this type of radiation damage is also referred to as surface damage and mostly affects the electronics located on the surface of the detector.

Bulk damage Interactions of the incident particle with the lattice nuclei in the silicon cause bulk or displacement damage. As these processes are not related to ionization, they are also called *non-ionizing* radiation damage. This type of damage changes the characteristics of the silicon bulk in which detectable electron-hole pairs are created.

2.3.1 Ionization energy loss

As described in Section 2.1, particles lose energy when traversing a material mostly by ionization and excitation of atoms, depending on their energy (for electrons and positrons, energies below the critical energy). This creates electron-hole pairs in the oxide layers of the silicon part where the readout electronics is implemented. In these circuits, due to the applied transistor bias voltage, the electrons and holes are separated in the electric field, and the holes accumulate near the Si-SiO_2 interface [8]. Effectively, this creates a charged layer that introduces an electric field, which changes the characteristics of the transistors by shifting the threshold voltage. Apart from the *total ionizing dose* (TID), i.e., energy deposited in the silicon, this effect is dose-rate dependent. This dependency originates from the possible recombination of electrons and holes; a more detailed discussion can be found in [8].

2.3.2 Non-ionizing energy loss

If particles collide with lattice atoms during their passage through matter, they can dislocate the atoms. This leads to point-like defects if they dislocate one atom or cluster effects if the dislocated atom has sufficient energy to dislocate more atoms in its vicinity. In general, protons produce more point and neutrons produce more cluster defects [27], although the effect of bulk damage also depends on the energy of the impinging particles. To quantitatively compare the produced radiation damage, a scaling called *non-ionizing energy loss* (NIEL) is introduced, such that the radiation damage scales linearly with NIEL. It takes into account the deposited energy that is not related to ionization and compares it to a reference particle and energy, by convention a neutron of 1 MeV. This allows for comparison of radiation damage from different types of damaging particles with different energies.

2.3.3 Bulk damage effects in silicon semiconductors

In the following, a selection of resulting effects and changes to the semiconductor properties is discussed. More details can be found in [8, 28].

The threshold energy E_d for displacement of single atoms ranges from 13 – 33 eV [28] in silicon. Such displacements create so-called *vacancies*, *interstitials*, and *Frenkel pairs* that are a combination of the two. They are depicted in Figure 2.11. Due to a low activation energy for

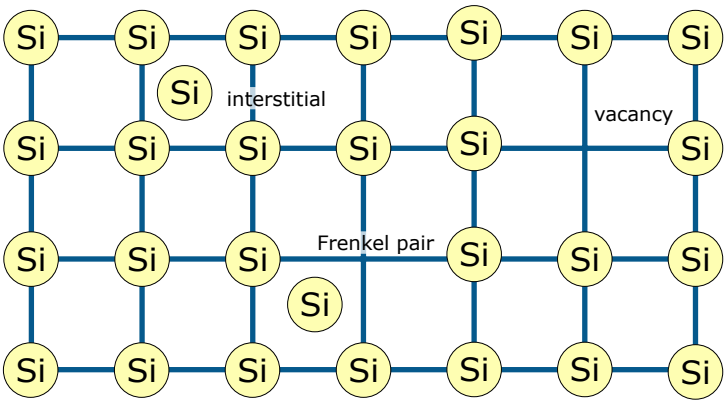

Figure 2.11: Displacement damage in a silicon lattice with interstitial lattice atoms, vacancies and Frenkel pairs.

migration throughout the crystal in the order of 18 – 45 meV [29], a fraction of defects will anneal and fill vacancies with interstitials, for example, creating stable defects. Annealing changes the electrical properties of silicon by introducing recombination-generation and trapping centers [8] as well as additional donor and acceptor levels. Recombination-generation centers are typically located in the middle of the band gap. They either generate additional (thermal) electron-hole pairs due to the smaller distance to the valence and conduction band, contributing to the leakage current or allow for recombination of electrons and holes from the conduction and valence band in this defect. Defects at energies close to the conduction and valence band edges can alter the effective doping, while trapping centers catch and release mobile charge carriers. If the time constants related to these processes are longer than the typical charge collection time, trapped charges will not fully contribute to the signal. The mentioned damage effects are discussed in detail and mathematically treated in the *Shockley-Read-Hall* framework, given in [30, 31]. A schematic drawing of defects in the energy band diagram is shown in Figure 2.12.

The resulting effective doping concentration as a function of the particle flux Φ can be described by [27]:

$$N_{\text{eff}}(\Phi) = N_D e^{-c\Phi} - N_A e^{-d\Phi} + (\beta_D - \beta_A)\,\Phi\,, \tag{2.43}$$

where N_D and N_A are the initial donor and acceptor concentrations, c and d can be interpreted as removal cross sections, and β_D and β_A are parameters reflecting the creation of defects that behave like donors or acceptors. It should be noted that the latter term in (2.43) is generally negative, which leads to so-called *type inversion* in n-type silicon (behaving like p-type silicon) with increasing particle flux [32]. Because of trapping in the silicon, decrease of the effective doping concentration, and consequently the smaller depletion depth at the same

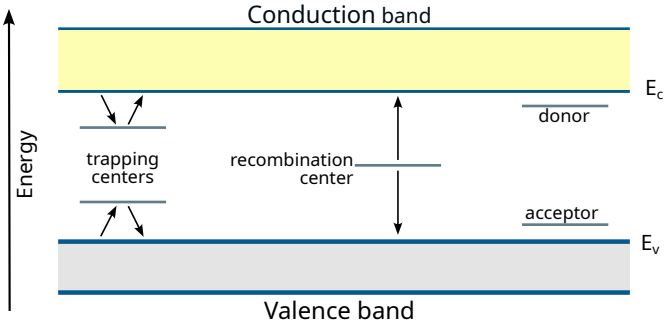

Figure 2.12: Energy levels in the band diagram for different substrate defects: trapping centers, recombination-generation centers, and additional acceptor and donor levels.

voltage, operation of irradiated silicon pixel detectors requires high voltages and large signals to overcome the reduction of collected charges. Additionally, the increase in leakage current usually demands cooling during measurements.

3 Depleted monolithic active pixel sensors

This chapter starts with an overview of existing semiconductor detector technologies. While all of them can be used for particle detection, their advantages and disadvantages for high-energy physics experiments are discussed. A focus lies on monolithic pixel detectors, more specifically those with depleted substrates (DMAPS) such as the TJ-Monopix detector design that is investigated in the scope of this work.

3.1 Silicon detector technologies

The first developments of integrated circuits in the late 1950s [33] led to a continuous and ever-growing research in the field of semiconductor fabrication and devices. Modern circuits are almost exclusively built from CMOS (complementary metal–oxide–semiconductor) elements that offer a high packaging density and low power consumption [34] by using both n-channel and p-channel MOSFETs (metal–oxide–semiconductor field-effect-transistors). With the availability of manufacturing fine-segmented structures and circuits in the order of micrometers, solid-state detectors became an important and revolutionary part of particle physics. The spatial resolution of segmented semiconductor detectors represented a huge improvement compared with the previously used gaseous detectors by two orders of magnitudes [4]. At the same time, the deposited energy and the generated signal are larger in semiconductor detectors due to the higher density compared with gases. The main semiconductor detector concepts that are actively used in high-energy particle physics today are presented in the following.

3.1.1 Microstrip detectors

Microstrip detectors are silicon devices that have segmented electrodes in one dimension. Thus, they provide only one-dimensional spatial resolution, but are easy to read out because the electronics can be connected at the end of each strip. A schematic drawing of this detector type is shown in Figure 3.1. Early developments already achieved spatial resolutions of 5 µm in a setup of six microstrip detectors with a strip pitch of 20 µm [35].

Two strip detectors can be mounted at an angle with respect to each other to extend the positional resolution to a second dimension. Typical angles are in the order of 10 mrad [36]. To reduce the resulting increase in material budget and required electronics, two layers of strips can be implemented on the same silicon bulk. The second layer of strips is placed on the opposite side

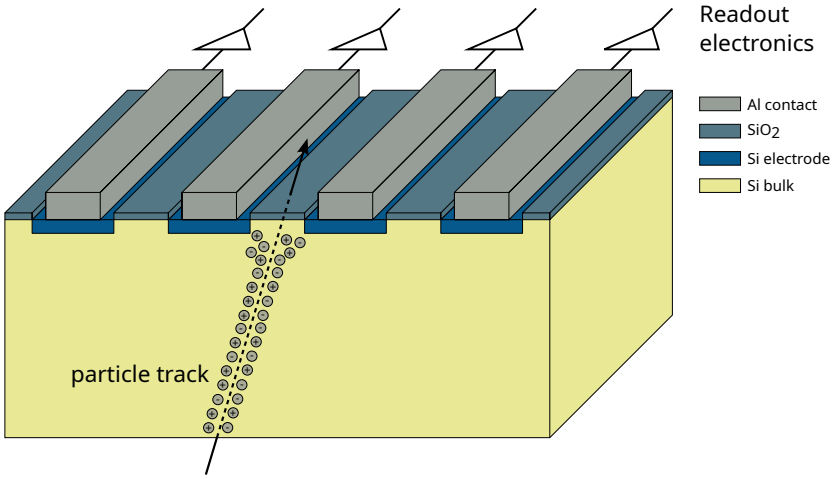

Figure 3.1: Schematic drawing of a microstrip detector. Electrodes are implemented on one side of the silicon bulk, and the readout electronics is located at the end of each strip.

of the silicon bulk and oriented perpendicular to the other layer. In this approach, more complex implantations with different doping levels are required, which significantly increases production costs compared to single-sided strip detectors [4]. Both the ATLAS and CMS detectors at the Large Hadron Collider use single-sided microstrip detectors due to simplicity in handling and operation, as well as cost [37, 38].

3.1.2 Hybrid pixel detectors

Further developments [39] led to segmented silicon detectors with two-dimensional spatial information, so-called *pixel detectors*. Nowadays, the pixels have typical sizes of a few 10 µm to a few 100 µm, depending on the application. In high-energy particle physics experiments, the readout electronics can usually not be placed at the end of the detector as is done for strip detectors. Each readout channel has to be connected to each electrode, which is achieved by so-called *bump bonding* of two separate chips. As a result, a pixel cell is a stack of two silicon blocks that are interconnected. The charge sensing part (referred to as *sensor*) and the readout electronics (referred to as *front-end*) are connected by conductive bump balls and are required to have a matching layout. These detectors are called *hybrid* pixel detectors as opposed to *monolithic* ones, which are fabricated in one silicon wafer and described in the next section. While the sensor is produced from highly doped silicon wafers to provide large amounts of created charges, the readout chip containing electronic circuitry is typically implemented in conventional CMOS technology on lightly doped silicon substrate. The structure of this detector type is depicted in Figure 3.2. Hybrid pixel detectors are state-of-the art devices for environments with high hit occupancy and high radiation, such as the ATLAS and CMS experiments at the LHC. Since the sensor and readout chip are designed and fabricated separately, they can be optimized indi-

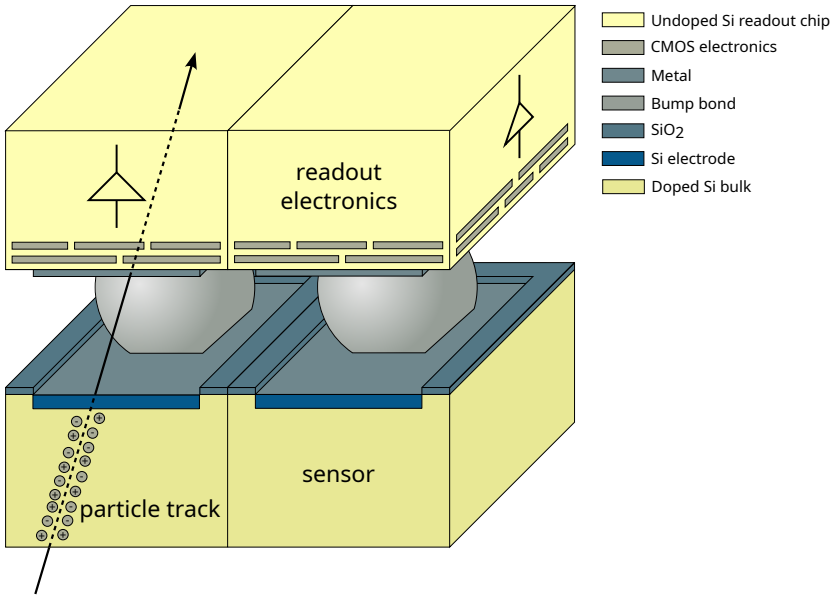

Figure 3.2: Schematic drawing of two hybrid pixels for charge detection. Sensor and readout chip are connected with a conducting bump bond. For solderability, metal is added above and below the bump bond. The sensor is fabricated on highly resistive silicon while the readout chip is built in commercial CMOS technology.

vidually for their specific requirements. Current readout chips for the innermost detector layers at ATLAS can withstand ionization doses of up to 1 Grad [40]. Optimized sensors for those readout chips with $50\,\mu m \times 50\,\mu m$ pixel size still operate within the required specifications after NIEL doses of more than $1 \times 10^{16}\,n_{eq}\,cm^{-2}$ [41]. Due to the separate fabrication of sensor and readout chip for hybrid pixel detectors, the bump bonding adds a complex and cost-intensive assembly step. Additionally, the two entities (sensor and readout chip) for a single detector layer represent a significant material budget.

3.1.3 Monolithic pixel detectors

In an attempt to simplify the hybrid detector design in terms of assembly and material budget, devices with readout circuitry implemented on the same silicon wafer as the sensor part were proposed as early as in the 1980s [42]. A schematic drawing of this idea is shown in Figure 3.3. Early prototypes were either designed in custom processes on silicon with high-resistivity, for example in [43], or in standard processes on low-resistivity epitaxial silicon [44]. While the former approach offers large signals due to the high resistivity of the silicon, it requires non-standard processing, which is cost-intensive and complex. The latter design utilizes commercial CMOS technologies available on thin ($\sim 15\,\mu m$) lightly doped silicon, at the cost of a small and slow signal due to non-depleted bulk material. Those devices are referred to as *monolithic active pixel detector* (MAPS). Commercial technologies typically use low-ohmic substrate wafers with

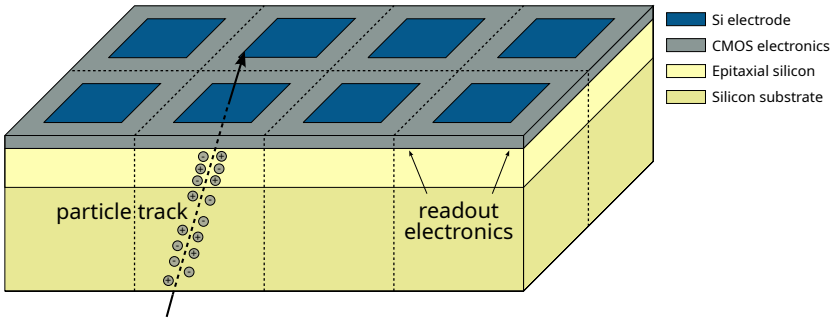

Figure 3.3: Schematic view of a monolithic pixel detector composed of eight pixels. The readout electronics is integrated in each pixel. Typically, the sensing part is epitaxial silicon grown on low-ohmic silicon substrate.

epitaxial silicon on top in which particles can be detected. Electronics is implemented at the top side of the epitaxial silicon. This type of silicon is produced by epitaxial growth processes resulting in good electrical properties and a long mean free path length which is beneficial for charge collection (see Section 2.2.3). The thickness of the charge-sensitive layer is in the order of $1-20\,\mu m$, which limits the amount of created charge carriers. Only a small part of the detector volume is depleted, and most charges are collected by diffusion. Figure 3.4 shows the cross-section of a monolithic pixel detector. Charge is collected by an n-type electrode

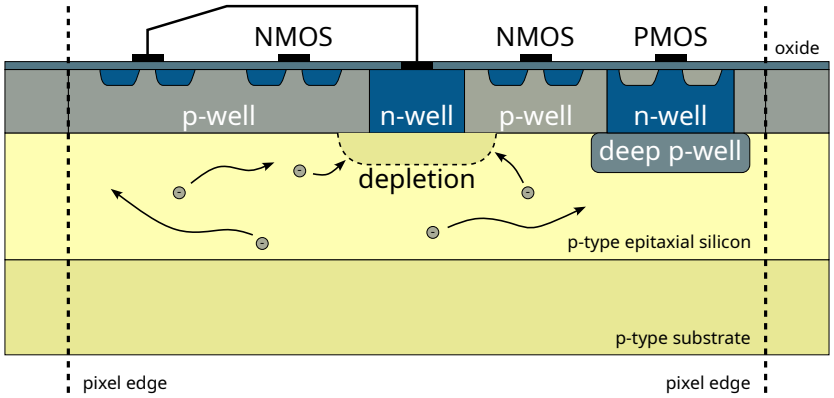

Figure 3.4: Cross-section of a monolithic active pixel detector. Only a small region is depleted and most charges are collected by diffusion. A deep p-well implantation shields n-wells for PMOS transistors so that they do not act as a charge collection electrode. Adapted from [4].

around which a small depletion region forms. To implement full CMOS logic, n-wells for PMOS transistors are required which would otherwise compete with the charge collection electrode. In order to shield them, additional p-type implants can be added below (*deep implant*). Due to a large contribution to the signal from diffusion, the charge collection process is slow (in the order of $10-100\,\mu s$) and charges might be lost due to undirected motion and trapping. This makes monolithic pixel detectors unsuitable for high-rate environments such as trackers

for ATLAS or CMS. Nevertheless, due to the small material budget, they are good candidates for less time-critical applications and actively used in high-energy physics experiments [45, 46].

Depletion is crucial for fast charge collection and a large signal. The availability of commercial CMOS technology that can withstand voltages on the order of multiple 10 V fueled new developments of monolithic pixel detectors [47]. With these high-voltage capabilities (compared to typical CMOS voltage levels well below 10 V), significant depletion of the bulk material can be achieved. Section 3.2 will go into more detail about the developments in this field.

3.2 Depleted monolithic active pixel sensors

From Section 2.2, it can be concluded that depleted silicon is crucial for fast charge detection in high-radiation environments. The drift velocity and therefore induced current scales with the electric field, and especially after irradiation, high fields are necessary to counteract degradation. Since the deposited energy and therefore the number of created charge carriers scale with the traversed path length of the incident particle, the depletion region should be as large as possible. However, keeping the material budget in mind, a compromise must be found. The resistivity ϱ of the silicon is related to the doping concentration, such that (2.31) for an external voltage $V_{\text{ext}} \gg V_{\text{bi}}$ can be written as:

$$d \propto \sqrt{\varrho\, V_{\text{ext}}}\,. \tag{3.1}$$

From this equation, it can be seen that large depletion in silicon is achievable by using highly resistive silicon and/or applying high voltage. Typical values are in the order of $1-10\,\text{k}\Omega\,\text{cm}$ and $10-500\,\text{V}$, respectively, depending on the provided silicon and the sensor design. However, high voltage applied to the sensor leads to a steep gradient of the electric potential at the edge of the pixel matrix. The correspondingly high electric field enables avalanche multiplication of charge carriers, leading to a breakdown behavior of the reverse-biased pn junction. Adding so-called *guard rings* around the pixel matrix smooths the gradient of the electric potential and improves the breakdown behavior. With careful design of the guard rings, voltages of several hundred volts can be applied to the sensor [48]. While the discussion above is valid for all semiconductor particle detectors, a focus is put on monolithic ones in the subsequent paragraphs.

Availability of high-resistivity substrates with high-voltage capabilities in commercial CMOS technologies offers comparably inexpensive (with respect to hybrid pixel detectors) and large-volume production of *depleted monolithic active pixel sensors* (DMAPS). They benefit from depleted substrates and active readout electronics integrated in each pixel. This reduces the material budget of pixel detector systems while potentially offering operational performance suitable for high-energy physics experiments with high particle rates and harsh radiation environments. Many prototypes have been designed [49–52], of which one is presented and charac-

terized in this thesis. Two general approaches in terms of collection-electrode design have been pursued from these prototypes:

Large collection electrode The charge collection electrode covers a large area of the pixel. The electronics is completely implemented inside the electrode with multiple nested wells.

Small collection electrode The charge collection electrode is separated from the readout electronics which is implemented in a dedicated area of the pixel. This area is significantly larger than the size of the collection electrode.

Both designs are shown in Figure 3.5 side-by-side to point out the design differences without going into the details of the actual implementations. It can already be seen from a geometrical

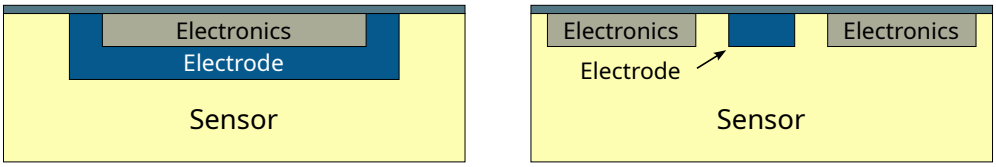

Figure 3.5: Simplified structure of large- (left) and small- (right) collection-electrode designs. The electronics is either integrated in (left) or separated from (right) the collection electrode. While the former is intrinsically more radiation-hard, the latter offers a very small detector capacitance which is related to better noise and timing performance.

standpoint, that a high and homogeneous electric field is easier to achieve in the large-collection-electrode design, but at the cost of the detector capacitance C_D that scales with the area of the electrode. With

$$\mathrm{d}V = \frac{\mathrm{d}Q}{C_D}\,, \tag{3.2}$$

it follows that the large capacitance leads to a small voltage signal at the amplifier input compared to the small-collection-electrode case with significantly smaller capacitance. Additionally, the electric noise of the amplifier scales quadratically with the detector capacitance [53]. The field geometry in a large-collection-electrode DMAPS is by design homogeneous with parallel field lines, which is an advantage for achieving radiation hardness. For high-rate and high-radiation environments the small-collection-electrode approach has to be precisely tuned in order to achieve full depletion, even after irradiation.

3.2.1 Large-collection-electrode DMAPS

The large-collection-electrode design was already implemented in one of the first DMAPS prototypes [47]. The CMOS electronics is placed in the charge collection electrode. Due to the implant structure in the silicon, it is often called *very-deep* or *deep n-well*, since the electrode is the deepest implant. In the following, an n-type collection electrode on a p-type substrate

(n-in-p) is considered, although other possibilities (such as n^+-in-n) exist. Figure 3.6 shows the schematic cross-section of this design. It can be seen that this structure requires manu-

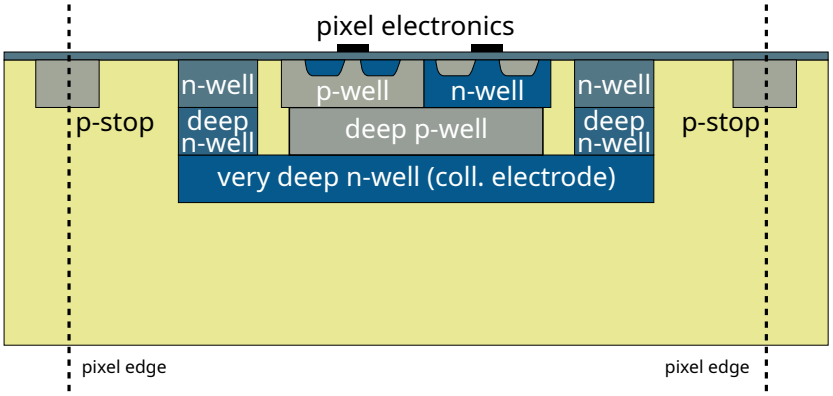

Figure 3.6: Cross-section of a depleted MAPS with a large collection electrode. Front-end electronics is located inside the n-well structure and shielded from the collection node by a deep p-well. *Deep* and *very deep* are classified related to the depth of the implant. The p-stop structure increases the electric field in the inter-pixel region where charge carriers can accumulate. Bias voltage is applied to the backside.

facturing processes that offer deep implantation across multiple layers. PMOS transistors are implemented in n-wells that are isolated from the collection electrode by a large p-well in which NMOS transistors are implemented to allow for full CMOS circuitry. Depletion is achieved by applying a negative bias voltage either through a backside contact or from the top, while keeping the collection electrode at ground or at least more positive than the bias voltage. The drift in a fully depleted substrate makes the design suitable for high-radiation environments, as the drift paths to the collection electrode are short and the probability of trapping small. Dedicated efforts for the guard ring structure on the sensor edges lead to breakdown voltages over 300 V [54] and maximize the depletion and electric field after irradiation.

The capacitance $C_{pw\text{-}n}$, between deep p-well and collection electrode introduces capacitive coupling between the two and significantly contributes to the overall detector capacitance. Although the design is similar to that of a planar sensor used for hybrid pixel detectors, the additional capacitance mentioned above results in a higher total capacitance. For a pixel of 50 µm × 250 µm, the detector capacitance of a large collection DMAPS is approximately 400 fF [55], a factor four higher than the 110 fF capacitance of a planar sensor of the same size [56]. Large electrode designs are proven to show a good performance after neutron irradiation to $10^{15}\,\mathrm{n_{eq}\,cm^{-2}}$, with 98.9 % hit detection efficiency [57].

3.2.2 Small-collection-electrode DMAPS

The small-collection-electrode design is similar to the one from MAPS detectors as depicted in Figure 3.4. In order to minimize coupling between the collection n-well and the readout

electronics, the former is separated by a few micrometers from the p-well in which the transistor logic is implemented. The size of the collection well is typically in the order of 2 µm, leading to a small capacitance C_D of about 5 fF [58]. According to

$$\mathrm{d}V = \frac{\mathrm{d}Q}{C_D}\,, \tag{3.3}$$

the voltage signal is larger than in a large-collection-electrode design, which allows for simpler amplifiers and circuitry. In Figure 3.7, a cross-section of this structure is shown. In modern

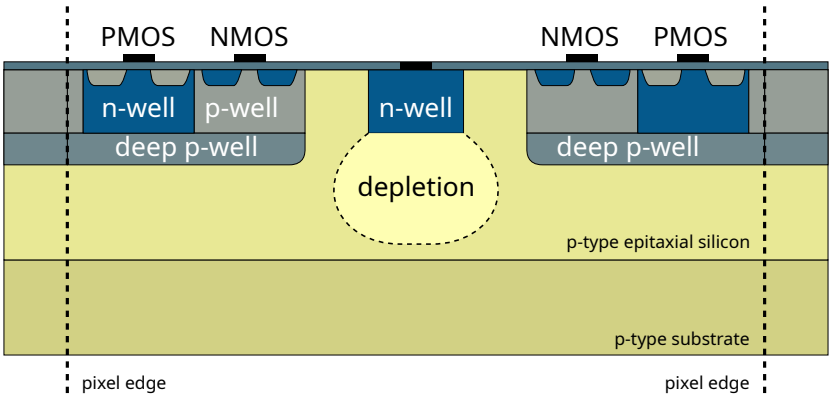

Figure 3.7: Cross-section of a depleted MAPS (DMAPS) with small collection electrode. The front-end electronics is separated from the n-type readout electrode. Full CMOS circuitry is possible due to the deep p-well implant that isolates the n-well substrate of the implemented transistors from the charge sensitive volume. Depletion is achieved by applying a voltage on the backside and the depletion region grows from the collection electrode, although the volume below the electronics typically cannot be fully depleted.

devices, the pixel pitch of $p < 50$ µm is typically smaller than in the large-collection-electrode design. This leads to an increased formation of charge clusters where the charge cloud is read out by multiple neighboring pixels. By identifying those clusters, the position resolution of the incident particle can be improved, even further by using energy information of the hits as weights for calculating the mean position. Full CMOS circuitry can be implemented because of the deep p-well that isolates the n-well of PMOS transistors, which would compete as charge collection electrode. Due to the geometrically small pn junction between collection electrode and epitaxial layer, the depletion region grows around this interface equally to the backside and sideways. Typically, a negative bias voltage is applied to the deep p-well and the backside of the chip. In the former case, the applicable voltage is limited by the rating of the transistors implemented in the p-wells. Due to the sensor's geometry, the voltage difference between substrate and deep p-well typically cannot exceed 1 V. For a higher voltage difference, punch-through between the two can be observed. The connection between p-well and n-well for the readout electronics forms another pn junction that is susceptible to diode breakdown. Due to the mentioned limitations, the typically applicable voltage is limited to a few volts in this design, which potentially depletes

only a part of the sensor volume.

Complete and fast charge collection is only possible in depleted silicon, which makes the design unsuitable for experiments with high particle flux and high radiation exposure because of charge collection by diffusion and long drift paths. For homogeneous and full depletion of the sensor volume, additional doping profiles are necessary, which will be explained in detail in Chapter 4.

4 Design of TJ-Monopix2

This chapter introduces the design of the TJ-Monopix prototypes from a sensor and front-end perspective. The first prototype, TJ-Monopix1, was designed in 2017 as a candidate for the ATLAS Inner Tracking Detector (ITk), which will replace the current Inner Detector in view of the high-luminosity upgrade of the Large Hadron Collider. While TJ-Monopix1, as well as other monolithic pixel detector proposals, was not pursued for this use case, further research and development in this technology has been conducted.

An enhanced sensor geometry with the original front-end design was submitted in 2019, and its radiation hardness has been studied within this thesis. TJ-Monopix2 is a successor to TJ-Monopix1 and was designed in 2020. The matrix size has been doubled, while the pixel size has been reduced. With the same sensor geometry as in TJ-Monopix1, the focus was put on the front-end electronics to allow for operation at a significantly lower threshold. Both TJ-Monopix prototypes were developed in other works [59] and are introduced in this chapter. The design of the advanced digital periphery of TJ-Monopix2 is part of this thesis and is described in Section 4.3. Lastly, the custom-developed data acquisition system required for testing TJ-Monopix2 is presented.

4.1 Sensor geometry

The sensor geometry is a result of a long R&D process of monolithic active pixel sensors for high-energy physics experiments. It uses the Tower Semiconductor 180 nm CMOS imaging process[1], which offers high-resistivity ($> 1\,\mathrm{k\Omega\,cm}$) epitaxial silicon with thickness up to 30 µm. For the upgrade of the ALICE Inner Tracking System [60], a prototype chip Explorer-0 [61] was designed to study the sensor design of a MAPS in this CMOS process with the goal of a thin (50 µm) tracking detector with pixel pitch of $\mathcal{O}(30\,\mu\mathrm{m})$ and low power consumption. Further submissions towards the full-scale chip ALPIDE showed good performance results [62, 63] meeting the requirements. The schematic cross-section of the ALPIDE chip corresponds to the one shown in Figure 3.7. This design relies on charge collection partially by drift in the small depleted volume and mostly by diffusion. Apart from the achievable charge collection time in the order of µs, the detector is susceptible to radiation damage. The introduced traps slow down the charge collection and decrease the amount of collected charge. For high-radiation environments,

[1] `https://towersemi.com/` (visited on 13 July 2024)

modifications are necessary to achieve full depletion to shorten the charge collection time (by drift) and the radiation tolerance to levels of $\geq 10^{15}\,\mathrm{n_{eq}\,cm^{-2}}$.

4.1.1 Process modification with continuous n-layer

Together with the foundry, a modification to the existing process was developed that adds a low-dosed n-type implant to the p-type epitaxial layer [64]. The oppositely doped implant creates a planar pn junction across the whole pixel area allowing for homogeneous depletion of the epitaxial layer and at the same time, a pn junction between the deep p-well and the implant. A schematic cross-section of this modification is depicted in Figure 4.1. With increasing negative

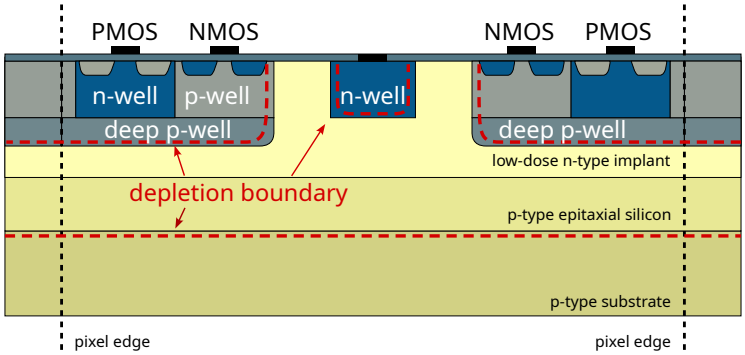

Figure 4.1: Process modification with a low-dosed n-type implant across the pixel area. The doping is tuned to achieve depletion boundaries as indicated for homogeneous depletion of the epitaxial silicon.

bias applied to the substrate and the deep p-well, the depletion region grows both towards the collection electrode and the boundary between the epitaxial layer and the substrate, as indicated in the figure. The doping of the n-type layer has to be tuned precisely to be low enough for full depletion, but high enough to prevent punch-through between the p-type substrate and the deep p-well. Detailed simulations and measurements on investigator chips are performed in [64, 65], comparing the performance of the original and the modified sensor geometry.

4.1.2 Towards an improved sensor geometry

Measurements on more prototype chips with integrated digital readout electronics produced in this modified process showed a significantly lower hit detection efficiency after irradiation of about 70 % compared with non-irradiated samples of about 97 %, predominantly in the pixel corners below the deep p-well [66–68]. Simulations [69, 70] confirmed these findings by showing a very small electric field between the pixels resulting in a long charge collection time. An increased number of impurities makes charge trapping more likely in irradiated silicon, which causes charge loss, especially in combination with long charge collection times (see also Section 2.3.3). A qualitative TCAD[2] simulation in Figure 4.2 shows the concentration of trapped

[2]Technology Computer-Aided Design. It is used for modeling and simulating semiconductor devices.

charge carriers after irradiation to $10^{15}\,\mathrm{n_{eq}\,cm^{-2}}$ after 25 ns. A significant fraction of charge carriers below the p-well, in which the electronics is integrated, will not reach the collection electrode due to trapping. Therefore, it is necessary to improve the electric field shape in this

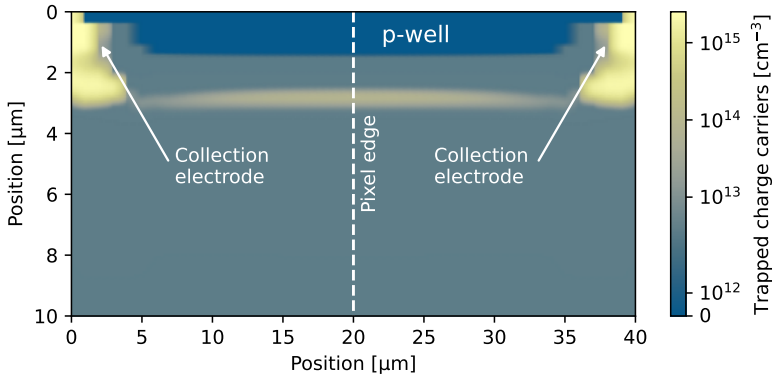

Figure 4.2: TCAD simulation of the topmost region of a single pixel showing trapped charge carriers in the small-collection-electrode design after 25 ns at an irradiation level of $10^{15}\,\mathrm{n_{eq}\,cm^{-2}}$. The geometry and doping are comparable to those of TJ-Monopix1. Yellow areas on the edges are the locations of the charge collection electrodes. Reproduced with data from [70].

region. For comparison, the concentration of trapped charge carriers in the same sensor geometry before irradiation is displayed in Figure A.1 Two approaches to increase the radiation hardness were proposed based on simulations [69]:

N-gap design The low-dosed n-type implant layer is removed at the pixel edges. This leaves a p-type silicon part below the deep p-well which shapes the electric field lines towards the collection electrode.

Additional deep p-well An additional p-type implant is added below the deep p-well. The shaping of the electric field is influenced in the same way as in the n-gap design.

Both designs substantially enhance the performance after radiation fluences of $10^{15}\,\mathrm{n_{eq}\,cm^{-2}}$, with the n-gap variant collecting slightly more charge after irradiation than the additional p-well one, according to simulations [69]. The cross-sections of both approaches are discussed in Section 4.1.3 and depicted in Figure 4.3 and Figure 4.4.

4.1.3 Sensor geometry variants of TJ-Monopix2

The two geometries explained in Section 4.1.2 are implemented in two different silicon substrates, resulting in four combinations that are available for testing. They are implemented in 30 µm thick epitaxial silicon on a low-resistivity substrate offered from the foundry and on highly resistive Czochralski silicon. In both cases the resistivity is $> 2\,\mathrm{k\Omega\,cm}$. For a large charge signal, a large thickness of the high-resistivity silicon is beneficial, which is limited to 30 µm in

the available epitaxial silicon wafers. On the contrary, Czochralski silicon substrates have 100 µm thickness, possibly yielding a higher signal if it can be depleted further than 30 µm. The available samples are depicted in Figure 4.3 for the epitaxial silicon and Figure 4.4 for the Czochralski silicon.

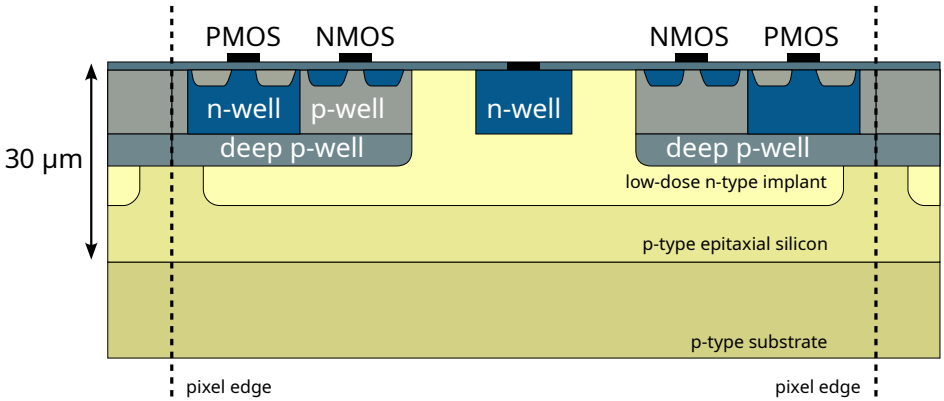

(a) Sensor geometry with a gap in the low-dosed n-layer, implemented in 30 µm thick epitaxial silicon.

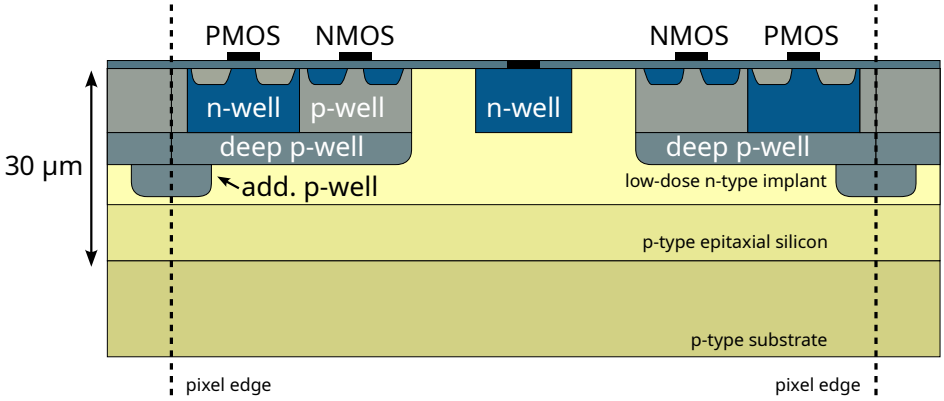

(b) Sensor geometry with an additional p-well implant at the pixel edge, implemented in 30 µm thick epitaxial silicon.

Figure 4.3: Sensor geometries of TJ-Monopix2, produced in high-resistivity epitaxial silicon on a low-resistivity substrate. The thickness of the epitaxial layer is 30 µm. A gap in the n-implant layer (a) or an additional deep p-well (b) shapes the electric field at the pixel edges towards the collection electrode. The drawings are not to scale.

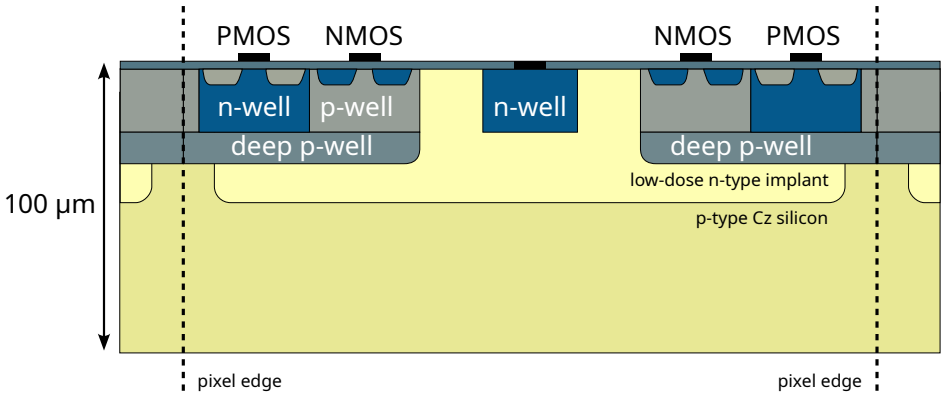

(a) Sensor geometry with gap in the low-dosed n-layer, implemented in 100 µm thick Czochralski silicon.

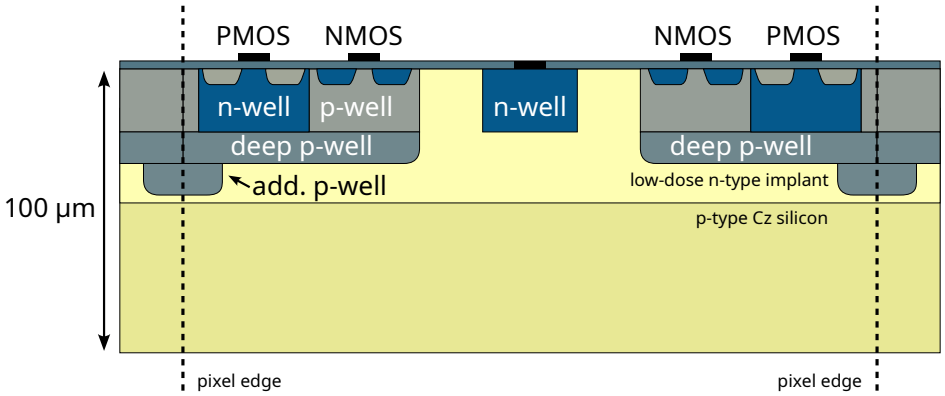

(b) Sensor geometry with additional p-well implant at the pixel edge, implemented in 100 µm thick Czochralski silicon.

Figure 4.4: Sensor geometries of TJ-Monopix2, produced in high-resistivity Czochralski silicon. The thickness of the substrate is 100 µm, potentially yielding a higher charge signal than in 30 µm epitaxial silicon. A gap in the n-implant layer (a) or an additional deep p-well (b) shape the electric field at the pixel edges towards the collection electrode. The drawings are not to scale.

4.2 Analog front-end

The signal processing chain in the pixel comprises most importantly an amplifier and a discriminator stage. They have to be designed carefully in order to find a compromise between low-threshold operation and a sufficiently high signal-to-noise ratio. At the same time, the charge measurement and timing requirements of the desired application have to be taken into account. The general structure of signal processing in the TJ-Monopix design is shown in Figure 4.5. In the first stage, the charge signal Q_S collected on the detector capacitance in terms

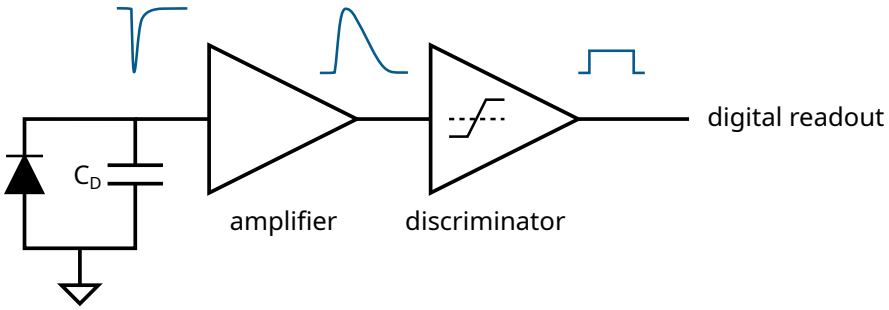

Figure 4.5: Signal processing chain in the analog front-end consisting of an amplification and discrimination stage. The length of the digital pulse is proportional to the measured charge.

of the voltage V_S is amplified and shaped in a way such that the following stage can determine the corresponding charge. This is achieved with a discriminator that produces a digital pulse upon the signal passing a predefined threshold. The length of this pulse is proportional to the deposited charge in the detector. By using a clock distributed to each front-end, the times of leading edge and trailing edge of the discriminator signal are stored in a memory cell for the read-out that is driven by the digital part of the chip.

4.2.1 Amplifier

Due to the small detector capacitance C_D of 3 fF [59] in the TJ-Monopix design, the voltage signal V_S is large, according to:

$$\mathrm{d}V_S = \frac{\mathrm{d}Q_S}{C_D} \,. \tag{4.1}$$

This facilitates the implementation of a voltage amplifier, instead of the more commonly used charge amplifier, in silicon pixel detectors. Apart from the sensor layout, the front-end design is based on the one of the ALPIDE chip [71, 72] as well. Compared to the first prototype TJ-Monopix1, transistor lengths in the front-end were adjusted for better performance. The size of the input transistor of the amplifier was enlarged to match resistances thereof and the feedback transistor which results in a 50 % increase of the gain. Most importantly, the capacitor (implemented by a transistor) between the source follower and the amplifier was increased by a

factor of 7.5 for better coupling to the input signal. This resulted in a gain increase by a factor of 2 and a significantly larger signal-to-noise ratio. The design process and comparison of the front-ends of TJ-Monopix1 and TJ-Monopix2 are treated in detail in [59].

4.2.2 Discriminator and charge measurement

The discriminator compares the analog output signal to a predefined voltage value and outputs a digital pulse when the signal is above this threshold. A global threshold (*GDAC*) can be set for the full matrix with a DAC of which the value is written in software and stored in a register in the chip. Each discriminator can be trimmed by the so-called *TDAC* (trim DAC), which is determined from three individually configurable bits stored in each pixel. The schematic of the discriminator stage is shown in Figure 4.6a. With a tuned amplifier response, the discriminator

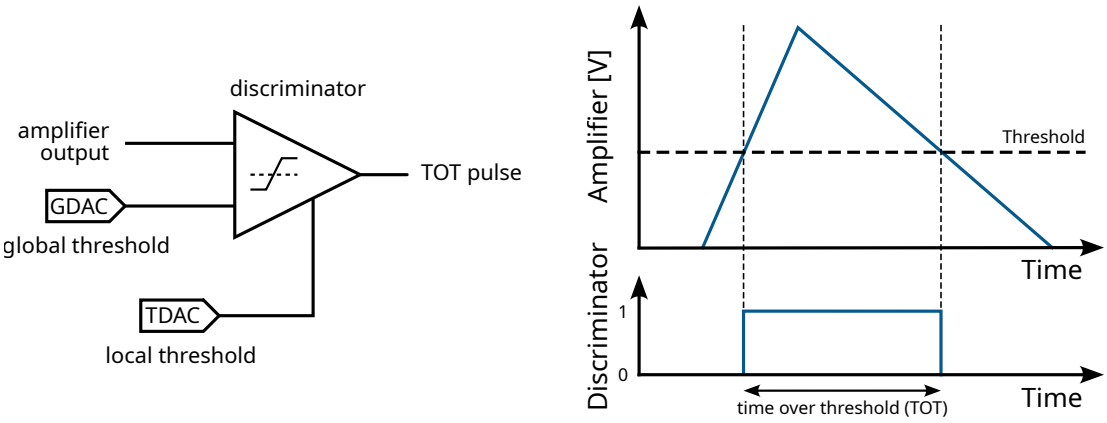

(a) In-pixel discriminator and threshold DACs.

(b) Time over threshold charge measurement.

Figure 4.6: (a) Schematic depiction of the discriminator stage in the analog front-end. The amplifier output is compared to a globally applied threshold (GDAC) and user-selectable threshold on pixel level (TDAC). (b) Charge measurement with time over threshold (TOT) method. The amplifier output is shaped such that the measured TOT is proportional to the deposited charge in the pixel.

can be used to measure the deposited charge in the detector. Simplified, the analog signal at the input of the discriminator follows a triangular shape. The passing of the threshold yields a leading and trailing edge of the resulting pulse which are sampled with a 40 MHz clock and subsequently stored in a memory cell. From their difference, the amount of deposited charge in the sensor can be measured in units of 25 ns. This value is referred to as *time over threshold* (TOT). Additionally, the discriminator output is routed through a network of OR gates to the bottom of each column (see Figure 4.10 for the matrix layout) to an output pad of the chip to make it available externally. This so-called `HitOr` signal is the fastest available response to a particle hit and can be used, for example, as trigger for measurements or sampled externally. The output signal is provided as logical OR of all pixels, which limits the use case to studies of single pixels.

4.2.3 Timing performance

Both amplifier and discriminator have a significant contribution to the time resolution σ_t of a pixel detector. For silicon pixel detectors, four underlying effects [73] can be identified:

$$\sigma_t^2 = \sigma_{\text{noise}}^2 + \sigma_{\text{ionization}}^2 + \sigma_{\text{distortion}}^2 + \sigma_{\text{TDC}}^2 \,, \tag{4.2}$$

where $\sigma_{\text{ionization}}$ is related to energy deposition in the sensor and can be separated into σ_{timewalk} and σ_{arrival} [4]. The contribution σ_{timewalk} arises from fluctuations of the signal amplitude that are governed by the energy loss distribution (Section 2.1.1.3). They introduce *time walk* due to different points in time of the threshold crossing in the discriminator as depicted in Figure 4.7. The second contribution to $\sigma_{\text{ionization}}$, σ_{arrival}, is often referred to as *Landau noise*.

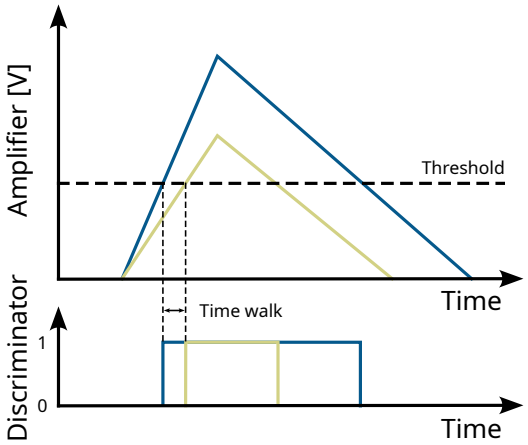

Figure 4.7: Time walk arises from different slopes on the rising edge of the amplifier. Small input signals cross the threshold later than large input signals. The return rate to the baseline is typically independent of the charge signal.

It describes the effect of non-uniform charge carrier generation along the particle track through the sensor. Depending on the position in the sensor, the drift time varies and consequently the time structure of the induced signal. This is strongly related to the thickness of the device with less time uncertainty in thinner devices. In addition, as described in Section 2.2.4, the charge signal varies with its drift velocity and weighting field. The implications of these effects are described by $\sigma_{\text{distortion}}$, which implies that the sensor geometry has to be taken into account when determining the temporal resolution.

Apart from these physics-related effects, the signal processing adds an uncertainty σ_{TDC} due to the resolution of the time-to-digital converter (TDC) and σ_{noise} due to electronic noise on the signal. Figure 4.8 shows the influence of the latter on the time resolution. It can be seen that a fast amplifier and/or large signal-to-noise ratio is beneficial for a good time resolution. The TDC contribution can be minimized easily, compared to the others, by using devices operating in the GHz range.

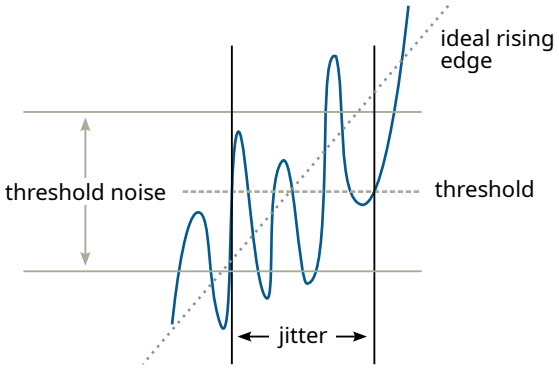

Figure 4.8: Electronic noise on the rising edge (blue) and on the threshold voltage (yellow) moves the time of the threshold crossing of the signal resulting in a jitter of the leading edge of the discriminator.

In addition to the time resolution, it is oftentimes useful to determine the percentage of hits that arrive *in-time*, as this ultimately defines the time performance as a tracking detector. The in-time definition, in accordance with ATLAS ITk outer layer specifications, requires hits to arrive within 25 ns. Consequently, the in-time threshold is the minimum amount of charge that is required for a hit to arrive within this time frame. The difference between in-time threshold and overall threshold is called *threshold overdrive*.

4.2.4 Power consumption

With increasing requirements of detectors for particle physics experiments concerning their spatial resolution, readout speed and logic density, ultimately the power consumption increases. On the other hand, the requirements on power consumption of the individual detectors are made stricter in order to reduce the material budget that comes with cooling solutions. For a good detector performance, a high signal-to-noise ratio S/N is beneficial. The equivalent noise charge (ENC) is defined as the input signal in units of electrons that creates a signal as large as the observed noise at the output of the amplifier. From there, the signal-to-noise ratio can be expressed as [74]:

$$\frac{S}{N} = \frac{Q}{qENC} \tag{4.3}$$

with Q the input charge, q the electron charge and ENC the input-referred equivalent noise charge. The latter is dominated by the thermal noise ENC_{th} of the first transistor gain stage. Plugging in the expression for ENC_{th} from [75] yields for the circuit at hand [59]:

$$N \propto \frac{C_{\mathrm{tot}}}{\sqrt{g_m}}\,, \tag{4.4}$$

where C_{tot} is the total capacitance of the system, that is dominated by the detector capacitance C_D and g_m denotes the transconductance of the input transistor. The latter scales with a power of the bias current and it follows [74]:

$$\frac{S}{N} \propto \frac{Q}{C_D}\sqrt{g_m} \propto \frac{Q}{C_D}\sqrt[k]{P} \quad \text{with} \quad 2 \leq k \leq 4\,. \tag{4.5}$$

Additionally, for the rise time of the amplifier output and consequently the time resolution, the following dependency holds [76]:

$$\tau_{\text{rise}} \propto \frac{C_D}{g_m} \propto \frac{C_D}{\sqrt[k]{P}} \tag{4.6}$$

with the same k as in 4.5. It can be seen that the small detector capacitance of TJ-Monopix2 of 3 fF is beneficial for low-power operation. Compared to a large-collection-electrode design, the required power of the front-end can be reduced to achieve the same signal-to-noise ratio. The same conclusion holds for the rise time and consequently the time resolution.

4.2.5 Coupling of input signal

In TJ-Monopix2, the charge signal can be coupled directly (DC) or via a capacitor (AC) to the front-end electronics. The standard approach is DC-coupling since it does not add a capacitance to the input node, and therefore provides a larger voltage signal, compared to the AC-coupled case. At the same time, since the collection n-well is connected to the amplifier input, the potential that can be applied to it is limited. It cannot exceed 1.8 V and is often lower because it defines the input baseline to the front-end. Part of the matrix consists of pixels that incorporate a capacitor implemented within the metal layers of the chip to AC-couple the collection node to the front-end. With this approach, the baseline of the amplifier input is set independently of the potential on the collection electrode. The latter can typically be as high as 50 V and potentially lead to more depletion of the sensor.

4.2.6 Test features

TJ-Monopix2 is equipped with features for characterization and debugging purposes. A charge injection circuit allows for artificial charge injection at the input of the amplifier to mimic charge deposition in the sensor. The schematic of the charge-injection circuitry is shown in Figure 4.9. Upon an injection pulse with amplitude V_{inj}, charge is accumulated on the injection capacitance C_{inj}. Since it is connected in series with the detector capacitance C_D, the injection capacitance has to be much smaller in order to maximize the charge at the input node. In TJ-Monopix2 its value is 230 aF, extracted from simulation [59]. Through a register setting, the time of injection can be adjusted with respect to the 40 MHz clock distributed across the matrix with a precision of 3.125 ns. The injection voltage V_{inj} and other currents and voltages steering the front-end

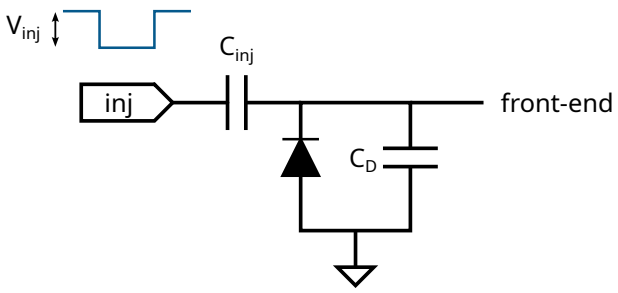

Figure 4.9: Injection circuit in TJ-Monopix2. A negative voltage pulse accumulates charge on the injection capacitor. Its capacitance must be significantly smaller than C_D in order to maximize the signal at the front-end.

are generated from configurable 8-bit DACs. The resulting signals can be measured externally or overwritten through dedicated pads on the chip.

The matrix contains eight special pixels: four located in the top left, and four in the top right corner of the matrix. They are not connected to the digital readout, but their analog signal can be accessed through pads connected to the carrier PCB. Details about the different pixel designs and implementation for analog output can be found in [59].

4.2.7 Matrix flavors

With the aforementioned coupling variations of pixels and two slightly different front-ends, the matrix is made up of four different pixel flavors. The largest part (448 out of 512 columns) is occupied by DC-coupled pixels, half of it with a front-end that is referred to as *standard front-end* and the other half with pixels including an additional cascode transistor (*cascode front-end*). The latter is supposed to increase the gain, compared to the standard front-end, by a factor of 1.6 [59]. At the side of the matrix, the remaining 64 columns implement the same two front-ends as AC-coupled flavors in 32 columns each. Figure 4.10 summarizes the different pixel flavors and their location in the matrix.

4.3 Digital design of TJ-Monopix2

Part of this work included the design of the digital periphery of TJ-Monopix2. It is responsible for processing and formatting the data recorded in the individual pixels. At the same time, the digital periphery decodes configuration commands from the end user and performs the actual configuration of registers in the chip. The digital periphery is designed in a *hardware description language* (HDL) and synthesized into electrical circuits by software. Therefore, an overview of the digital features and working principles is given in this chapter, focusing on functionality, usage, and limitations.

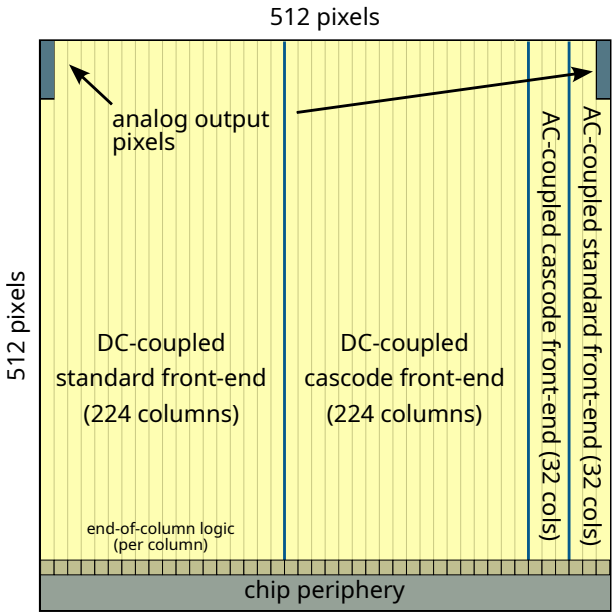

Figure 4.10: Schematic overview of the pixel matrix and the different flavors of the TJ-Monopix2. Each column has an end-of-column digital logic to process the column data. The data from all columns is combined in the chip periphery which also handles configuration and communication. The analog output pixels are located in the top corners, four per side. They are not related to the matrix area in which they are implemented.

4.3.1 Command decoder and configuration registers

To operate the chip with as few as possible input and output lines, the configuration logic and digital-to-analog converters (DAC) are included in the chip. This allows for using commercially available cables and a physically separated readout board with advantages in irradiation or beam test scenarios when there are no active components in the vicinity of the radiation and the mechanical mounting is easy and flexible. For this kind of setup with cable lengths of a few meters, differential data transmission is required. The differential transceiver is an implementation of an existing pseudo-LVDS driver [77]. With the help of a command decoder, the minimum number of data lines is reduced to four. An overview of those (and optional signals for further measurements or debugging) is given in Table 4.1.

The command decoder is used to write and read configuration registers, send pulses to the injection circuit, and configure the individual pixels for masking and local threshold DACs. The commands are made up of 8-bit data words that are transmitted serially at 160 MHz where one command can be composed of multiple thereof. The implementation and command set is taken from the RD53B readout chip [79] to ease with integration and usage.

The configuration is stored in the chip in form of a register consisting of 16-bit words and a unique address. This way, each register can be written by the command decoder individually and read in the same fashion. Some settings require more than the available 16 bits and are

Signal	Description	Direction
CMD_CLK	Command clock, running at 160 MHz in sync with CMD	input
CMD	Serially transmitted 8-bit command words	input
SER_CLK	Serializer clock, running at 160 MHz or optionally at 320 MHz. Used to clock out DATA words	input
DATA	8b10b encoded data stream [78]	output
HITOR	Optional fast HitOr signal (discriminator output) of selected pixels, routed through an additional cable (see Section 4.4.1)	output
INJ	Optional injection pulse, usually not used in favor of internal injection command	input

Table 4.1: Overview of the data lines for operation of TJ-Monopix2. Required signals are supplied via DisplayPort connectors on the single-chip card (see Section 4.4.1).

spread across multiple registers. For example, enabling the clock distribution along each double column is saved for each double column and therefore a 256-bit value that is spread across sixteen configuration registers with 16 bits each. There are 219 registers in total for 112 configurable boolean options and integer values. Three special registers control the pixel configuration and are explained in the following section.

4.3.2 Pixel configuration

Each pixel has a 3-bit in-pixel threshold DAC (TDAC) to adjust the local threshold in order to reduce the threshold dispersion over the whole matrix. A value of 0 masks the pixel for recording any hits, which leaves the user with seven possible threshold settings. A value of 4 denotes the default with lower values lowering the threshold and vice versa. A functional diagram of how the individual pixels are configured is shown in Figure 4.11.

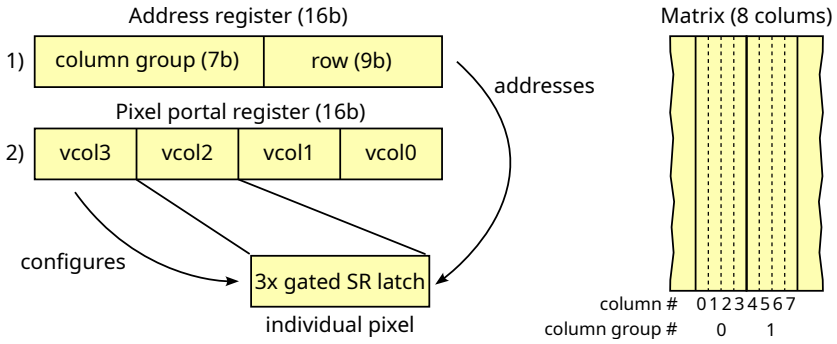

Figure 4.11: (left) Functional diagram of the pixel configuration logic and register interpretation. In the first step, the address in terms of column group (see right-hand figure) and row is written into the address register. In the second step, the individual pixels are configured when writing the configuration into the *pixel portal* register. (right) Addressing of the columns in terms of their column group.

For configuration of the individual pixels, the matrix is segmented into column groups of four consecutive columns each, in the following referred to as *virtual columns* (*vcol*). Their actual location in the matrix is determined by a 16-bit address register. It can be accessed to write the row number and corresponding column group where the pixel that is to be configured is located (step 1 in Figure 4.11). In a second step, the configuration values for the virtual columns are written into the so-called *pixel portal* register. Writing to the *pixel portal* register triggers a state machine, that processes the address and configuration values and sets the three SR latches for each of the four pixels, which store the threshold DAC value. Masking pixels works in the same fashion, since one possible value out of the eight possible combinations of three bits corresponds to a masked pixel. This allows for an individual masking of each pixel.

In addition, each pixel can be toggled to accept a charge signal produced by an injection circuit outside the matrix and distributed along the columns. This option is set on a column and row basis so that multiple pixels can be activated at the same time when the selected column and row lines intersect, as shown in Figure 4.12. Enabling the injection patterns is implemented

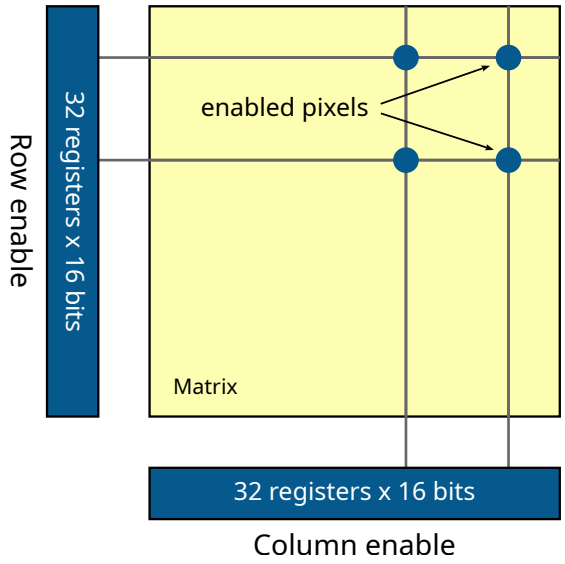

Figure 4.12: Schematic depiction of how individual pixels are enabled for artificial charge injection or `HitOr` output in TJ-Monopix2. Individual columns and rows can be set with two register blocks and pixels at intersecting columns and rows are enabled.

as described above, with 32 registers of 16 bits – one bit for each of the 512 columns – and another 32 registers of 16 bits for rows. The `HitOr` output (see Section 4.2) is configured in the same fashion. Since the `HitOr` signals of all pixels are combined using a logical OR in the periphery, one must ensure that only one pixel is enabled for `HitOr` measurements or only one hit occurred at a time, so the measurement can be correlated to the actual hit information (i.e. column, row and charge).

4.3.3 Data transmission

Output from the chip is provided in a common data stream for all types of data. To differentiate between data from actual detector hits and data from reading back registers, these two types of information will be referred to as *hit* and *register words* in this section. A regular hit word consists of 32 bits, while a register word consists of 24 bits – the structure is shown in Table 4.2.

	Column (8b)			Leading edge (7b)			Trailing edge (7b)			Row (10b)		
Bit	31	...	24	23	...	17	16	...	10	9	...	0

(a) Bit-wise structure of hit words.

	Address (8b)			Value (16b)		
Bit	23	...	16	15	...	0

(b) Bit-wise structure of register words.

Table 4.2: Structure of (a) hit and (b) register words on bit-level. Interpretation needs to be aware of the type of data which is therefore encoded in the frame header (see below). Since the matrix is designed with 256 double columns and 1024 rows each, the row number of a hit consists of 10 bits, and the column number of 8 bits. The mapping to regular x-y coordinates is done in software during interpretation. Register address and value are read back in one block and mapped to a named register in software.

Hit and register words are placed into separate FIFOs in the chip's periphery when they are fully processed. The serializer then pulls and transmits the data to the readout board. In this process, register words are read out with lower priority than hit words to prevent overflow of the FIFO and possible data loss at high hit rates.

The 8b10b protocol [78] transmits data octets (8 bits) in 10-bit blocks that provide a DC-balanced data stream where 0 and 1 occur at the same rate in the data stream, but not necessarily in a single 10-bit word. Apart from possible capacitative coupling this transmission method allows for error detection to a certain extent since the number of allowed combinations in 8b10b encoding is smaller than the number of possible combinations ($2^{10} = 1024$). In the worst case scenario, a hit is sent out before data of a following hit is ready for transmission, which means that the 32-bit data block is separated into 4 octets and padded with an 8-bit header (*start of frame* (SOF)) and trailer (*end of frame* (EOF)), identifying multiple octets as a full frame at the receiving end. The overhead due to the encoding for hit and register words

SOF	Block 1	Block 2	...	Block n	EOF

Table 4.3: Structure of the transmitted data encoded as 8b10b frames. Each block consists of 10 bits that encode 8 bits of actual chip data. A frame can hold more than one hit or register word but they cannot be mixed.

(transmitted separately) is depicted at the top in Figure 4.13. At a 160 MHz output data rate

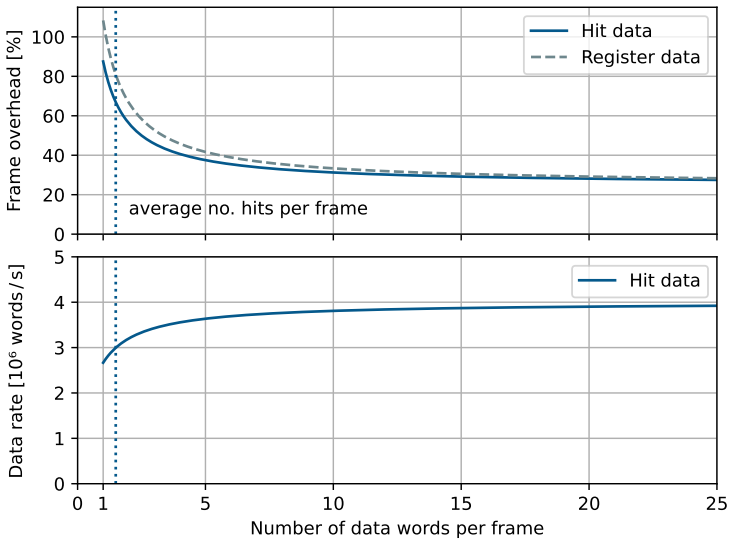

Figure 4.13: Top: overhead from encoding and frame identifier (SOF and EOF) for data transmission depending on number of register and hit words per frame. The lower bound is at 25 % due to the 8b10b algorithm. Bottom: Number of hit words per second that can be transmitted depending on the number of hits per frame. This number varies in an experiment depending on hit rate and processing time in the matrix and periphery. Shown is the average number of hits per frame in a typical beam test environment with a hit rate of a few kHz.

approximately 2.7 million hit words per second (wps) can be transmitted out of the chip with only one hit per frame according to:

$$\text{wps}\,(n) = \frac{160\,\text{MHz} \cdot n}{32 \cdot n + 8 + 8}\,\frac{8}{10} \tag{4.7}$$

with n the number of hits per frame. The result depending on n is shown in the bottom of Figure 4.13. This value is solely determined by the output logic and encoding, and is not related to the readout capabilities of the matrix. While the value quoted above is a worst-case scenario, the effective transmission rate can be higher (when multiple hits are combined in one frame). It is evident that the data transmission out of the chip is a bottleneck for the readout rate as the readout logic of the matrix (see [80]) can handle hit rates of more than $100\,\text{MHz}\,\text{cm}^{-2}$ [59, and references therein]. For measurements in a particle beam at a typical beam rate of a few kHz, the average number of hits per frame is approximately 1.5 resulting in an overhead of 67 %.

It should be noted that register words are usually read out individually and rarely, which produces a relatively large overhead for the single frame according to Figure 4.13, but almost no contribution to the overall data rate limit.

4.4 Data acquisition system

A dedicated data acquisition (DAQ) system for readout and configuration of TJ-Monopix2 is designed with ease of setup and operation in mind. The system consists of hardware to mount and connect TJ-Monopix2 chips to a pre-existing readout board hosting a commercial FPGA that acts as an interface between a DAQ computer and the device under test. A brief overview of the features of the readout board and its FPGA firmware presents its functionality for communication with TJ-Monopix2 and auxiliary hardware, for example, for beam tests. The DAQ system is complemented with a specific software package that acts as a user interface for operation of TJ-Monopix2 and abstracts the firmware component from the end user.

4.4.1 Hardware

The hardware part of the DAQ system consists of two separate components. One is a printed circuit board (PCB) on which TJ-Monopix2 chips are mounted with connectors for applying operating voltages, communication with the readout board, and debugging purposes. The second component is a readout board which houses a commercial FPGA, taken from an existing DAQ system designed for testing readout chips developed for the ATLAS ITk pixel detector [81].

A dedicated PCB is designed to connect the bare silicon chip to the DAQ system and is shown in Figure 4.14. It provides an area to glue the chip on and pads for wirebonding the 466 input and output connections of the chip to the PCB, which are located on three sides around the chip gluing area. A cutout in the PCB below the chip reduces the material budget for tracking applications, for example, beam tests (see Section 5.1). There are no active components on the board, which are susceptible to radiation damage, for example, in irradiation campaigns. Multiple pin headers are used to set chip parameters, measure internal or supply external DAC voltages to the chip. Data lines for input and output are routed through a DisplayPort connector with five LVDS lines. The fast `HitOr` signal (see Section 4.2.2) is routed through an additional DisplayPort connector, connected to a second port on the readout board. Supply voltages of 1.8 V for the analog and digital domains, as well as for the DACs, and periphery of the chip are applied by an external power supply. Bias voltages are applied through LEMO connectors on the right side of the board. The PCB provides four output channels on the left side for measurements with and debugging of the analog output signal from dedicated test pixels on the chip. Pin headers on the top can be accessed to measure DAC currents and voltages, or provide them externally. Since the RD53B command set supports addressing of multiple chips connected to one readout board via a chip ID, it can be selected by placement of a jumper.

The readout board was designed in the framework of BDAQ53 [81], a DAQ system for pixel detector readout chips developed in the RD53 collaboration. It consists of a custom PCB that hosts a commercial Mercury+ KX2[3] FPGA board and a variety of input and output connectors. Typical use cases of this setup are lab and beam test measurements, since it requires a small

[3] `https://www.enclustra.com/en/products/fpga-modules/mercury-kx2/` (visited on 17.08.2023)

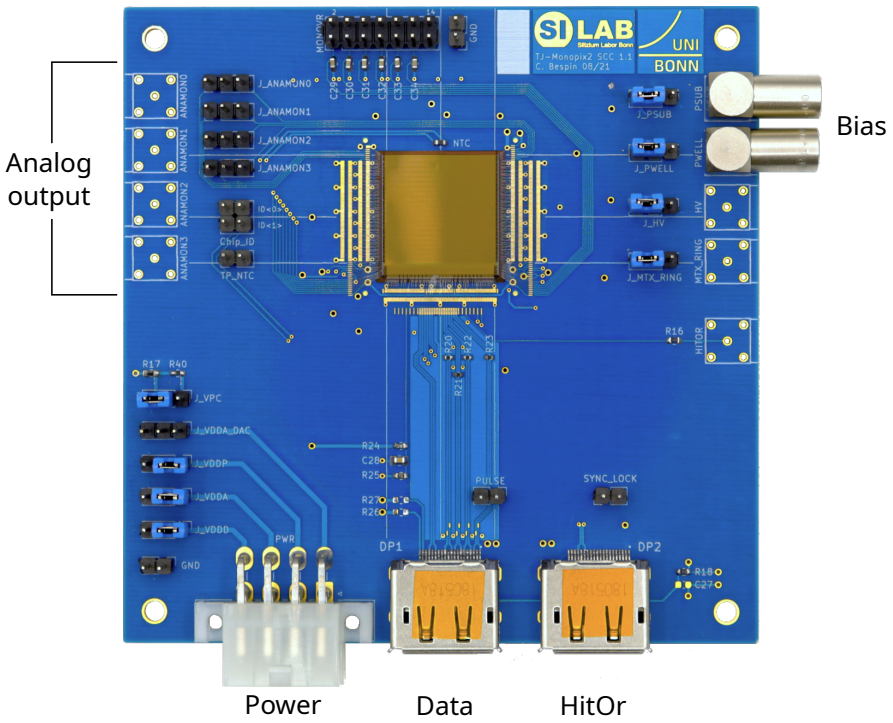

Figure 4.14: Photograph of the single-chip carrier board with a mounted TJ-Monopix2 chip, annotated are the most important input and output connectors for regular operations.

amount of space, power supplies, and cables. Because of the low output data rate of TJ-Monopix2 compared to the originally supported readout chips in BDAQ53, only one of the DisplayPort connectors can be used for data readout. The remaining ones are connected to high-speed receiver channels of the FPGA that are not compatible with TJ-Monopix2 data rates. In the future, a modification of the readout board could provide parallel readout of multiple chips. The readout board is connected to the data acquisition computer with a 1 Gbps ethernet connection.

4.4.2 Firmware

The custom firmware for the FPGA is built on top of the `basil` firmware modules publicly provided in [82]. It follows a modular approach that can be separated into modules responsible for communication with the chip, data processing, and communication with the DAQ computer. The latter is achieved by using different protocols for configuration of the firmware modules (UDP) and data transmission to and from the chip (TCP).

A block diagram of the most important firmware parts is presented in Figure 4.15. At the core of the firmware is the data receiver that accepts the 8b10b encoded frame data [78] from the chip and decodes it to separate hit information and register read values from the data

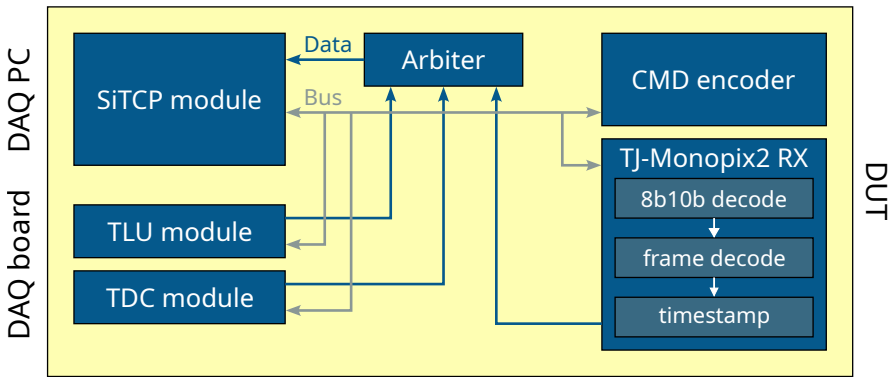

Figure 4.15: Block diagram of the most important building blocks of the FPGA firmware for the readout board. A bus system (colored in gray) is used for configuration of the individual firmware modules while data (colored in blue) is transmitted via FIFOs and an arbiter to the DAQ computer via TCP.

stream. The hit information is tagged with a 52 bit-timestamp that is sampled at arrival time of the corresponding frame and then combined into 32 bit-data words with headers, identifying timestamps, start and end of hit words and register data. All DUT-related data is placed in a FIFO register to be pulled from the later data processing stages. The chip can also provide a `HitOr` signal, as described in Section 4.2.2, that corresponds to the discriminator output of a pixel and therefore the measured charge. It can be sampled with a time-to-digital converter (TDC) running at 640 MHz to get more precise charge and time information. For measurements in particle beams, a trigger logic unit (TLU) is usually necessary. Details of such a setup will be given in Section 5.1. To record the data provided by the TLU, a specific module is required. It performs a data handshake with the TLU to process and receive information about the current trigger event recorded with a scintillator in the particle beam. This module is tailored to the type of TLU that is used and the available types of handshake and data transmission. Both the TDC and TLU modules attach a header, identifying the corresponding data words before storing them in their respective output FIFO registers. A round-robin arbiter pulls the individual FIFO data from the three aforementioned modules if there is any, and produces a continuous data stream of all data recording modules. This data stream is placed in another FIFO from where it will be sent out via TCP to the DAQ computer.

The readout board transmits data in two directions: (1) to the chip with commands for operation and configuration and (2) to the DAQ computer with data. The former is achieved exclusively with a command encoder module, a matching counterpart to the command decoder that is synthesized in the chip. Commands are put into a FIFO in the command encoder from which the commands are processed and transmitted. To speed up possible repetitions of a series of commands such as continuous charge injections, the firmware supports looping commands on the FPGA level. The command encoder is driven by a configurable low-jitter `Si570` oscillator on the readout board matching the 160 MHz command frequency.

Communication with the DAQ computer is realized via both UDP and TCP connections. The former is used to access the bus system of the firmware modules for configuration and control because of its low overhead and high speed. It comes at the disadvantage of lacking error checks or data ordering. However, these are not required for the purpose at hand. Chip data that is acquired during operation, mainly hit information and read register data, are transmitted via TCP because of its reliability concerning handshakes, error correction capabilities, and data ordering. A dedicated module for the supported Kintex7 FPGA series is used to achieve proper usage of the TCP protocol [83].

Additional modules provide options to configure the readout board or get temperature measurements from an NTC mounted close to the DUT on the carrier PCB.

4.4.3 Software

The control software for data taking is written in `Python` and the general structure is adopted from the `bdaq53` project as well[4]. It relies heavily on `basil` [82] that provides software interfaces for the respective firmware modules. The specific software parts for the command encoder and custom data recording are included in the DAQ software that is publicly available[5]. A `ScanBase` class provides basic methods and attributes that are required for each individual scan. Individual chips are instances of a `tjmonopix2` class and attributes of the `ScanBase` that make them available during scans. This approach enables possible implementation for reading out more than one chip at the same time when multiple instances of a chip object are connected to the `ScanBase`. So far, this is not supported in hardware as explained in Section 4.4.1. For configuration of the readout board, another class `bdaq53` can be used in order to control different firmware modules and settings. The software is completed by multiple analysis and plotting functions that provide the user with measurement-dependent result values and figures. Figure 4.16 shows the different software components and their relation to each other.

All currently available scans in the software package are listed in Table 4.4. This list does not assume completeness since user-specific scans can easily be added; it provides the basic set of measurements for detector characterization.

4.5 Specification summary of TJ-Monopix1 and TJ-Monopix2

Table 4.5 summarizes the specifications of TJ-Monopix1 and TJ-Monopix2. Relevant values and features are compiled to highlight the most important differences.

[4] `https://gitlab.cern.ch/silab/bdaq53`
[5] `https://github.com/SiLab-Bonn/tj-monopix2-daq`

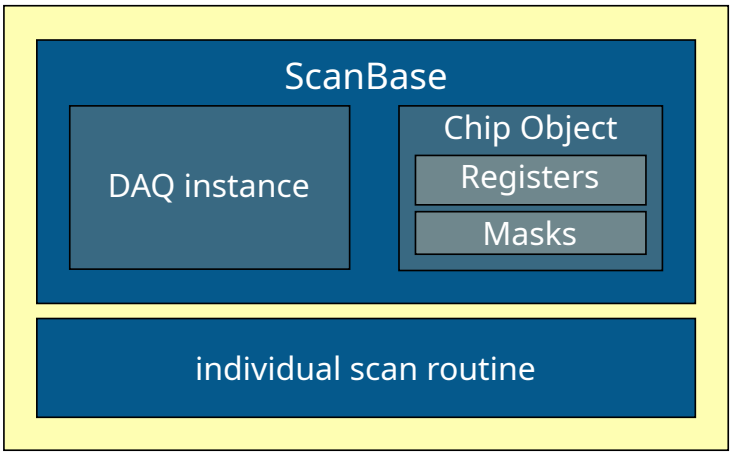

Figure 4.16: Structure of the DAQ software. Every scan is derived from a common `ScanBase` that provides access to configure the readout board and the chip. Current register settings and masks for the individual pixel configuration are stored in software. The scans differ by their measurement routines that are implemented on a case-by-case basis.

Name	Description
Analog scan	Injection of fixed charge into the pixel matrix, usually used for testing the general functionality
Threshold scan	Injection of varying charge to detect the threshold when each pixel starts responding
Global threshold tuning	Coarse tuning by changing global front-end parameters to a desired (mean) threshold
Local threshold tuning	Fine-tuning on a per-pixel basis using the local trim DAC (see Section 4.2.2) to homogenize the threshold of all pixels
External trigger scan	Measurement with a trigger logic unit (TLU supplying an external trigger signal to the DAQ board)
Source scan	Basic measurement recording every incident particle, e.g., from radioactive sources

Table 4.4: List of available scan routines in the TJ-Monopix2 DAQ software. Only the most general scans are listed and briefly described. Additional scans are available or can be implemented easily using the software structure for more specific measurement purposes.

	TJ-Monopix1	TJ-Monopix2
Chip size	2 cm × 1 cm	2 cm × 2 cm
Pixel size	40 µm × 36 µm	33.04 µm × 33.04 µm
Number of pixels	448 × 224	512 × 512
Matrix size	17.92 mm × 8.06 mm	16.92 mm × 16.92 mm
In-pixel threshold DAC	–	3 bits
Matrix clock	40 MHz	40 MHz
TOT resolution	6 bits	7 bits
I/O	CMOS	LVDS
Data output rate	40 MHz	160 MHz
Data encoding	–	8b10b

Table 4.5: A selection of TJ-Monopix1 and TJ-Monopix2 specifications concerning dimensions and features.

5 Measurements in particle beams

Measurements of detectors in particle beams provide the ability to characterize them with regard to detection efficiency and charge measurement with minimum-ionizing particles (see Section 2.1), among others. Since particle trajectories are required for efficiency measurements, the material budget in the so-called *beam telescope* for track reconstruction should be minimized to allow particles to pass all detector planes with minimal scattering.

5.1 Beam telescope setup

A beam telescope setup is a measurement device that consists of multiple detectors and is used to reconstruct trajectories of individual particles. These trajectories or *tracks* are used as reference to determine if the *device under test* (DUT) mounted in the beam telescope (see Figure 5.1 for a schematic setup) detected a hit at the correct position and at the correct time. In order for this to work, a particle beam is necessary, that passes the whole beam telescope without absorption or any other type of beam loss, for example, from scattering.

A EUDET-type beam telescope [84] consisting of six detector planes is used for particle tracking, operated with a `Python`-based readout system [85]. The planes are built from 50 µm thick Mimosa26 monolithic active pixel sensors [86] featuring a pixel pitch of 18.4 µm × 18.4 µm. The telescope can achieve track resolutions below 2 µm for a *device under test* (DUT) positioned in between the center telescope planes [87]. Pixels are read out using a rolling-shutter readout with 115.2 µs frame time, providing hit information in the form of one "picture" for the entire matrix at this frequency. This integration time limits the time resolution of the tracks, although precise tracking requires a better time resolution. An additional FE-I4 detector designed for the ATLAS Inner Detector [88, 89] is used for time-tagging of tracks with 25 ns time resolution. The additional time reference detector has a pixel pitch of 50 µm × 250 µm which is larger than the telescope planes that provide much better spatial resolution. Based on spatial matching, the telescope tracks are tagged with a precise timestamp from the time reference detector. This results in reconstructed tracks with both low spatial resolution and sufficiently high timing resolution. The DUT is mounted on the carrier PCB above a cutout (see Section 4.4.1) to minimize the material budget. It is placed in the center of the telescope to achieve the optimal track resolution.

All detectors, including the DUT, are connected to a trigger logic unit [90], which provides a common trigger signal when a particle traverses the scintillator in front of the telescope. A

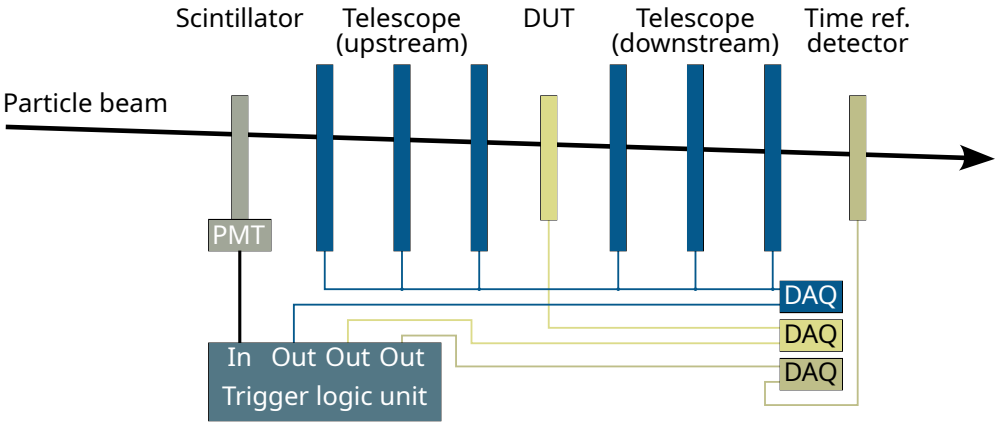

Figure 5.1: Setup of a beam telescope for efficiency measurements. A scintillator in front of the telescope is used together with a TLU to distribute trigger signals to the DAQ systems upon passage of a particle. The DUT is placed in the middle of the telescope for optimal tracking resolution. A dedicated time reference detector is used for time-tagging of particle tracks with 25 ns resolution.

schematic of the full setup is shown in Figure 5.1. At the DESY II test beam facility [91], where the experiments presented in this work were conducted, users can select the beam energy in the range of 1 – 6 GeV. In order to minimize the material scattering according to (2.20), an energy of 5 GeV is chosen. Since the beam rate decreases with increasing energy, this setting is a compromise between minimizing multiple scattering and achieving high statistical precision within a given time frame.

Irradiated devices are mounted inside a styrofoam box, which serves as a cold box to cool the DUT while adding minimal material to the beam telescope setup. For the cooling, nitrogen gas is cooled down with dry ice and fed into the styrofoam box. This setup allows DUT temperatures to reach −20 °C, which helps to limit leakage current and therefore noise in the detector [92].

5.2 Track reconstruction and analysis software

The DAQ board records the timestamp of hit information from the detector as well as from trigger information from a TLU, independently of each other. Since the DUT does not support triggering, unlike the other detectors in the beam telescope, all recorded hits are read out. This includes hits possibly uncorrelated to the ones detected in the other planes. By a later offline analysis, detector hits are assigned to the recorded TLU signals based on their timestamps. This process is referred to as *event building*. For later track reconstruction and hit detection efficiency measurements, the `beam telescope analysis` software package [93] 3 is used. It performs pre-processing of hits such as clustering, and alignment of the individual detectors in the beam telescope as well as track reconstruction and efficiency calculation.

5.2.1 Event building

An event is defined as a particle passing the scintillator in front of the telescope. It contains all recorded detector hits that are correlated with this incident particle. The TJ-Monopix chips operate without trigger logic, which means that all registered hits are recorded in the DAQ, tagged with a timestamp (see Section 4.4.2) and saved to disk. Sorting hits into events that correlate with a scintillator hit and a subsequent trigger signal in the DAQ software is performed offline. Due to data propagation and processing in the DUT, the exact time delay between the actual hit detection in the chip and its arrival in the DAQ system relative to the scintillator is unknown. A unique association is not possible, which adds a systematic uncertainty to the efficiency calculation. Both underestimation and overestimation of the hit detection efficiency ϵ are possible, if correlated hits are not associated with the event or if uncorrelated hits are incorrectly associated. Exact uncertainties require detailed studies and simulations, but the following calculations give an estimate of the impact of the above-mentioned event building on the hit detection efficiency.

New triggers following the one that defines an event are vetoed within a time frame t_{veto} that is configured to be long enough to process all the hits in the DUT before the next event. This prevents data hits from being recorded after the next trigger signal and artificially limits the trigger rate of the whole system. All hits that arrive within the time $t_{\text{event}} = 10\,\mu\text{s} < t_{\text{veto}} = 12.5\,\mu\text{s}$ are assigned to the corresponding event. Calculating the underestimation of efficiency, i.e. not assigning proper hits to the event requires detailed information about the time structure of the signal processing on the chip. The more important aspect, the assignment of random hits to the event (leading to a higher efficiency than the actual one) can be estimated more easily. With a beam rate r_{beam} on the sensor, the probability P of k particles that are not correlated with a track hitting the detector within this time window is given by a Poisson distribution:

$$P_{\text{beam}}(k) = \frac{\lambda_{\text{beam}}^{k}}{k!}\, e^{-\lambda_{\text{beam}}} \tag{5.1}$$

with

$$\lambda_{\text{beam}} = r_{\text{beam}}\, t_{\text{event}}\,. \tag{5.2}$$

If there is an event defined by the scintillator and the telescope, but no hit recorded in the DUT, the total probability of N random beam hits (for example from scattered particles) that could increase the hit detection efficiency is given by the sum:

$$\sum_{k=1}^{N} P_{\text{beam}}^{\text{uncorr}}(k) \overset{N\to\infty}{=} 0.039\,, \tag{5.3}$$

where a typical trigger rate of 4 kHz was chosen for the numerical calculation. Additionally, noise

hits can artificially increase the efficiency if they pass the hit criterion as defined in Section 5.2.3. The probability P_{noise} of a noise hit occurring in the event window t_{event} and being associated with an event is determined by the noise occupancy of the detector. It is defined as the amount of noise or background hits per time that occur during a measurement. It can be calculated by performing a measurement without any signal (i.e. no beam or radioactive source) and counting the recorded hits. Figure 5.2 shows the typical noise occupancy of TJ-Monopix2 in beam test conditions (front-end settings and environment). The average number of all background hits

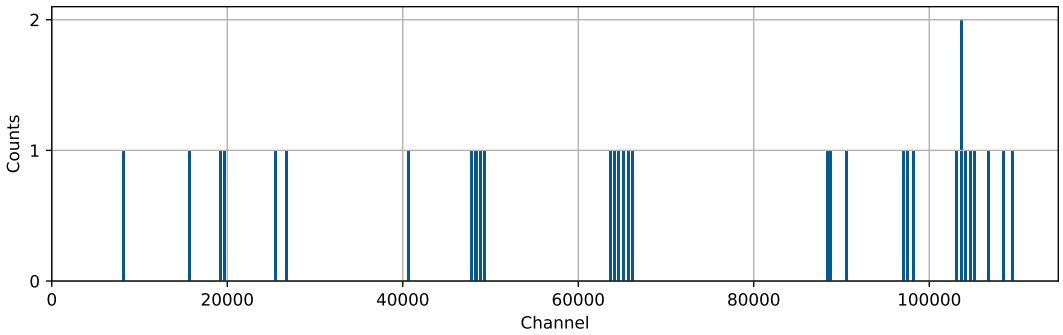

Figure 5.2: Typical noise occupancy of the DUT in beam tests. The measurement time is 300 s and the total number of noise hits is 51. The x-axis corresponds to the pixel channel, a linearized form of the matrix according to channel = column coordinate $\times$ n_{rows} + row coordinate.

recorded during a 300 s long measurement is 51. This results in an average noise rate r_{noise} per pixel per bunch crossing (25 ns) of:

$$r_{\text{noise}} = 5.4 \times 10^{-14} \,. \tag{5.4}$$

For simplicity, the noise distribution is also assumed to follow a Poisson distribution. The probability to record m noise hits on a sensor with n pixels during an event of length t_{event} is:

$$P_{\text{noise}}(m) = \frac{\lambda_{\text{noise}}^{m}}{m!}\, e^{-\lambda_{\text{noise}}} \tag{5.5}$$

with

$$\lambda_{\text{noise}} = n \cdot r_{\text{noise}} \cdot t_{\text{event}} \cdot 25 \times 10^{-9}\,\text{ns} \,. \tag{5.6}$$

The total probability of assigning a hit to an event that does not correspond to an actual particle passing the beam telescope is the sum of the two contributions:

$$P_{\text{total}}^{\text{misassociation}} = \sum_{k=1}^{\infty} P_{\text{beam}}^{\text{uncorr}}(k) + \sum_{m=1}^{\infty} P_{\text{noise}}(m) \,. \tag{5.7}$$

To calculate the effect of uncorrelated beam and noise hits on the efficiency, only those hits have to be considered, that are located within the association distance d_{assoc} (see Section 5.2.3) around the intersection of the reconstructed track and the DUT (see Figure 5.6). In this case, the probability P_{beam} has to be scaled to the association area $A_{\text{assoc}} = \pi\, d_{\text{assoc}}^2$ and the number of pixels n in (5.6) has to be replaced by the number of pixels within A_{assoc}. For TJ-Monopix2, an event window of 10 µs is chosen based on the available timing information, which is only recorded in the readout board. The overestimation of the efficiency in dependence of the noise rate per pixel per bunch crossing and the beam rate is depicted in Figure 5.3. According to the

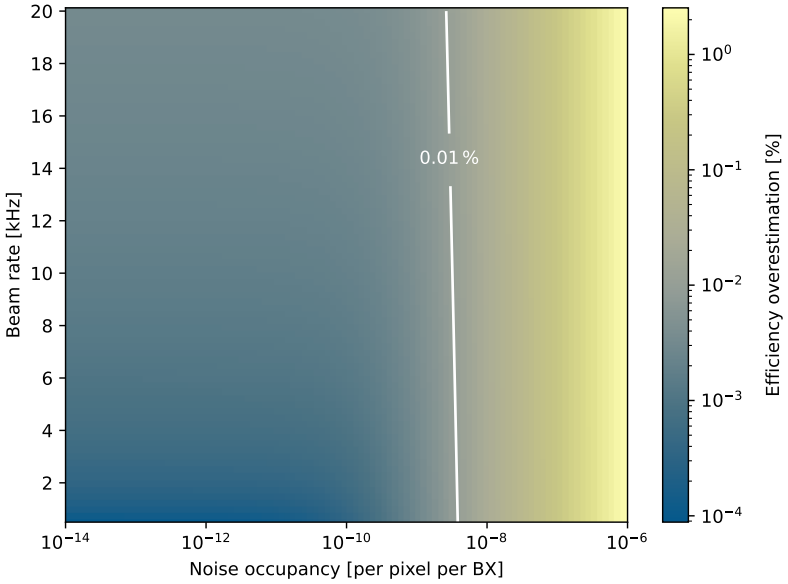

Figure 5.3: Efficiency overestimation for an event time t_{event} of 10 µs. For a noise occupancy above 10^{-8}, the overestimation increases rapidly to more than 1 %. Indicated in white is the limit at which the overestimation is 0.01 %. The typical noise occupancy for TJ-Monopix2 in beam tests is in the order of 10^{-14}.

values shown therein, the overestimation of the efficiency of TJ-Monopix2 is less than 0.01 % over a wide range of beam rates. In addition, this value decreases with increasing (true) efficiency of the device, as these calculations assume that there is no actual hit that was identified as such. Due to a different timestamping procedure of the hits in TJ-Monopix1, the event window is 2 µs for which the overestimation is smaller, even for irradiated sensors with a noise occupancy of about 10^{-9}.

5.2.2 Detector alignment and resolution

The detectors in a beam telescope are usually unintentionally shifted and rotated against each other due to the mounting precision. In the alignment procedure of the track reconstruction

software, the pixel coordinates of each detector are transformed to form a common coordinate system. Finding the translations and rotations is performed in two steps with coarse and fine alignment, the latter using a Kalman filter [94]. For each reconstructed track, the *residual* between the track intersection and the hit position at a given telescope plane can be calculated. An example distribution of the residual of the DUT is shown in Figure 5.4a. The residual is unbiased since the DUT is not included in the track reconstruction. With proper alignment, it

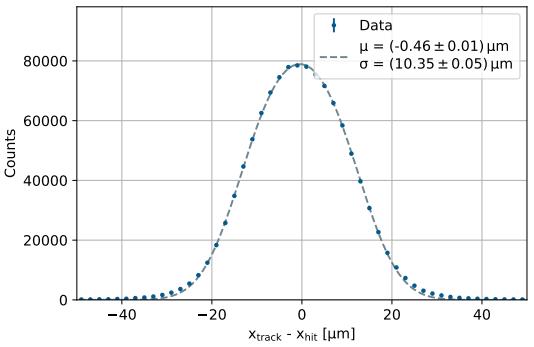

(a) Exemplary residual distribution for a device under test in a particle beam. It is centered around 0 with a Gaussian shape in the core of the distribution.

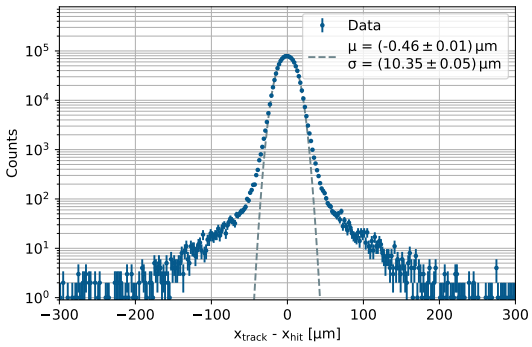

(b) Logarithmic scaling of the distribution in (a). Due to multiple Coulomb scattering, the tails are more pronounced compared to a Gaussian distribution. Background hits are visible over the whole plot range.

Figure 5.4: One-dimensional residual distribution of a device under test in a particle beam with minimum-ionizing particles. The distributions are centered around 0. From a Gaussian fit to the central part of the distribution, the spatial resolution can be determined. In this case, it is 10.35 µm, which includes the spatial resolution of the telescope tracks.

is expected to be centered around 0. Due to multiple Coulomb scattering (see Section 2.1.3), the tails are larger according to Molière theory. This can be observed with a logarithmic scaling in Figure 5.4b, where the background is visible. The spatial resolution of a DUT is defined as the standard deviation of the unbiased residual distribution.

Assuming binary hit information in a single electrode, integration over the uniformly distributed probability density of the impact position yields the term for the spatial resolution σ_{det} of the detector [4]:

$$\sigma_{\text{det,binary}} = \frac{p}{\sqrt{12}}\,, \tag{5.8}$$

where p denotes the pixel or strip pitch. In case of charge cluster formation due to the charge distribution exceeding the pixel size, the hit position can be determined more precisely by computing the geometrical center of the individual hits in the cluster. Additional energy information adds weights to the hits to compute the center of gravity, thus improving the position resolution even more. The finite pixel size generally leads to a residual distribution of a box function convolved with a Gaussian function. While it is more pronounced for pixel sizes in the

order of 100 µm, the flattening around the maximum in the distribution can be observed in both TJ-Monopix1 and TJ-Monopix2 with a pixel size below 40 µm as well. Figure 5.5 shows fits with a Gaussian function and with a Gauss function convolved with a box function (*Gauss-box*) to the example data. To restrict the comparison to the relevant central part of the distribution,

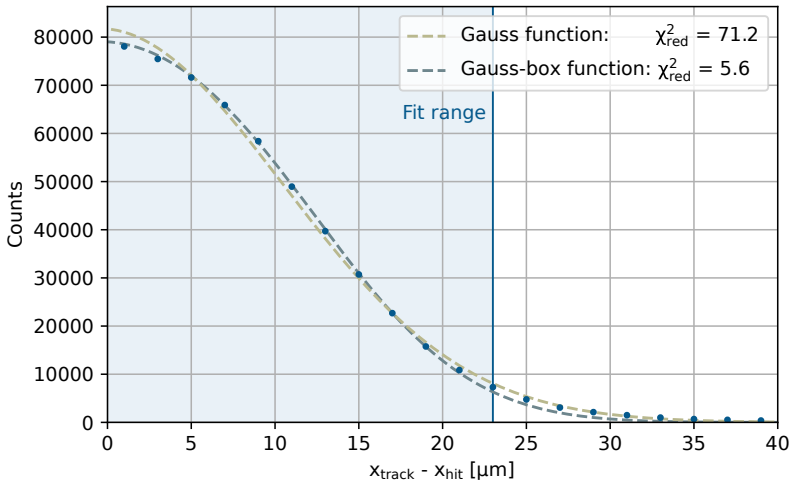

Figure 5.5: Comparison of residual distribution of data and different models, notably a Gaussian function and a Gaussian function convolved with a box function. The latter has smaller χ^2_{red}, which indicates a better match of the function to the data points. The shaded area shows the data points that are included in the fit. They correspond to the range where the number of counts is larger than 10 % of the maximum in order to reduce the impact of background and scattering effects.

the fit range is limited to the region where the number of histogram entries is larger than 10 % of the maximum value. The χ^2_{red} of the least squares fit is 71.2 and 5.6, respectively, which indicates that the latter is a better description of the data. Consequently, all stated spatial resolutions are extracted from a Gauss-box fit. The difference from the expected $\chi^2_{\text{red}} = 1$ is due to background and scattering effects that are not included in the model. The standard deviation σ_{res} of the residual distribution can be calculated from its variance:

$$\sigma^2_{\text{res}} = \text{Var}(x) = \int_{-\infty}^{\infty} x^2 \, f(x) \, \mathrm{d}x - \mu^2 \, , \tag{5.9}$$

where $x = x_{\text{track}} - x_{\text{hit}}$. A functional form for the probability density function f and the expected value μ is extracted from the fit. The integration is performed numerically and a `Python` package is used to propagate the uncertainties [95].

In the example in Figure 5.4, σ_{res} is (10.35 ± 0.05) µm, which is the quadratic sum of the detector (σ_{det}) and telescope track (σ_{tel}) resolution according to:

$$\sigma^2_{\text{res}} = \sigma^2_{\text{det}} + \sigma^2_{\text{tel}} \, . \tag{5.10}$$

The latter is both an intrinsic property of the beam telescope setup and depends on the quality of the track reconstruction. Typically, a track resolution of $2-3\,\mu\text{m}$ can be obtained with the given setup.

5.2.3 Efficiency calculation

A crucial parameter for a detector is the hit detection efficiency. It is defined as the ratio of detected hits in the DUT and tracks traversing the telescope, which is why a particle beam and track reconstruction is necessary for the measurement. With the number of tracks with DUT hits $N_{\text{tracks}}^{\text{DUT}}$ and the total number of tracks $N_{\text{tracks}}^{\text{total}}$, the efficiency is given by:

$$\epsilon = \frac{N_{\text{tracks}}^{\text{DUT}}}{N_{\text{tracks}}^{\text{total}}} \,. \tag{5.11}$$

In order to avoid noise hits being counted for the DUT hits, only those within a given area around the track intersection are taken into account. The similar pixel dimensions in both directions of the investigated detectors allow for a circular shape, of which the radius is chosen according to the residual distribution and will be referred to as *association distance*. Figure 5.6 depicts the

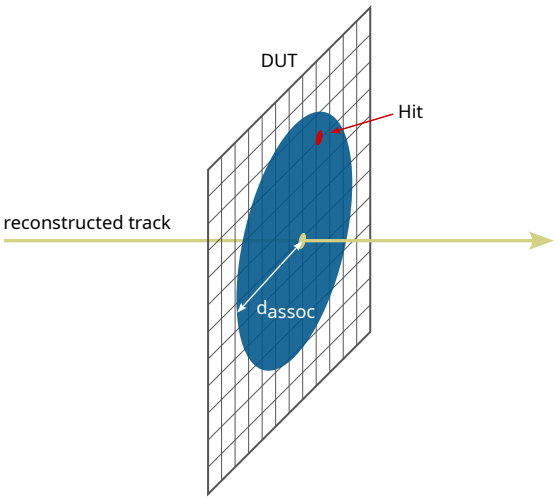

Figure 5.6: Hits (in red) within a circle of radius d_{assoc} around the track intersection with the DUT are associated to the tracks and count towards $N_{\text{tracks}}^{\text{DUT}}$ for the efficiency calculation.

association mechanism. Based on the residual distribution obtained from Figure 5.4b, a radial cut of $d_{\text{assoc}} = 150\,\mu\text{m}$ is applied. A uniform background from noise hits and unrelated tracks is visible in the residual distribution that cannot be separated from the relevant entries. The aforementioned cut is chosen to include most of the distribution while not taking the background into account.

5.2.4 Error discussion

Apart from the systematic uncertainty introduced by the event building procedure and discussed above, the setup, track reconstruction and analysis add multiple error sources for the efficiency calculation. In [96], four main effects are identified:

Increased $N_{\text{tracks}}^{\text{total}}$ The number of reconstructed tracks can be erroneously increased due to, for example, fake tracks produced in the track reconstruction or not assigning a valid DUT hit to the track. This will lead to an underestimation of the efficiency.

Decreased $N_{\text{tracks}}^{\text{total}}$ The efficiency of the telescope planes and the *track reconstruction efficiency* of the analysis software can reduce the total number of reconstructed tracks. The overestimation of the efficiency is, for reasonable cuts and the used telescope, less than 0.03 % [96].

Increased $N_{\text{tracks}}^{\text{DUT}}$ Assigning noise hits to a track intersection in the DUT artificially increases the efficiency. It depends on the noise occupancy in the detector as well as the association distance. This contribution is discussed in detail in Section 5.2.1.

Decreased $N_{\text{tracks}}^{\text{DUT}}$ A decrease of the measured number of DUT hits that do not correspond to an inefficiency can occur for strongly scattered tracks or those close to the sensor edges. With good track fitting methods taking scattering into account and constraining the calculation to a region of interest in the center of the sensor, this effect can be mitigated.

Exact calculations of the systematic uncertainty are difficult, since they depend, among others, on the used telescope, the efficiency of the DUT, the noise occupancy and the beam conditions such as the rate and size of the beam spot [96]. For the measurement setup and procedure as well as analysis cuts and settings used in this work, the overestimation of the efficiency is conservatively estimated to less than 0.04 %, based on the discussions in [94, 96] and the result shown in Figure 5.2. The overestimation is a bias for which an exact value cannot be determined and it will be treated as an uncertainty in the data analysis.

The probability for detection of $N_{\text{tracks}}^{\text{DUT}}$ hits in a sample size of $N_{\text{tracks}}^{\text{total}}$ where the probability corresponds to the true hit efficiency is given by the binomial distribution. The confidence intervals depend on both ϵ_{hit} and the number of recorded tracks. For ϵ_{hit} close to 1 and a typical number of recorded tracks larger than 10^6, the statistical uncertainty (1-σ interval) is less than 0.02 %. As a result, the systematic uncertainty discussed above is the dominating factor. Since it is an estimation based on the involved contributions, it is not included in the values obtained from the analysis software.

6 Hit detection efficiency of TJ-Monopix1

This chapter first recapitulates the radiation hardness results of the original TJ-Monopix1 sensor geometry (see also Section 4.1) that was studied outside this work. Within this work, the revised sensor geometry of TJ-Monopix1 that was later incorporated in TJ-Monopix2 was measured in test beam campaigns to assess the hit detection efficiency before and after irradiation.

6.1 Hit detection efficiency of original sensor design

Earlier measurements of TJ-Monopix1 showed a hit detection efficiency of 93.7 % and 97.1 %, depending on the sensor variant, for non-irradiated samples [67]. A significant efficiency loss to 50.7 % and 69.4 %, respectively, was observed after irradiation with neutrons to a NIEL fluence of $10^{15}\,\mathrm{n_{eq}\,cm^{-2}}$ [67]. Localized inefficiencies within a 2×2 pixel block were identified and tied to specific areas where large decoupling capacitors are placed. As mentioned in Section 4.1.2, those losses arise from a low electric field between adjacent pixels, where a large fraction of charges is trapped after irradiation.

6.1.1 Design changes for increased radiation hardness

Modifications to the sensor geometry were proposed based on these findings to enhance the electric field and lateral motion of charges in the detector. The proposed changes described in Section 4.1.2 were implemented in a dedicated test chip MiniMALTA demonstrating an increased hit detection efficiency after irradiation to $10^{15}\,\mathrm{n_{eq}\,cm^{-2}}$ of up to 92.5 % [97]. Additionally, an improved analog front-end in this test chip enables lower threshold values, which result in an increase of the hit detection efficiency to above 99 % after irradiation.

Due to fabrication reasons, only the change in sensor geometry could be implemented in TJ-Monopix1 which did not require a full re-submission of the design.

6.2 Hit detection efficiency with improved sensor geometry

In this work, TJ-Monopix1 chips were tested with regard to their radiation tolerance after the previously mentioned modifications of the sensor geometry. Since the analog front-end remained the same, no dedicated tests of its performance were conducted. The effects on the hit detection efficiency led to the design of TJ-Monopix2, of which the performance is evaluated in Chapter 7.

6.2.1 Investigated samples

Two different sample types were investigated. One is fabricated on a Czochralski silicon substrate with additional p-well (Figure 4.4b) and the other one on epitaxial silicon with removed n-layer at the pixel edges (Figure 4.3a). Due to availability of the samples, no comparison between the different substrates is possible in the same sensor geometry. From [69], it is expected that the latter modification (n-gap) collects slightly more charge, while the chip on Czochralski silicon offers a potentially larger depletion depth over the 30 µm epitaxial layer. The measurements investigate if the sensor modifications lead to an improved hit detection efficiency in the TJ-Monopix1 design. Samples are available before and after neutron irradiation to $10^{15}\,\mathrm{n_{eq}\,cm^{-2}}$. Irradiations were performed with neutrons from the TRIGA MARK II reactor at Jožef Stefan Institute [98].

6.2.2 Hit detection efficiency of non-irradiated TJ-Monopix1

Measurements were performed in test beam campaigns at the DESY II test beam facility [91]. The non-irradiated samples are mounted in the center of the beam telescope for the best track resolution. The noise rate is kept below 1 hit per pixel per 10^6 LHC bunch crossings which corresponds to 25×10^6 ns. Pixels exceeding the target noise rate are masked for data taking and subsequently excluded from the analysis. While this influences the efficiency of the detector as a whole, this work focuses on the performance of the pixel design for which conclusions are valid as long as the percentage of masked pixels is reasonably low ($\mathcal{O}(5\,\%)$). The matrix is laid out in design blocks of 2×2 pixels that share areas of analog and digital electronics between them. A schematic depiction of this *core cell* structure is shown in Figure 6.1. For this reason, results are presented as 2×2 histograms that contain information of the whole matrix reduced

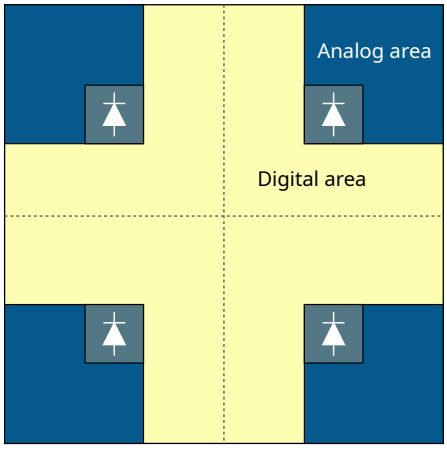

Figure 6.1: Schematic depiction of the basic building block of the matrix in the TJ-Monopix designs, referred to as core cell. It consists of a 2×2 pixel array with spatially separated analog and digital circuitry. The full matrix can be built up by tiling these blocks.

to one unit cell with high statistics. Those allow for visualization of the data with small binning to identify variations within a pixel.

A collection of plots for the non-irradiated samples is shown in Figure 6.2 and Figure 6.3. It contains hit detection efficiencies for a Czochralski silicon sample with additional deep p-well and an epitaxial silicon sample with n-gap modification, both for DC- and AC-coupled pixels. The respective results and the corresponding detection threshold Q_{thr} are given in the captions. Additionally, the efficiency in the central part of the pixels around the collection electrode is shown in the individual figures.

For the DC-coupled front-end, the hit detection efficiency is homogeneous across the 2×2 core cell and of the same value for both silicon types under investigation. Due to a higher charge detection threshold of $590\,\mathrm{e^-}$ in the AC-coupled matrix flavor of the epitaxial silicon sample, the efficiency is lower compared to the Czochralski silicon sample. There are no structures visible within the core cell of the different flavors. Across all tested samples, the obtained results show a significant increase compared to the 97.1 % hit detection efficiency reported for the original sensor design with continuous n-implant and no additional p-well [67]. Since the modifications were designed to refine the electric field shape, and the obtained results already show an improvement before irradiation, it is expected that a higher hit detection efficiency is achieved after NIEL damage as well. The use of Czochralski silicon with possibly larger depletion depth shows no advantage for non-irradiated sensors over the 30 µm thick epitaxial silicon.

6.2.3 Hit detection efficiency of irradiated TJ-Monopix1

Significant improvement of the hit detection efficiency over the one of the original sensor design is expected after NIEL damage [65]. Due to availability, only Czochralski silicon with additional deep p-well and epitaxial silicon with gap in the n-implant could be measured. The difference between the two designs can be neglected compared to the difference between modified and original sensor geometry, which allows for drawing conclusions and comparing the 300 µm thick Czochralski versus the 30 µm epitaxial silicon in terms of deposited charge. Neutron and proton irradiated samples (the latter only in Czochralski silicon with additional p-well) are mounted in a styrofoam box with circulating nitrogen for beam tests, cooling the detector down to $-20\,^{\circ}\mathrm{C}$.

Only the AC-coupled front-end type was measured due to time constraints during the test beam campaigns, since it allows for bias voltages of up to 50 V, which is expected to create a larger depletion depth than the DC-coupled one. Due to the voltage rating of the components mounted on the chip carrier board, a bias voltage of 30 V is applied to the collection electrode. However, it is expected to significantly enhance the depletion compared to the DC-coupled front-end where a maximum of $-6\,\mathrm{V}$ can be applied. Figure 6.4 shows the measured results for the hit detection efficiency of neutron irradiated sensors to a fluence of $10^{15}\,\mathrm{n_{eq}\,cm^{-2}}$.

A noticeable difference can be observed between the Czochralski silicon and the epitaxial

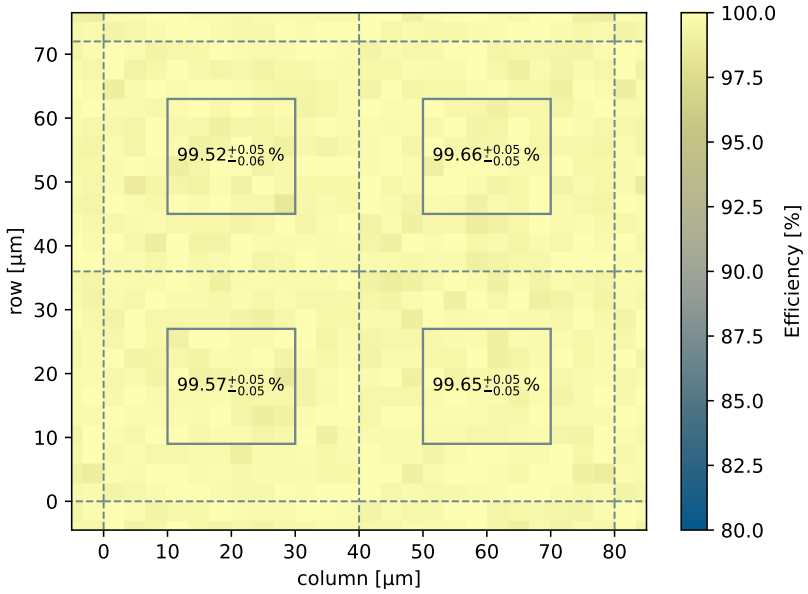

(a) DC-coupling: $\epsilon_{\text{hit}} = (99.64 \pm 0.04_{\text{sys}} \pm 0.01_{\text{stat}})\,\%$ at $Q_{\text{thr}} = 520\,\text{e}^-$.

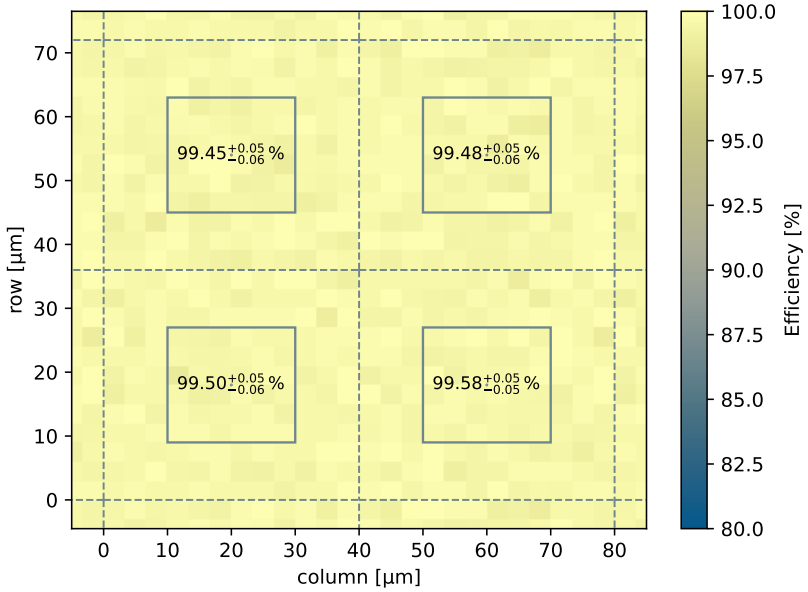

(b) DC-coupling: $\epsilon_{\text{hit}} = (99.56 \pm 0.04_{\text{sys}} \pm 0.01_{\text{stat}})\,\%$ at $Q_{\text{thr}} = 520\,\text{e}^-$.

Figure 6.2: Hit detection efficiency of the **DC-coupled** matrix flavor of **non-irradiated** TJ-Monopix1 sensors implemented on (a) 30 µm thick epitaxial and (b) 300 µm thick Czochralski silicon. Depicted are core cells consisting of 2×2 pixels each. The values of the marked areas and their statistical error corresponds to the central part around the collection electrode. Results for the whole 2×2 cell and the respective detection threshold are given in the caption.

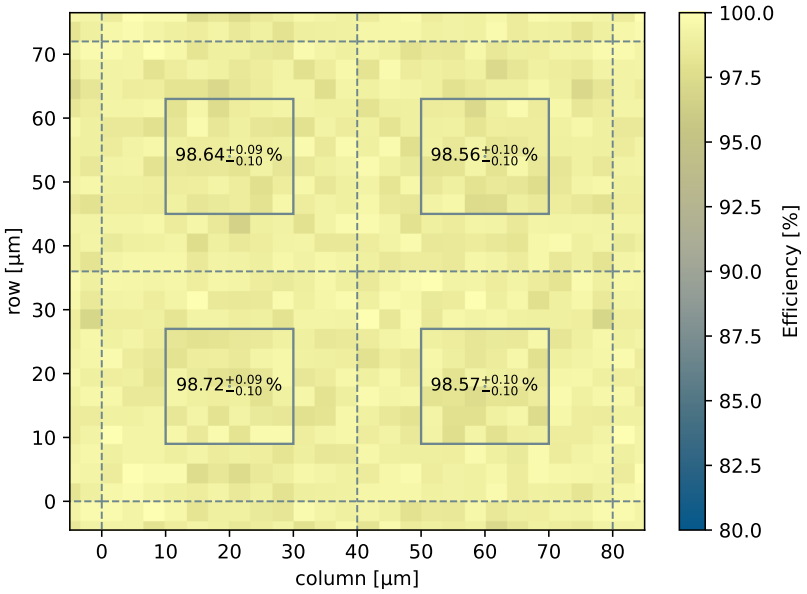

(a) AC-coupling: $\epsilon_{\text{hit}} = (98.89 \pm 0.04_{\text{sys}} \pm 0.02_{\text{stat}})\,\%$ at $Q_{\text{thr}} = 590\,\text{e}^-$.

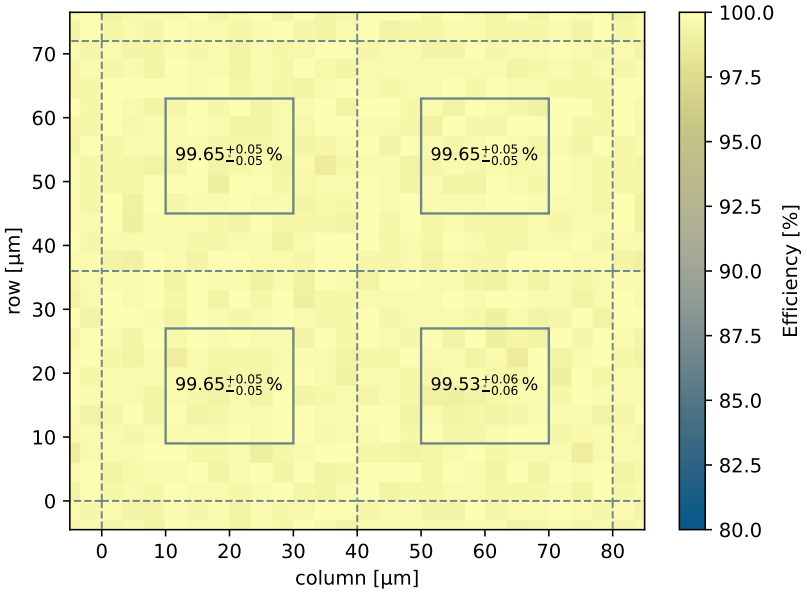

(b) AC-coupling: $\epsilon_{\text{hit}} = (99.65 \pm 0.04_{\text{sys}} \pm 0.01_{\text{stat}})\,\%$ at $Q_{\text{thr}} = 490\,\text{e}^-$.

Figure 6.3: Hit detection efficiency of the **AC-coupled** matrix flavor of **non-irradiated** TJ-Monopix1 sensors implemented on (a) 30 µm thick epitaxial and (b) 300 µm thick Czochralski silicon. Depicted are core cells consisting of 2×2 pixels each. The values of the marked areas and their statistical error corresponds to the central part around the collection electrode. Results for the whole 2×2 cell and the respective detection threshold are given in the caption.

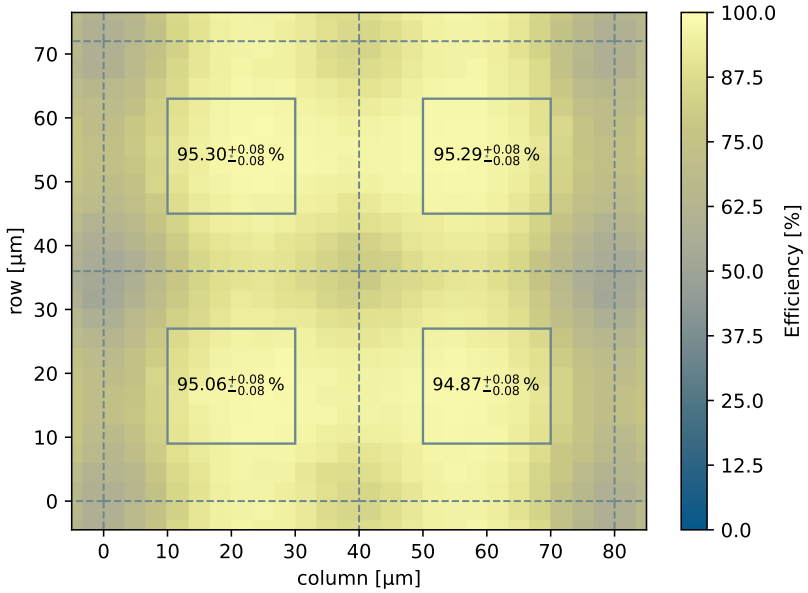

(a) AC-coupling: $\epsilon_{\text{hit}} = (87.29 \pm 0.04_{\text{sys}} \pm 0.03_{\text{stat}})\,\%$ at $Q_{\text{thr}} = 520\,\text{e}^-$.

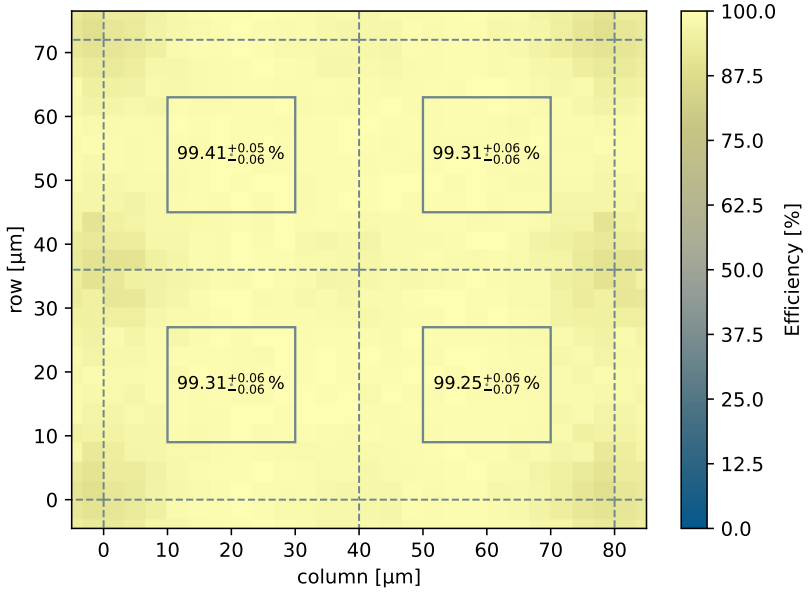

(b) AC-coupling: $\epsilon_{\text{hit}} = (98.28 \pm 0.04_{\text{sys}} \pm 0.02_{\text{stat}})\,\%$ at $Q_{\text{thr}} = 590\,\text{e}^-$.

Figure 6.4: Hit detection efficiency of the **AC-coupled** matrix flavor of **neutron irradiated** TJ-Monopix1 to a fluence of $10^{15}\,\text{n}_{\text{eq}}\,\text{cm}^{-2}$. The samples are implemented in (a) 30 µm thick epitaxial and (b) 300 µm thick Czochralski silicon. Both sensors are AC-coupled to the readout electronics and 30 V bias is applied. Depicted are core cells of 2×2 pixels each. The values of the marked areas and their statistical error corresponds to the central part around the collection electrode. Results for the whole 2×2 cell and the respective detection threshold are given in the caption. Notably, the color scale is different from the one in Figure 6.2 and Figure 6.3.

silicon sample. While the hit detection efficiency of the epitaxial sample in Figure 6.4a is 87.29 %, the Czochralski one achieves 98.28 % despite a higher threshold. The efficiency losses of the epitaxial silicon sensor occur in the pixel edges, as can be seen in Figure 6.4a, where the central part of the pixel around the electrodes still detects about 95 % of all tracks.

Since the measured front-end and biasing conditions are the same for the two samples, the relevant difference is the thickness of the high-resistivity silicon which is more than a factor of three larger in the Czochralski silicon sample. The most probable charge value is 1340 e^- and 2240 e^- in the epitaxial and Czochralski case at a detection threshold Q_{thr} of 520 e^- and 590 e^- respectively, which demonstrates a larger depleted volume in the latter. Figure 6.5 shows a map

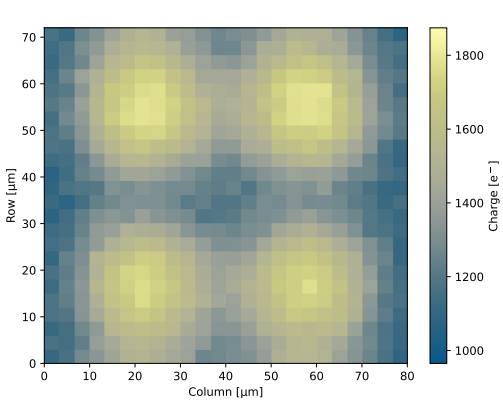

(a) Mean charge distribution over the core cell of neutron irradiated TJ-Monopix1 to $10^{15}\,\mathrm{n_{eq}\,cm^{-2}}$ for the epitaxial silicon sample. Pronounced areas of less charge are visible in the pixel corners and to some extent the pixel edges. Reasons for the ellipsoid structure are suspected to originate from the electric field shape since each pixel in the core cell is not invariant under rotations.

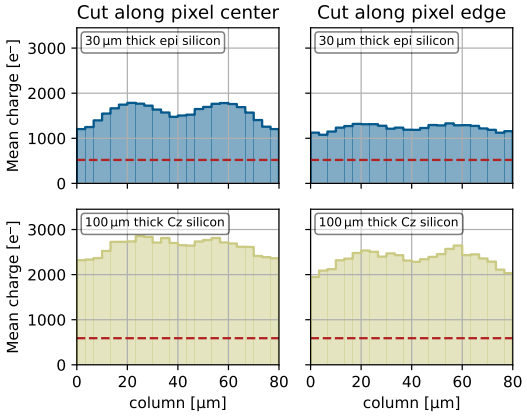

(b) Charge profile of the core cell at two different locations for $10^{15}\,\mathrm{n_{eq}\,cm^{-2}}$ neutron irradiated samples: at the center of the pixel, i.e. at row 18 in Figure (a) and at the pixel edge, i.e. at row 36. The epitaxial silicon sample is shown in blue, the Czochralski one in yellow. The respective detection threshold is marked in red.

Figure 6.5: Charge map (a) of a $10^{15}\,\mathrm{n_{eq}\,cm^{-2}}$ neutron irradiated TJ-Monopix1 on epitaxial silicon. The charge profile for two different cuts along the core cell is shown for the two irradiated samples in (b).

of the mean charge distribution in the core cell as well as the mean charge profile along the pixel center and along the pixel edge for both samples. The mean charge map in Figure 6.5a resembles the efficiency map in Figure 6.4a and originates from the same dataset. A significantly lower charge is observed at the edges and corners between the pixels where charge sharing occurs.

It can be seen from Figure 6.5b, that the ratio of collected charge to threshold is much higher in the Czochralski silicon case due to its larger thickness, compared to the epitaxial layer in the other one. In both cases, the collected charge in the epitaxial sample is slightly larger than two times the threshold. Particles impinging the detector at those locations between pixels are likely to form charge clusters of which the individual charge on each electrode must be large enough to overcome the threshold. From Figure 2.2 it is known that the mean charge is higher

than the most probable value. This means, that in the majority of cases, the deposited charge is less than the one depicted in Figure 6.5a. Charge sharing of already small signals at pixel edges and in pixel corners increases the probability of a loss of observed charges due to the threshold.

As a result, it can be concluded that the TJ-Monopix1 design can achieve high efficiency above 98 % after irradiation to $1 \times 10^{15}\,\mathrm{n_{eq}\,cm^{-2}}$, if the deposited charge is large enough to be fully read out. This can be achieved in the samples produced in Czochralski silicon where the depletion depth is not limited by the thickness of the high-resistivity epitaxial silicon. At the same time, the increase of depletable silicon can only be used if the technology allows for voltages large enough to deplete the volume. In the present case, the Czochralski silicon sample is depleted more than the epitaxial one, going by the results without performing dedicated depletion depth measurements. However, the amount of deposited charge indicates, that it is not fully depleted at 30 V bias voltage. This can be concluded from the ratio of charge to silicon thickness observed in Figure 6.5b. The achieved depletion depth, although unknown, is sufficient to reach high levels of hit detection efficiency. Alternatively, a lower threshold can be targeted, which needs a refinement of the circuitry implemented in TJ-Monopix1 as these results are obtained using the minimum achievable threshold in the test beam environment. Through dedicated design efforts, the threshold is significantly lower in TJ-Monopix2 and the hit detection efficiency results are presented in Section 7.4.3.

7 Characterization of TJ-Monopix2

The main part of this work is the characterization of TJ-Monopix2. The increased matrix size compared to TJ-Monopix1 features smaller pixels of 33.04 µm × 33.04 µm in 16.92 mm long columns. Improvements in the front-end circuitry aim for lower electronic noise, allowing for lower thresholds. Power consumption as well as threshold and noise characteristics are investigated with regard to the advantages of the small collection electrode. In addition, measurements of the depletion depth are presented. This chapter investigates the performance of TJ-Monopix2 in particle beam tests, evaluating its hit detection efficiency and timing performance.

7.1 Power consumption

As laid out in Section 4.2.4, the small detector capacitance of TJ-Monopix2 yields a large signal-to-noise ratio as well as a short signal rise time while keeping the power consumption low. The total power of the chip is spread over four power rails. Since these are supplied separately, they can be measured independently. The four power rails are:

- Power for the analog front-end,
- power for the digital-to-analog converters supplying currents and voltages for operation,
- power for the digital circuitry in the matrix, and
- power for the clock distribution, command decoder, registers and data processing in the periphery.

Figure 7.1 shows the contributions to the power consumption $P_{\text{total}} = 555.8\,\text{mW}$ of TJ-Monopix2 at its default configuration. It can be seen that the total power consumption from the DAC and the digital circuitry in the matrix is low as the currents in those domains are typically small. They are responsible for supplying currents and voltages required for operation of the front-end as well as the memory cells in the pixel and the readout logic in the column. The analog voltage supplies power to the amplifier and discriminator stage. As described in (4.5) and (4.6), the signal-to-noise ratio and the rise time improve with higher power, which is reflected by about 161 mW that is consumed by the analog front-end. It corresponds to a power consumption of less than 1 µW per pixel. The contribution of 82 mW to the power consumption of the periphery originates from the end-of-column logic such as the column-drain readout state

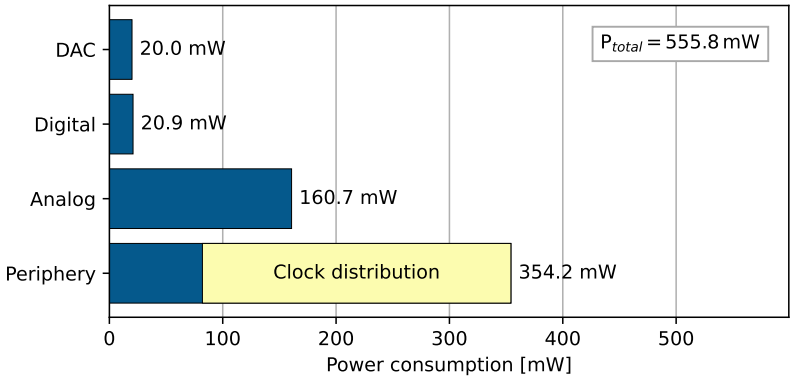

Figure 7.1: Power consumption of the different power rails of TJ-Monopix2 at default configuration settings and with all pixels enabled. The yellow bar indicates the power required for distributing the time-tagging clock through the matrix.

machine and operation of the configuration registers, data encoding and serialization, and LVDS transceivers for data transmission.

The largest contribution to the overall power consumption arises from the 40 MHz clock that is distributed throughout the matrix for recording the leading and trailing edges of the discriminator output. With the TOT method as explained in Section 4.2.2, it enables an energy measurement. The required power strongly depends on the clock frequency that is determined by the ATLAS bunch-crossing frequency, but can be reduced for other applications or even deactivated if binary hit information is sufficient. With an increasing number of columns to which the clock is distributed, the power consumption scales linearly as depicted in Figure 7.2 with 0.54 mW per column. Adding up the power required for matrix operation (analog, digital, DAC and clock distribution) yields the power consumption per matrix area, excluding the functionality in the periphery:

$$P_{\text{matrix}} = \frac{20\,\text{mW} + 20.9\,\text{mW} + 160.7\,\text{mW} + 272.2\,\text{mW}}{286.3\,\text{mm}^2} = 165.5\,\text{mW/cm}^2\,. \tag{7.1}$$

7.2 Threshold and noise performance

With its small collection electrode, TJ-Monopix2 is expected to achieve low thresholds due to a high signal-to-noise ratio. As discussed in Section 6.2.3, it is evident that a low threshold has a large impact on the hit detection efficiency. For TJ-Monopix1, a significant efficiency loss after irradiation was observed as the signal gets smaller and traps are introduced in the sensor. The effect can be reduced by utilizing a thicker sensor to increase the amount of initially created charge carriers, but a loss of signal in the pixel corners still remains. For further improvement of the charge collection and the hit detection efficiency, a decrease of the achievable minimum

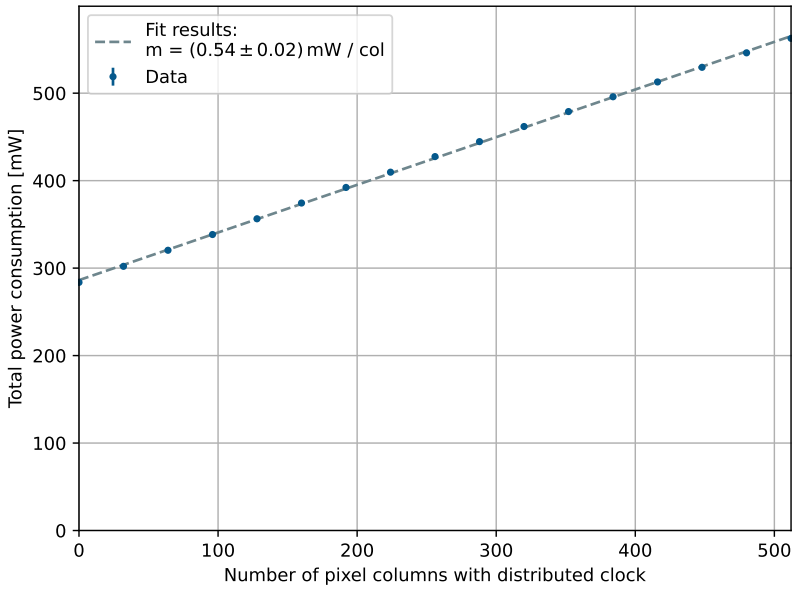

Figure 7.2: Total power consumption of TJ-Monopix2 at default settings versus the number of columns with activated matrix clock. The slope corresponds to the additional power consumption per column.

threshold is required. With a sufficiently low threshold compared to the deposited charge, the required thickness of depleted silicon can be reduced as well, aiming for a minimization of the material budget.

7.2.1 Threshold measurement using charge injection

The threshold can be determined in laboratory measurements using the charge injection capabilities of the DUT (see Section 4.2.6). At a fixed threshold setting of the discriminator, a varying charge Q is injected into the pixel. Per charge step, the injection is repeated N_{inj} times. For a range covering the threshold, a sigmoid function (s-curve) of the form

$$N_{\text{hit}}(Q) = \frac{N_{\text{inj}}}{2}\left[\text{erf}\left(\frac{Q - Q_{\text{thr}}}{\sqrt{2}\,\sigma}\right) + 1\right] \tag{7.2}$$

is observed, where σ denotes the steepness of the curve, a measure for the observed noise. Q_{thr} denotes the charge at the threshold crossing, defined as $N_{\text{hit}}(Q_{\text{thr}}) = 0.5 \cdot N_{\text{inj}}$. In the absence of noise, the curve shows a step function behavior that is smeared out in a real-world scenario. Both the ideal and the real response function are depicted in Figure 7.3.

Noise hits occur on a statistical basis and the resulting distortion of the step function is parameterized by σ, which gives the ENC. Repeating the s-curve measurement process for the full pixel matrix or a section thereof gives a threshold and noise distribution from which

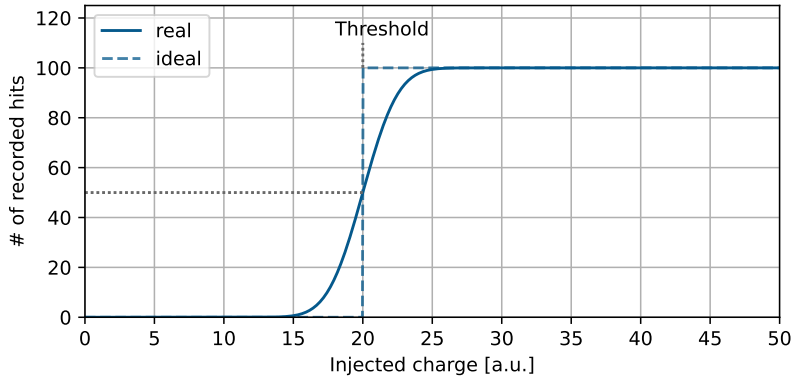

Figure 7.3: Ideal and real response of the front-end to charge injection. The threshold is defined as the charge at which the function crosses 50 % of its maximum. The smearing compared to an ideal step function can be used to determine the noise of the front-end.

important parameters can be extracted. The mean of the threshold distribution is quoted for the overall threshold value of the measured pixels and accordingly for the ENC distribution. As a measure for the uniformity of the threshold, the *threshold dispersion* is defined as the 1σ-width of the threshold distribution. It is not related to the σ used for extracting the ENC from the s-curve measurement.

Figure 7.4 shows the recorded s-curves for each pixel of a TJ-Monopix2 sample overlaid on top of each other as well as the resulting threshold distribution. The s-curves show the expected behavior with two plateaus significantly above and below the threshold where either all or no

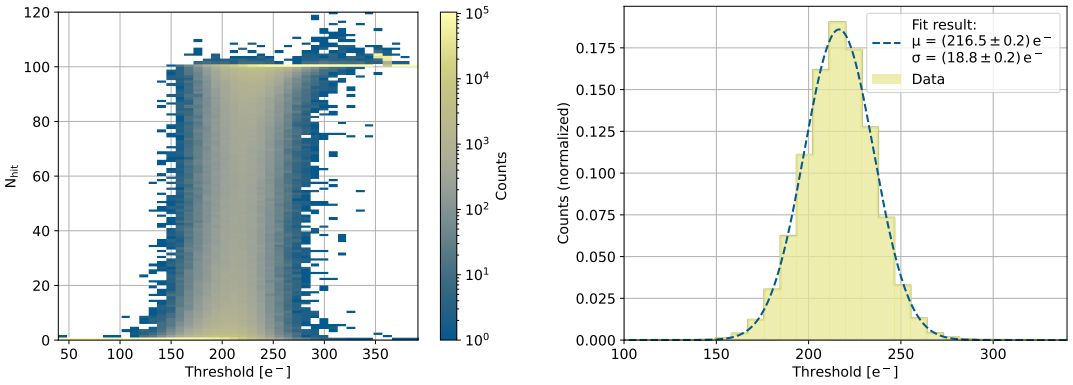

(a) S-curve measurement before local threshold trimming with $N_{\text{inj}} = 100$. Entries above 100 hits are possible due to noise hits.

(b) Threshold distribution of the data shown in (a). It follows a Gaussian function with the stated mean value and standard deviation extracted from a fit.

Figure 7.4: Exemplary s-curve threshold measurement (a) and the corresponding threshold distribution (b) before local threshold trimming. The sample is an epitaxial silicon chip with the standard DC-coupled front-end and operated with −6 V applied to the p-well and substrate.

pixels respond to charge injection. Around the threshold, the curve is broadened, which is due to threshold variations between the individual pixels. It can be attributed to localized differences in the front-end, for example the reference voltages of the DACs due to voltage drops over the matrix, and process variations. Additional hits above the upper plateau value are recorded due to noisy pixels. As long as their occurrence is small compared to the number of pixels saturating at the number of injections (100 in the given case), they can be neglected.

The threshold distribution is a cut in horizontal direction at the 50 % level of the s-curves. The width of the example distribution in Figure 7.4b, defined as threshold dispersion, is $(18.8 \pm 0.2)\,e^-$. It can be improved by trimming the threshold of each individual pixel as described in Section 7.2.3. The mean threshold value of $(216.5 \pm 0.2)\,e^-$ is measured at typical operating conditions and is not the achievable minimum. It is a factor of 1.5 smaller than the typical threshold in TJ-Monopix1 of approximately $350\,e^-$ [67]. Although a higher operational threshold is expected after NIEL due to larger noise in the sensor, the low starting point may result in a lower threshold for irradiated sensors compared to TJ-Monopix1.

7.2.2 Improvement of noise behavior

A limiting factor for the lowest achievable operational threshold in TJ-Monopix1 is a noticeable tail in the noise distribution towards higher energies [67]. Setting the threshold in this range results in a high occupancy of noise hits, resulting in potentially invalid conclusions, in particular concerning detection efficiency. The threshold has to be increased to reduce the number of noisy pixels and restore the validity of measurements. As discussed in Section 6.2.3, the outcome is a decrease in efficiency, since a significant fraction of the signal does not overcome the threshold. Section 4.2.1 gives an overview of the changes in the analog front-end implemented in TJ-Monopix2.

The noise distribution for the same data as in Figure 7.4 is displayed in Figure 7.5, overlaid with the one from TJ-Monopix1. It shows that the tail of the distribution towards higher ENC values is noticeably reduced, and the distribution is of almost Gaussian shape. The average noise value in terms of ENC is extracted from the peak positions and amounts to $6.3\,e^-$ in TJ-Monopix2, which is in line with the value of approximately $5\,e^-$ expected from the design [59]. At the same time, the average noise value is reduced by a factor of 2 compared to TJ-Monopix1.

7.2.3 Threshold tuning and threshold trimming

TJ-Monopix2 exhibits a threshold trimming feature that was not included in the previous prototype. It aims to reduce the threshold dispersion by adjusting a 3-bit trim DAC ($TDAC$) in every pixel to accommodate for small threshold variations across the matrix. A simplified schematic is shown in Figure 4.6a. The procedure to set the chip's operating conditions is called *tuning*. Depending on the type of measurement, front-end settings must be changed from their default ones to adjust to the testing environment, expected signal and other variables. The

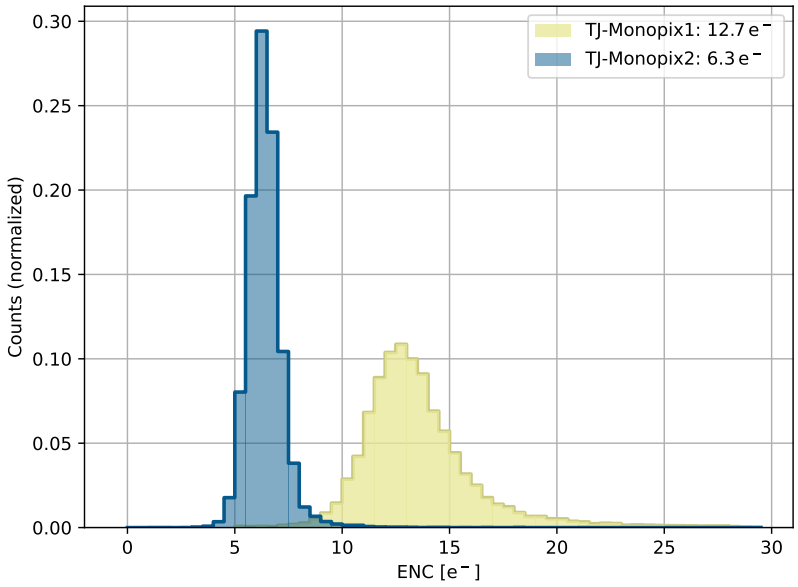

Figure 7.5: Normalized noise distribution of TJ-Monopix1 and TJ-Monopix2. A 50 % lower ENC is achieved in TJ-Monopix2 compared to TJ-Monopix1 and the pronounced tail is mitigated.

tuning of the chip to a desired threshold is typically performed in multiple steps and is an integral part of the measurement preparations. The main steps are:

1. Global (coarse) threshold tuning of the matrix as a whole with common front-end settings. Those are adjusted to match the average threshold of all pixels with the given target one.

2. Local (fine) threshold tuning of each individual pixel, adjusting the trim DAC to reduce the threshold dispersion. It aims at achieving the same target value for the threshold of each pixel.

3. (Optional) lowering of the global threshold closer to the noise floor. Due to the smaller threshold dispersion, the threshold as a whole can be lowered until the pixels with the smallest threshold reach the noise floor.

Both the settings for the global threshold and for the TDAC adjustment are computed with a binary search algorithm that features fast convergence. The tuning procedure as well as the binning of the achieved threshold distribution is limited by the least significant bit (LSB) of the injection DAC. For the local threshold tuning, the TDAC LSB can be adjusted with a front-end configuration register. Figure 7.6 shows the threshold distribution of the same sample at the same operating conditions as in Figure 7.3, but with applied local threshold tuning. The resulting threshold dispersion is reduced from 18.8 e^- to 4.6 e^-, which is at the lower end of the threshold dispersion range of 5 – 10 e^- expected from the design [59].

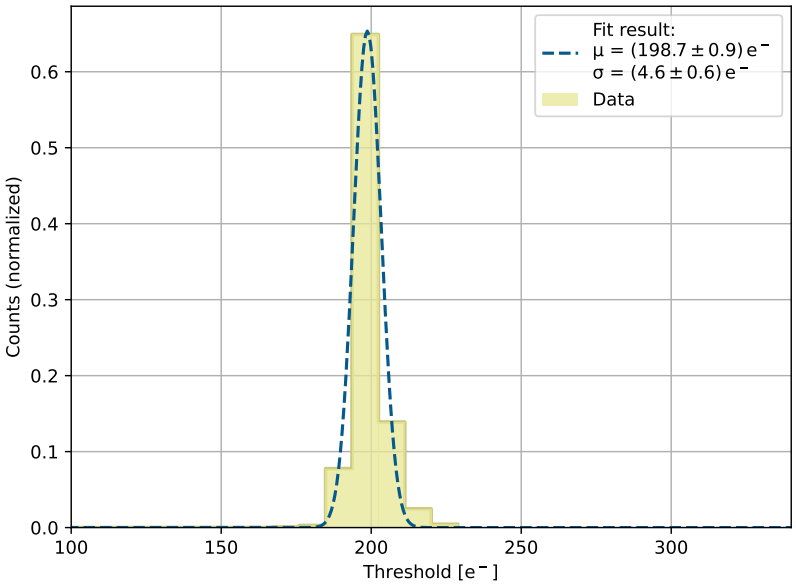

Figure 7.6: Threshold distribution for the same epitaxial silicon chip and front-end as in Figure 7.4. The in-pixel threshold DAC is adjusted to minimize the threshold dispersion across the matrix flavor in this example (approximately 100 000 pixels).

7.3 Depletion depth studies

The performance of pixel detectors depends on the volume of depleted silicon. This allows for charge collection by drift and leads to a maximum collected charge with minimum read-out time (regarding the sensor part and neglecting the electronics). According to (3.1), the depletion depth scales with the resistivity of the silicon bulk as well as the applied voltage. Both values depend on the manufacturing process and design, since the availability of silicon is determined by the foundry and the applicable voltage is limited by the chosen technology node (transistors). Additionally, the sensor design in terms of geometry and implants can pose a limit, typically by the breakdown voltage.

The collection electrode in TJ-Monopix2 is either DC- or AC-coupled, depending on the matrix flavor (see Section 4.2.5). In the former case, the electrode is directly connected with the front-end input. It is kept at the same potential as the operating voltage of the front-end of 1.8 V. Depletion is achieved by biasing both the p-well and backside of the chip, leading to depletion boundaries as depicted in Figure 4.1. Due to the sensor geometry, the applied bias voltage on the deep p-well and the p-substrate has to be kept at the same negative potential to prevent punch-through between them. The p-well also houses n-type implantations for full CMOS circuitry. For increasing voltage in the p-well, the junction with the aforementioned n-well becomes a limiting factor as the current increases and alters the operation of the circuitry. The combination of these two limitations results in an applicable voltage of up to -6 V for the

bias scheme implemented in the DC-coupled matrix flavors.

For the AC-coupled front-end, its operating voltage is supplied independently of the biasing, which opens the possibility to deplete the sensor in a more conventional way as for planar sensors. It is realized by applying a voltage between electrode and backside. This allows for a higher voltage, limited by the AC-coupling capacitor that is designed for a potential difference of up to 50 V. Due to the complex field and sensor geometry in TJ-Monopix2, expected values for the depletion depth are difficult to obtain and require precise simulations or measurements. A geometrical approach that relies on the formation of charge clusters is used to determine the depletion depth.

7.3.1 Measurement setup

The depletion depth can be probed by enlarging the distance that an impinging particle traverses. Consequently, it passes multiple electrodes in which a current is induced that will be observed as a charge cluster. Measuring the length ℓ of the cluster yields a value for the path length along which a particle produces electron-hole pairs. It is defined as the average width of a cluster in direction of the particle beam:

$$\ell = \langle cs_{\parallel} \rangle \,, \tag{7.3}$$

where $cs_{\parallel}$ is the cluster size parallel to the incident beam direction. The measurement principle and relevant values are shown in Figure 7.7. The functional relationship between the measured

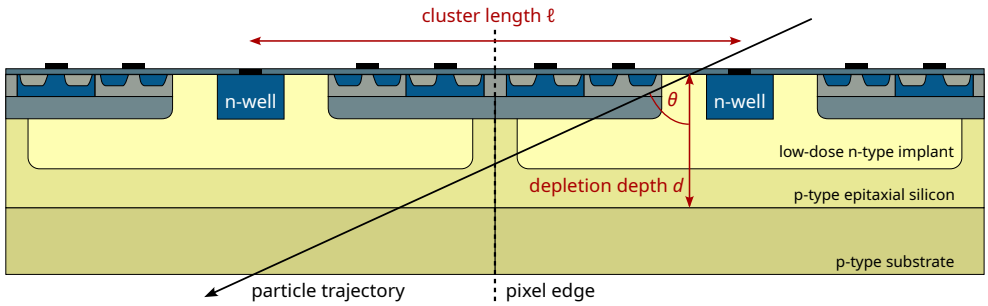

Figure 7.7: Measurement principle for determination of the depletion depth from charge clusters. A particle track with incidence angle θ traverses multiple pixels and creates a signal in each of them. The number of hit pixels in the same plane as the particle track is defined as the cluster length.

angle θ and the cluster length ℓ is:

$$\ell\left(\tan\left(\theta\right)\right) = d\,[\text{pitch}] \cdot \tan\left(\theta\right) + \ell_0 \,. \tag{7.4}$$

In this equation, the depletion depth d is given in units of the pixel pitch and ℓ_0 is the cluster length at an incident angle of 0°. The depletion depth d can be determined by a linear fit when

ℓ is plotted against $\tan(\theta)$.

7.3.2 Determination of the depletion depth

In a beam test campaign, the DUT is rotated along the horizontal axis orthogonal to the beam. Figure 7.8 shows the corresponding data and results for a sensor with 30 µm epitaxially grown silicon in (a) and 100 µm thick Czochralski silicon in (b). Both samples have the n-gap sensor geometry and are not irradiated. As expected, the average cluster length increases with the

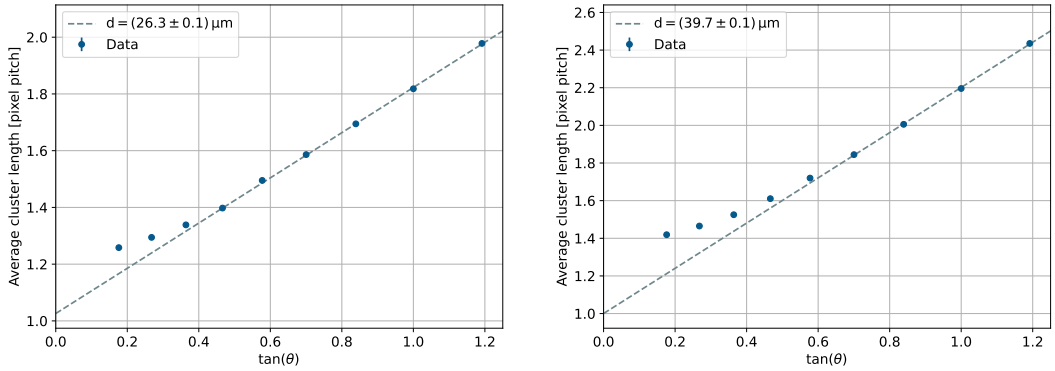

(a) 30 µm thick epitaxial silicon with n-gap modification, standard front-end.

(b) 100 µm Czochralski silicon with n-gap modification, standard front-end.

Figure 7.8: Average cluster length versus the DUT angle with respect to the beam. In the non-linear part, diffusion has a significant contribution to charge collection. From the linear part, the depletion depth is determined from a line fit. Uncertainties on the angle are not depicted due to the precision of the rotation stage ($< 0.1^\circ$). Error bars are too small to be visible.

incident angle, and follows a linear shape above 30° or $\tan(30^\circ) = 0.58$. The change in shape is related to the geometrical accuracy of the measurement. It can be seen in Figure 7.7 that the cluster length is an imprecise measure for small incident angles as it depends more strongly on the hit position in the pixel than the traversed number of pixels. Due to the thicker sensitive material, the Czochralski sample already shows a higher average cluster size for small rotation angles θ. By a linear fit to the data points in the aforementioned range, the depletion depth of the epitaxial and the Czochralski silicon sample are extracted:

$$d_{\text{epi}}|_{-6\,\text{V}} = (26.3 \pm 2.0_{\text{sys}} \pm 0.1_{\text{stat}})\,\mu\text{m}\,, \tag{7.5}$$

$$d_{\text{Cz}}|_{-6\,\text{V}} = (39.7 \pm 2.0_{\text{sys}} \pm 0.1_{\text{stat}})\,\mu\text{m}\,. \tag{7.6}$$

The large systematic uncertainty is an estimation based on the obtained results for different choices on where the linear range begins.

In the sensor with epitaxial silicon, the achievable depletion depth d_{epi} is limited by the thickness of the high-resistivity epitaxial layer that is given by the foundry as 30 µm. Taking

variations of the thickness and the volume occupied by electronics into account, the result of 26.3 µm is within the expected range. A comparable value of $(25.8 \pm 2.0_{\text{sys}} \pm 0.1_{\text{stat}})$ is obtained for the AC-coupled front-end biased with a large voltage of 35 V. This proves that the depletion depth is in fact limited by the thickness of the epitaxial layer and both DC- and AC-coupled front-end flavors can be fully depleted.

On the other hand, the Czochralski silicon has a highly resistive silicon bulk of 100 µm thickness. The depletion depth d_{Cz} given above shows a significantly deeper depletion of this sensor design with the applied −6 V compared to the epitaxial one. Based on these findings, the collected charge is expected to be higher than in the 30 µm epitaxial silicon case, although not the full thickness of the substrate can be depleted. This observation is also in line with the results presented for TJ-Monopix1 in Section 6.2.3 and Figure 6.5b, which exhibits a sensor geometry that is very close to the one in TJ-Monopix2. As displayed in Figure 6.1, the individual pixels are not symmetric under rotation and consequently the pixel response can vary over an elongated cluster. Non-uniform electrical fields in the sensor constitute another contribution to the systematic uncertainty, that – in total – tends to underestimate the cluster length.

7.4 Beam tests of non-irradiated sensors

Multiple test beam campaigns were conducted at the DESY II test beam facility [91] with a 5 GeV electron beam to study the performance of TJ-Monopix2 concerning its charge collection properties, spatial resolution and hit detection efficiency. The setup is identical to the one sketched in Figure 5.1 and used in Chapter 6.2. In none of the tested chips, the rightmost front-end (AC-coupled standard front-end) was fully functional, but half of the columns did not respond to any input signal. Due to the low number of operational pixels and the available beam time, this front-end variation was not measured.

7.4.1 Charge deposition

For tracking detectors, the deposited charge in the sensor must be large enough to overcome the threshold to provide a good hit detection efficiency. According to (2.7), the amount of charge created in the sensor is subject to fluctuations in both number and energy transfer. The resulting charge distribution follows a distinct shape from which the most probable value (MPV) can be extracted. It strongly depends on the size of the depleted volume and the electric field configuration. The histogram of the collected charge in an epitaxial and Czochralski silicon sample with a 30 µm and a 100 µm thick sensitive layer, respectively, is shown in Figure 7.9. The relevant threshold settings are indicated in the figure. For both silicon variants, the most probable value exceeds the threshold (240 e^-) by more than a factor of 9. As expected, the thicker sensitive volume in the Czochralski silicon sample allows for a larger signal since more charge is collected by drift in the depleted region. Measurements of the achieved depletion are

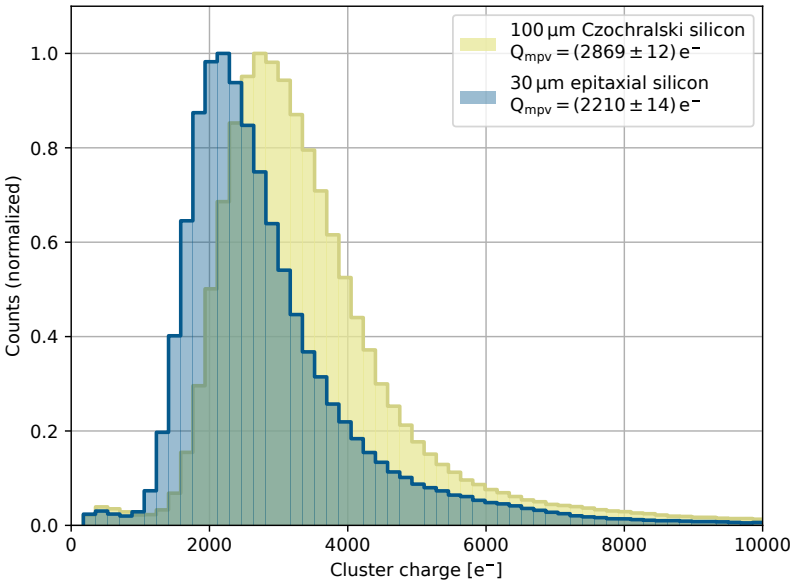

Figure 7.9: Charge distribution for the standard DC-coupled front-end in 30 µm thick epitaxial (blue) and 100 µm thick Czochralski silicon (yellow).

presented in Section 7.3. The collected charge is of the expected order of magnitude, assuming a charge deposition of about 70 e^- per µm according to [3, 99].

7.4.2 Cluster size and spatial resolution

As a consequence of the small pixel size, geometrical considerations lead to the expectation that a significant amount of deposited charge induces a signal in the electrodes of neighboring pixels (see Section 2.2.3). The observed number of pixels in a charge cluster depends on the inter-pixel incidence position of the charge-depositing particle. Hits close to the pixel edge or corner can share the charge between one or more adjacent electrodes. Cutting the signal of each individual pixel due to the applied threshold can lead to underestimation of the cluster size if the individual charge is smaller than the threshold. This is more likely to occur in case of a small initially deposited charge or a large extent of the cluster. As described in Section 5.2.2, clusters can improve the spatial resolution of a detector, especially in combination with energy information of the individual hits.

The cluster size depends on the size of the charge cloud that arises from diffusion. Its broadening is not related to drift, but the movement in the drift field that induces the signal at the electrodes restricts the time over which the diffusion can take place. Hence, the cluster size depends on the thickness of the sensitive layer. Figure 7.10 shows the obtained cluster size distribution for different thicknesses. The average cluster size for the Czochralski silicon sample

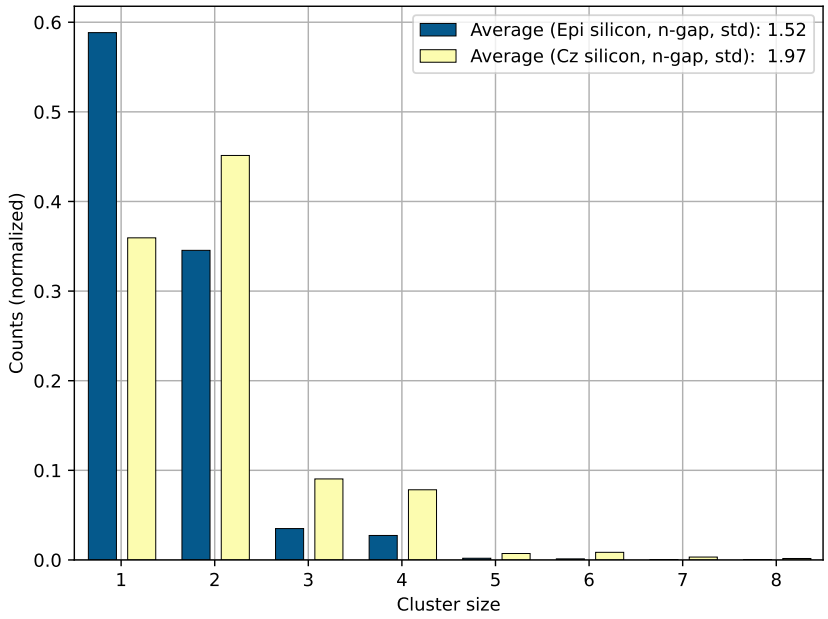

Figure 7.10: Cluster size distribution for the standard DC-coupled front-end of chips with 30 µm epitaxial silicon and 100 µm Czochralski silicon with n-gap modification. According to the results in Section 7.3, the depletion depths are 26.3 µm and 39.7 µm, respectively.

is about 30 % larger with most clusters of size 2 compared to the epitaxial silicon sample with predominantly cluster size 1.

In order to calculate the achieved spatial resolution for different samples, the contribution from the track resolution σ_{tel} to the total measured one has to be determined. When restricting the calculation to hits that do not produce charge clusters, the spatial resolution is given in (5.8):

$$\sigma_{\text{det}} = \frac{p}{\sqrt{12}} \,, \tag{7.7}$$

where p is the pixel pitch. According to (5.10), the track resolution can be calculated if the detector resolution is known. Measuring the spatial resolution from events with only one hit and combining (5.10) and (7.7) yields:

$$\sigma_{\text{tel}}^2 = \sigma_{\text{res}}^2 - \sigma_{\text{det,1-hit}}^2 = \sigma_{\text{res}}^2 - \frac{p^2}{12} \,. \tag{7.8}$$

From the measurement data, a resolution of $\sigma_{\text{tel}} = (3.67 \pm 1.50)$ µm is derived. It is in agreement with the results obtained from studies of the used telescope [87]. The track resolution is used to calculate the actual detector resolution σ_{det}.

The resulting values as well as the average cluster size for different samples and front-end flavors is shown in Figure 7.11. In general, the spatial resolution correlates with the cluster size

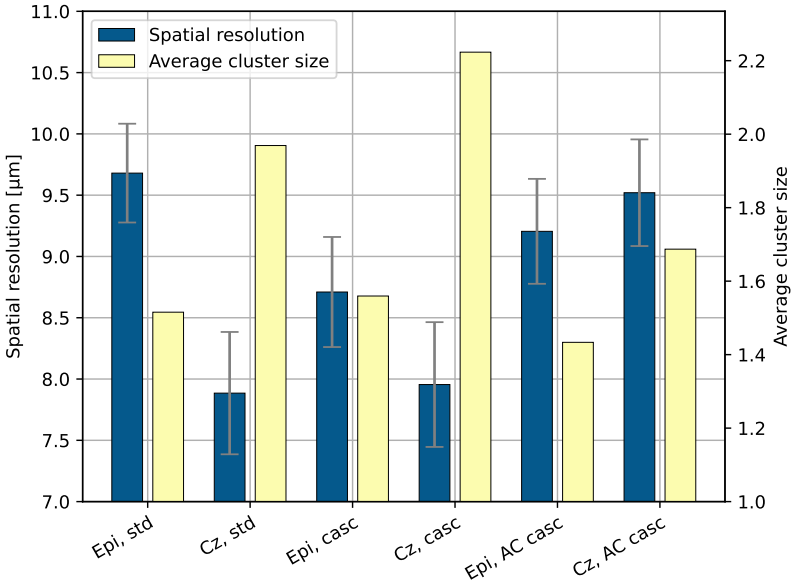

Figure 7.11: Spatial resolution and average cluster size for all tested samples across different thicknesses of the charge-sensitive layer and front-end flavors. The track resolution of $(3.67 \pm 1.50)\,\mu\text{m}$ has been subtracted for all given values. The uncertainty on the average cluster size is consistently below 0.01 and not shown.

with better resolution achieved in samples with a large average cluster size, as expected from Section 5.2.2. The Czochralski silicon samples generally show a better spatial resolution than the epitaxial silicon ones, which matches the results presented in Figure 7.10. Deviations can arise from threshold effects. The uncertainty of the spatial resolution is dominated by the one of the track resolution. It should be noted that the absolute variations of the spatial resolution are below 2 µm for all tested samples.

7.4.3 Hit detection efficiency

With the available tracking data, the hit detection efficiency of TJ-Monopix2 is measured as described in Section 5.2.3. All results are obtained from data with 5 GeV electrons at the DESY II test beam facility [91]. Multiple non-irradiated samples are tested with respect to the thickness of the sensitive layer and across multiple matrix flavors. A schematic drawing of the matrix and its front-end implementations is shown in Figure 4.10. As mentioned in Section 7.4, the DC-coupled front-ends with and without additional cascode transistor and the AC-coupled front-end with cascode transistor are investigated. The efficiency maps for a 2×2 core cell are displayed in Figure 7.12, Figure 7.13 and Figure 7.14. For the Czochralski silicon samples, the high-resistivity silicon has a thickness of 100 µm, for the epitaxial silicon samples 30 µm.

The hit detection efficiency for the DC-coupled front-end flavors (Figure 7.12 and Figure 7.13)

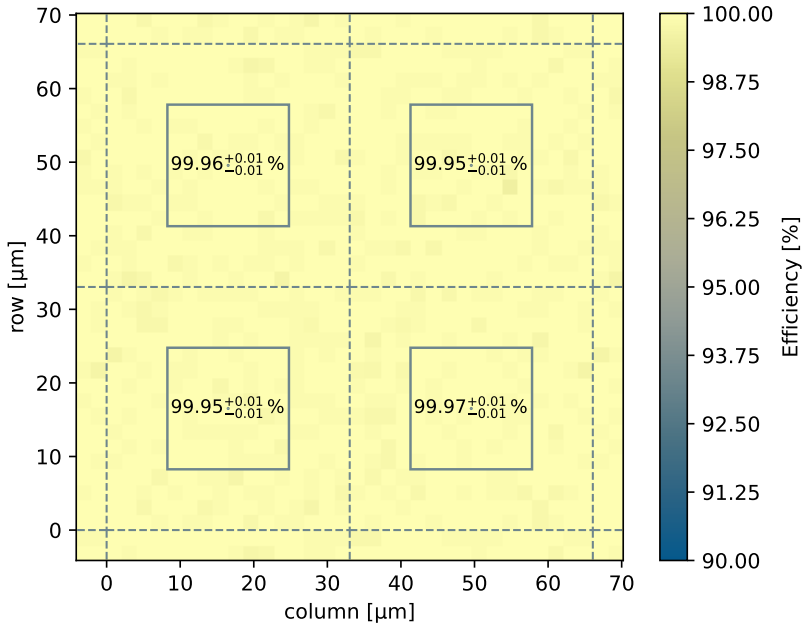

(a) $\epsilon_{\text{hit}} = (99.96 \pm 0.04_{\text{sys}} \pm 0.01_{\text{stat}})\,\%$ at $Q_{\text{thr}} = 240\,\text{e}^-$.

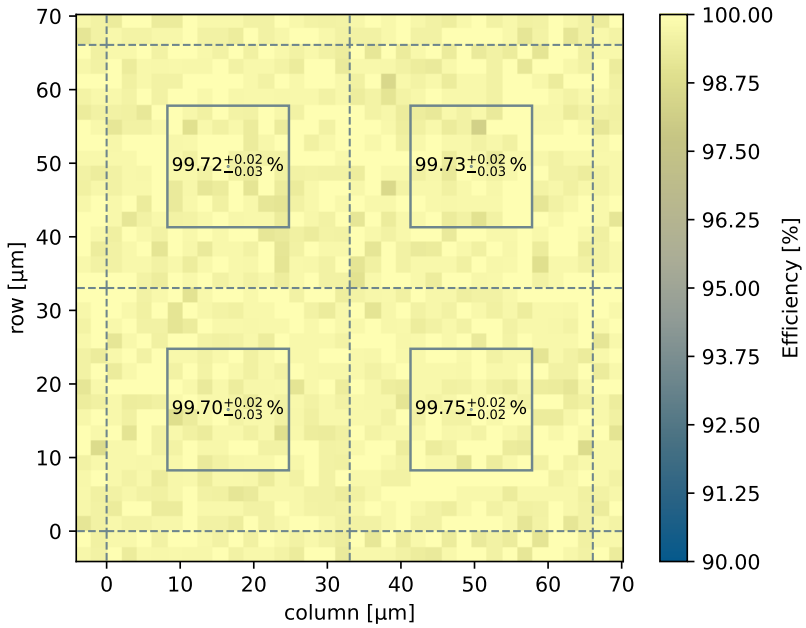

(b) $\epsilon_{\text{hit}} = (99.73 \pm 0.04_{\text{sys}} \pm 0.01_{\text{stat}})\,\%$ at $Q_{\text{thr}} = 235\,\text{e}^-$.

Figure 7.12: Hit detection efficiency of the **DC-coupled standard** front-end on (a) epitaxial silicon and (b) on Czochralski silicon. Displayed is the core cell consisting of 2×2 pixels. The values of the marked areas and their statistical error correspond to the central part around the collection electrode. The samples are operated with $-6\,\text{V}$ applied to the substrate and p-well.

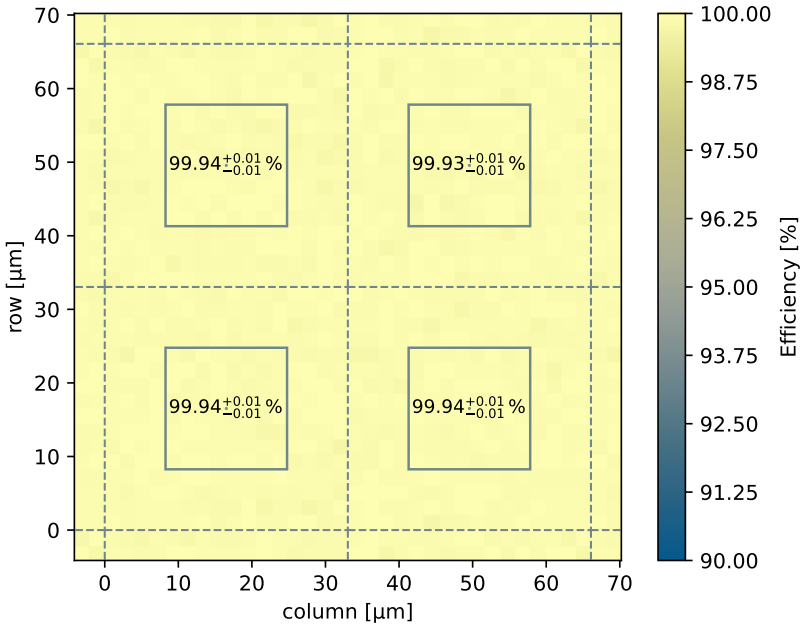

(a) $\epsilon_{\text{hit}} = (99.94 \pm 0.04_{\text{sys}} \pm 0.01_{\text{stat}})\,\%$ at $Q_{\text{thr}} = 205\,\text{e}^-$.

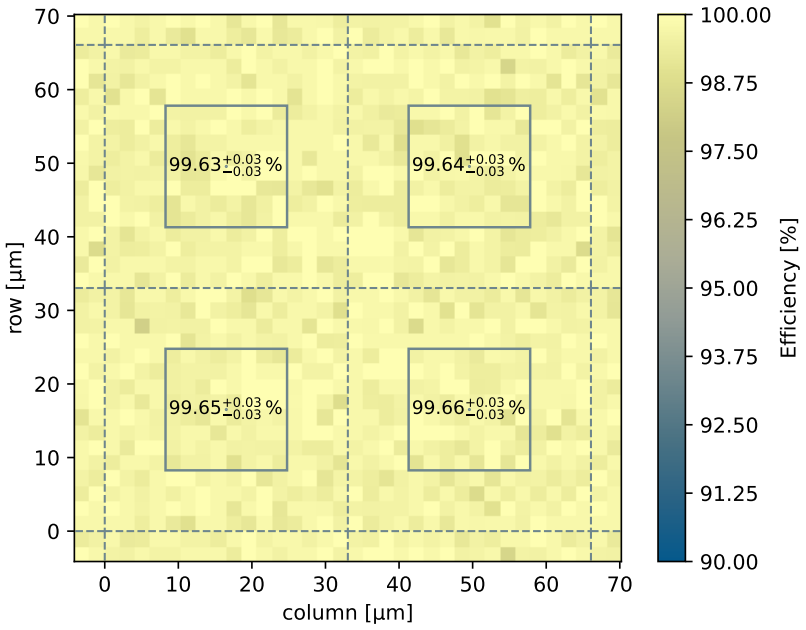

(b) $\epsilon_{\text{hit}} = (99.65 \pm 0.04_{\text{sys}} \pm 0.01_{\text{stat}})\,\%$ at $Q_{\text{thr}} = 210\,\text{e}^-$.

Figure 7.13: Hit detection efficiency of the **DC-coupled cascode** front-end on (a) epitaxial silicon and (b) on Czochralski silicon. Displayed is the core cell consisting of 2×2 pixels. The values of the marked areas and their statistical error correspond to the central part around the collection electrode. The samples are operated with $-6\,\text{V}$ applied to the substrate and p-well.

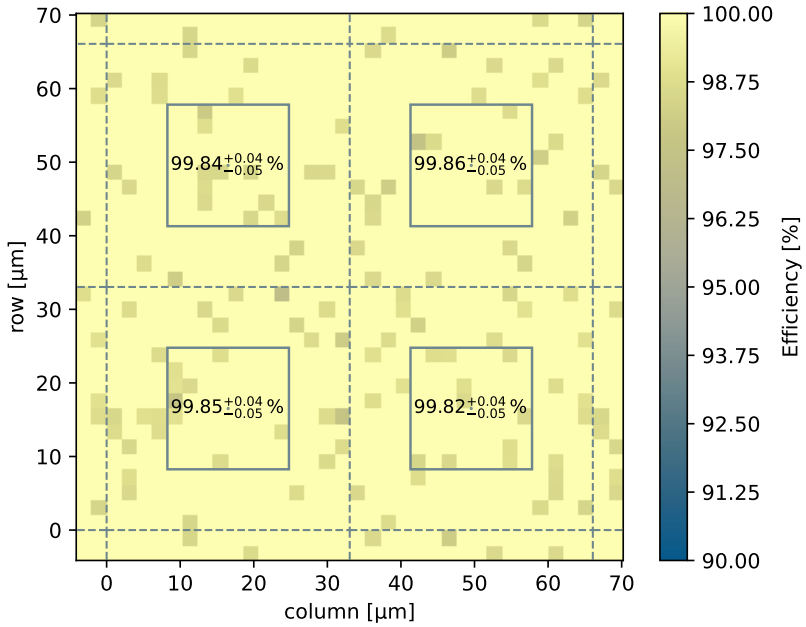

(a) $\epsilon_{\text{hit}} = (99.85 \pm 0.04_{\text{sys}} \pm 0.02_{\text{stat}})\,\%$ at $Q_{\text{thr}} = 225\,\text{e}^-$.

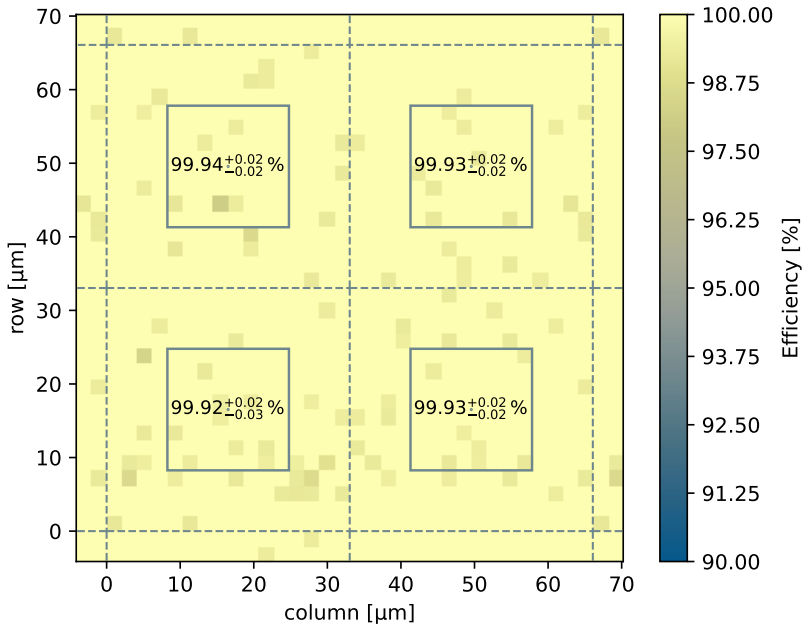

(b) $\epsilon_{\text{hit}} = (99.93 \pm 0.04_{\text{sys}} \pm 0.01_{\text{stat}})\,\%$ at $Q_{\text{thr}} = 240\,\text{e}^-$.

Figure 7.14: Hit detection efficiency of the **AC-coupled cascode** front-end operated at 15 V bias voltage on (a) epitaxial and (b) on Czochralski silicon. Displayed is the core cell consisting of 2×2 pixels. The values of the marked areas and their statistical error correspond to the central part around the collection electrode. The pronounced bins on the given color scale arise due to fewer statistics.

is homogeneous across the core cell and larger than 99.6 % for all tested samples. No significant differences can be observed between the DC-coupled front-ends for each sample. The ones with epitaxial silicon as the sensitive layer achieve values above 99.9 % at a threshold of 240 e^-. For those implemented in Czochralski silicon, the efficiency is approximately 0.2 – 0.3 % smaller. This small difference cannot be explained with the significant difference in depletion depth, as measured in Section 7.3 and a larger most probable charge (Section 7.4.1). Since the threshold value in those measurements is very similar and no losses within the pixel can be observed, no apparent reason has been identified at this time. Precise simulations to model the electrical field and charge deposition, propagation and collection could be used in the future to examine the observed results.

For the AC-coupled pixel flavors (Figure 7.14), the hit detection efficiency is above 99.8 %. The Czochralski silicon samples show an efficiency of 99.93 %. In contrast to the DC-coupled pixels where the Czochralski samples show a slightly lower hit detection efficiency, the result for the AC-coupled pixels matches the expectation based on the larger depletion depth. A possible explanation is the different biasing procedure in the AC-coupling case (with positive voltage on the collection n-well and the substrate connected to ground) and subsequently a different field geometry.

In summary, all pixel flavors across different samples detect hits with a probability larger than 99.6 %, some exceeding 99.9 %, and can be considered fully efficient.

7.5 Timing studies

To study the suitability of a detector for a high-energy physics experiment, not only the ionization effects and ultimately the hit detection efficiency have to be taken into account, but the time requirements have to be met as well. Typically, the time interval between collisions is fixed and all hits in such an interval have to be read out before the next one. Both the time resolution and the in-time efficiency, i.e., the percentage of hits being recorded within this time interval, are investigated in this work.

Measurements are conducted using a feature of the FPGA firmware (see Section 4.4.2), where both the length of the `HitOr` signal and the delay with respect to a reference signal is sampled with a 640 MHz clock. This results in a 1.5625 ns time measurement resolution. A network of OR gates in the matrix propagates the `HitOr` signal along the column to the periphery, and each one has a processing time in the order of picoseconds that needs to be corrected for due to the high number of rows in a column. In the chip bottom, the signals are again combined with logical OR gates to merge the individual column signals down to one digital line. It is directly connected to the DAQ system, which means that only the signal of one pixel can be read out at a time.

7.5.1 Time walk measurements using charge injection

By using the charge injection capabilities of the chip (see Section 4.2.6), a large sample size on a per-pixel basis with controllable amplitude can be achieved in the lab. Since no charge is deposited in the sensor volume, the result is not dependent on the thickness or type of silicon, and takes only the front-end electronics into account. From these measurements, the time walk and noise components in (4.2) can be determined.

For the reference time, a signal from the command encoder is chosen that produces a pulse every time an injection command is processed and sent to the chip. The setup is sketched in Figure 7.15. The `HitOr` propagation delay and the charge injection delay both depend on the position of the pixel in the matrix.

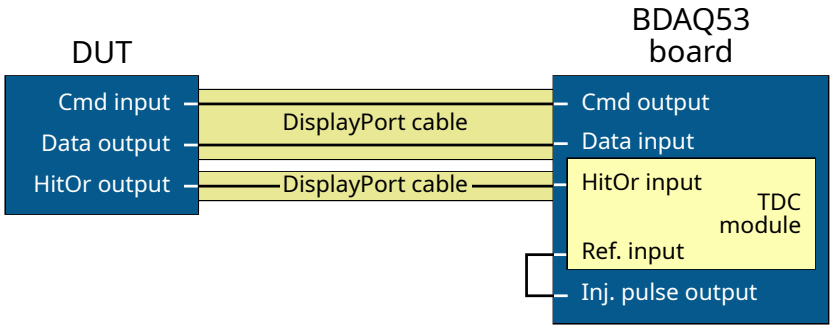

Figure 7.15: Setup for time walk measurements using the charge injection circuitry of TJ-Monopix2. A pulse from the command encoder that is in a high state every time an injection command is sent to the chip is used as time reference. It is available on a LEMO output connector of the DAQ board and fed back into a LEMO input connector with a short cable.

As such, these effects cannot be differentiated. The typical order of magnitude of 50 – 100 ns is significantly larger than the value to be measured ($\mathcal{O}(1\,\text{ns})$). Thus, it cannot be determined when injecting into multiple pixels at the same time. The following results are for one pixel in the center of the matrix flavor under test only, if not stated otherwise. For fine binning of the measured charge, the length of the `HitOr` pulse is sampled with 1.5625 ns precision and the amount of charge is given in nanoseconds. The resulting distribution of trigger delay versus charge for a single pixel is shown in Figure 7.16. The large number of data points at low charges (compared to Figure 7.21) arises from the fact that the charge distribution from injection does not follow an energy loss behavior as the deposition of charges in the sensor. Due to the limited amount of charge that can be injected, the curve does not show saturation towards high charges. In order to estimate the minimum trigger delay, the curve is extrapolated. The extrapolation is shown in Figure 7.16. The in-time threshold is determined from the crossing point of the time walk curve and the highlighted window, which corresponds to a trigger delay of 25 ns with regard to the extrapolated saturation value. It corresponds to 306 e^- at a nominal threshold setting of 240 e^-. By subtracting these values from each other, a threshold overdrive (see Section 4.2.3) of 66 e^- is measured in good agreement with the simulated values of 65 e^- [59]. The spread of the

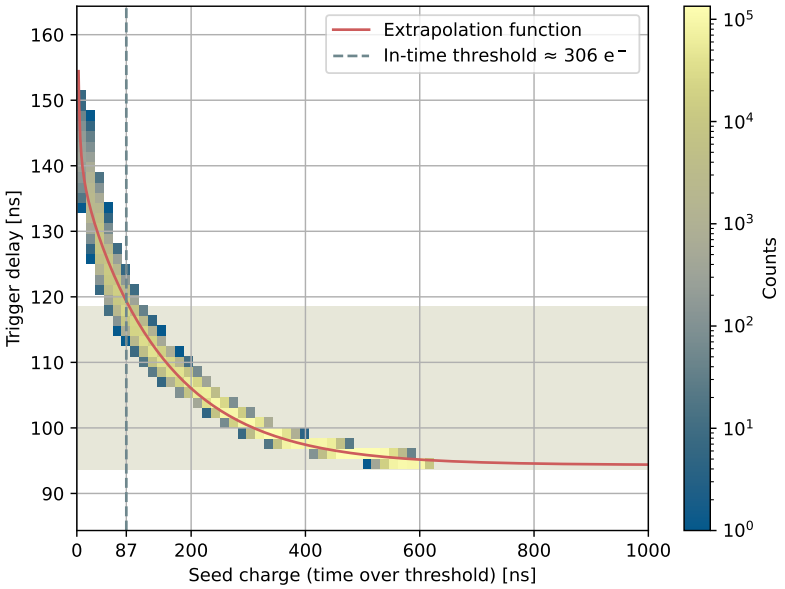

Figure 7.16: Time walk curve for one pixel with extrapolation to the saturation region. In the plot, the saturation value is subtracted from the data to define the in-time window of 25 ns for arrival time of hits. The in-time threshold is estimated to 87 ns, which corresponds to 306 e^- at a nominal threshold of 240 e^-, i.e. 66 e^- threshold overdrive.

in-time threshold will increase compared to the nominal threshold due to rise-time and noise differences across multiple pixels. With a typical threshold dispersion of less than 10 e^-, the dispersion of the in-time threshold is expected to be in the same order of magnitude.

It can be noted from Figure 7.16 that the trigger delay measurement points are spread across a few bins of 1.5625 ns width in vertical direction. A more precise measurement is not possible with the given firmware framework, but a digital oscilloscope[1] offers better time resolution with an uncertainty less than 10 ps. The measurements above are thus repeated with an oscilloscope. Figure 7.17 shows the injection pulse and `HitOr` signal from a single acquisition. The time walk is the delay between the rising edges of the two signals and the pulse length measurement of the `HitOr` corresponds to the injected charge. To speed up data taking, fourteen charge values are used over the whole injection circuit range. A fixed amount of charge is injected repeatedly to get about 10 000 entries for each data point. Figure 7.17b shows the resulting curve on top of the ones measured with the TDC FPGA module. The two measurements are well in agreement and validate the oscilloscope measurement setup.

[1] `https://www.tek.com/en/datasheet/5-series-mso`

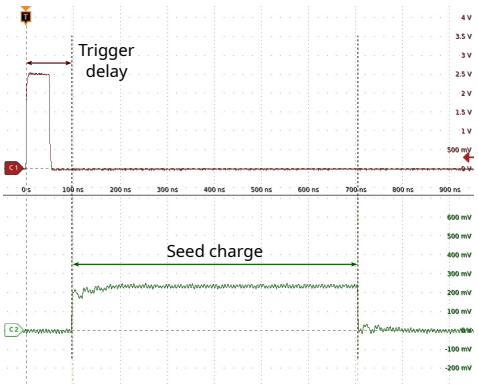

(a) Oscilloscope screen for the time walk measurement using charge injection. Depicted is a single sample. The top channel is the injection pulse signal from the command encoder, the bottom channel the `HitOr` output of the DUT.

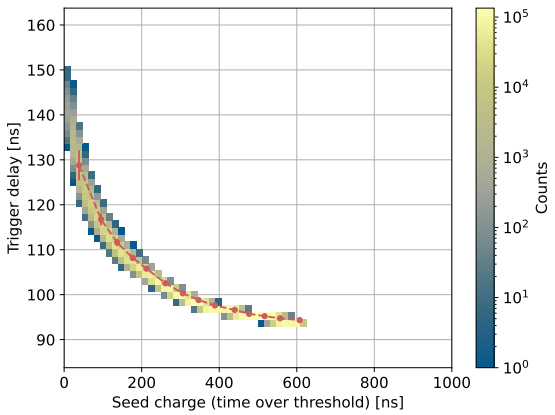

(b) Time walk measurement with an oscilloscope (red) overlaid on top of the measurement using the TDC module in firmware. The two are well in accordance with each other.

Figure 7.17: Oscilloscope measurement of time walk with the injection circuit of TJ-Monopix2. The time resolution of the oscilloscope far outweighs the one from the TDC FPGA module. The overlay of the oscilloscope measurement (in red) in (b) demonstrates the validity of the measurement, producing the same results.

7.5.2 Time resolution of the analog front-end

Due to the time resolution of this setup, it can be used to measure the time stability of the rising edge of the discriminator. The noise contribution in (4.2) depends on the signal rise time and the (electronic) noise on the signal [73]:

$$\sigma_{\text{noise}} = \frac{N}{\mathrm{d}V/\mathrm{d}t} \approx \frac{t_r}{S/N} \,, \tag{7.9}$$

with $\mathrm{d}V/\mathrm{d}t$ the slope of the rising edge at the threshold and t_r the rise time of the signal (assuming a linear slope). N denotes the noise and S the signal with S/N being the signal-to-noise ratio. The signal in a small-collection-electrode design is typically large because of the small capacitance, while the noise is small, resulting in a short rise time and a high signal-to-noise ratio. Again, the setup with a digital oscilloscope with integrated delay measurements between two input channels as in Figure 7.17a is used. The time distribution of the leading edge with respect to the reference pulse at the largest injection charge ($140\,\Delta\mathrm{V_{cal}}$) is depicted in Figure 7.18.

For the charge equivalent of $140\,\Delta\mathrm{V_{cal}}$ (approximately $1200\,\mathrm{e^-}$), the rise time is in the order of 20 ns [59], and the signal-to-noise ratio is approximately 200 for the front-end settings used in these measurements. A rough calculation of the expected time resolution is according to (7.9) 87 ps. Fitting a Gaussian function yields a time resolution of 93.7 ps. Subtracting

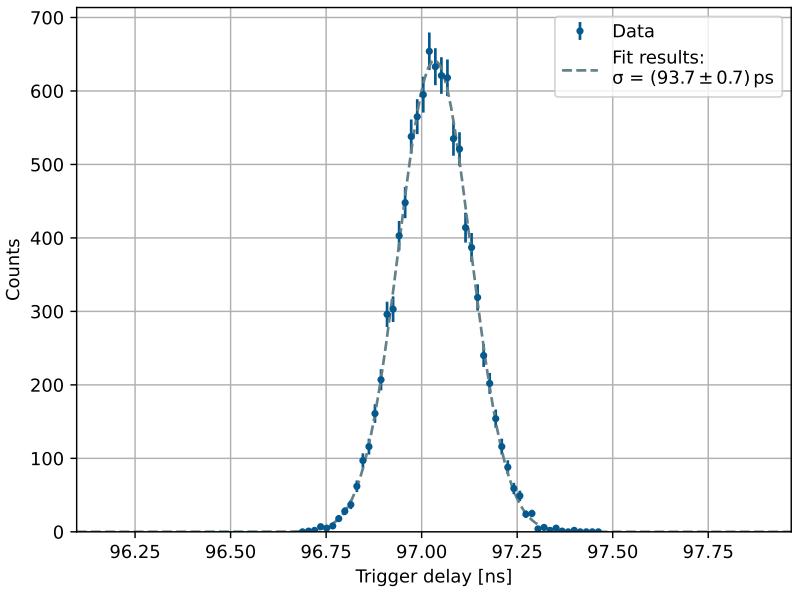

Figure 7.18: Leading-edge distribution for the largest available injection charge. The uncertainty of the trigger delay is in the single digit picosecond range and not displayed.

the 8.6 ps time resolution of the oscilloscope in quadrature results in

$$\sigma_{\text{noise}} = \sqrt{\sigma^2_{\text{meas}} - \sigma^2_{\text{osc}}} = (93.3 \pm 0.8)\,\text{ps}\,, \tag{7.10}$$

which is in the expected order of magnitude. Figure 7.19 shows the width of the leading edge distribution for various injection charges. It can be concluded that the jitter is less than 500 ps for charges larger than 200 ns, which corresponds to about 300 – 400 e^- depending on the operating conditions, but well below the typical cluster charge (larger than 2000 e^-) reported in Section 7.4.1. The observed saturation of the jitter leads to the expectation that it will not improve significantly for higher charges, although the charge regime of interest is not covered by the measurement.

7.5.3 Timing studies with minimum-ionizing particles

In a beam test campaign at the DESY test beam facility [91], the time walk for TJ-Monopix2 is measured with a non-irradiated chip on epitaxial silicon. From the results, the percentage of hits that arrive within 25 ns can be determined. No beam telescope is necessary for this measurement, but a reference time signal from a scintillator is used together with a EUDET-type trigger logic unit as explained in Section 5.1. The TLU provides the discriminated scintillator signal as LEMO output, which is connected to the readout board as well as the `HitOr` signal from the DUT. The cable lengths introduce a constant difference between the reference and

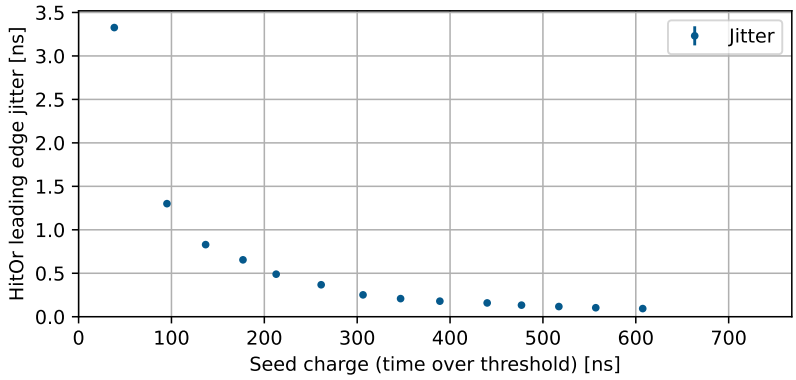

Figure 7.19: Width of the leading edge distribution versus injected charge. For sufficiently large charge values, the jitter is less than 500 ps. The error bars are smaller than the marker size.

the `HitOr` signal that shifts the resulting curve in vertical direction, but has no impact on the interpretation of the results. Figure 7.20 schematically shows the setup used for the experiment.

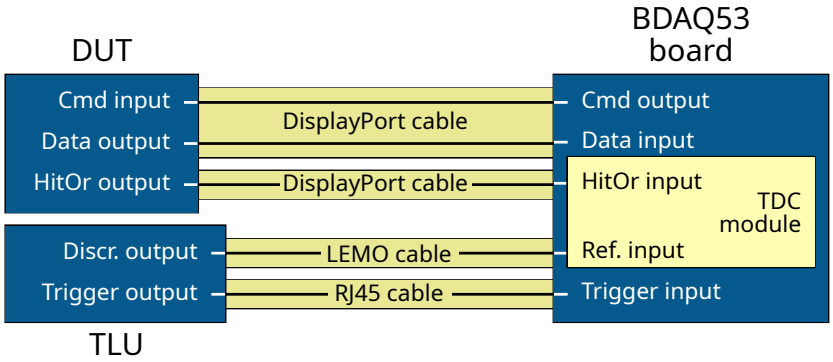

Figure 7.20: Setup for time walk measurements using a particle beam. The TLU outputs the discriminated signal from a scintillator in the beam which is used as reference time. Usually, the `HitOr` from the DUT has to be delayed in order to compensate for the discrimination of the scintillator signal in the TLU. This does not influence measurements as it only adds a constant offset.

During the analysis of the recorded data, multiple aspects of the measurement procedure have to be taken into account.

Association of `HitOr` and pixel data To increase the statistical precision, all pixels of the matrix are enabled, but only events with one cluster are selected for the analysis to eliminate possible ambiguities. The `HitOr` values (trigger delay and high-precision charge) corresponding to that trigger can then be assigned to the pixel hit with column and row information.

Cluster effects Due to the high average cluster size in TJ-Monopix2 (see Section 7.4.2), but

only a single available `HitOr` output, the high-precision charge measurement of the TDC module does not necessarily reflect the total deposited charge of the cluster. The measured trigger delay stems from the fastest hit. Only the seed pixel of a cluster is regarded which corresponds to the largest charge in the cluster, typically resulting in the fastest signal. The association of `HitOr` and position information is refined by restricting the analysis to only those hits for which the length of the `HitOr` signal matches the total duration of the cluster measured with the 40 MHz timestamp in each pixel.

Propagation delay For the `HitOr` propagation delay correction, the maximum trigger delay per pixel is used as data point for a linear fit along each column. Since the functional dependence between delay and row number is expected to be linear as it only depends on the used OR gate, the fit result describes the relationship reasonably well. An exemplary figure for this correction is shown in Figure A.2.

While the above considerations form the best available approach, there is still a chance of mismatching which can be observed in the results. The relationship between seed charge (in terms of time over threshold) and trigger delay before and after correction is shown in Figure 7.21. The general shape follows the one from Figure 7.16, but takes the charge spectrum from a MIP

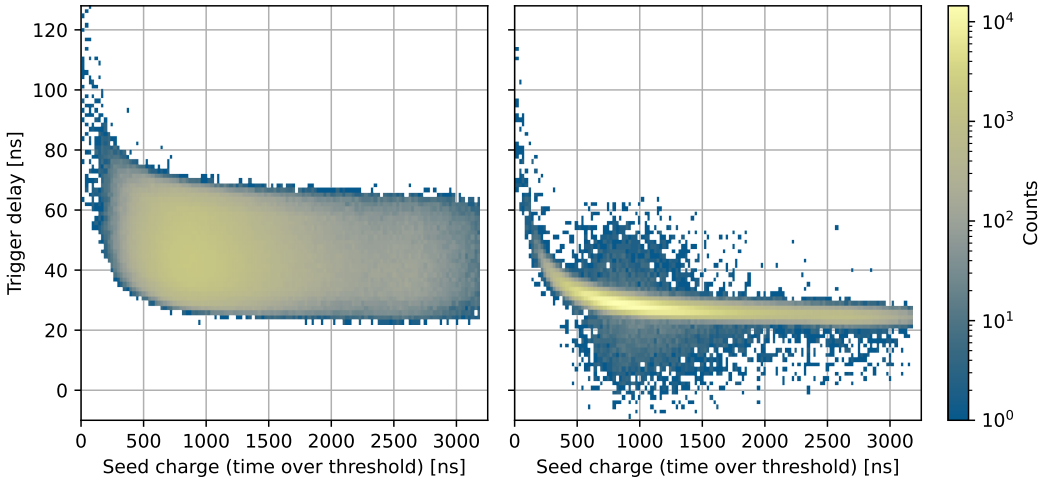

Figure 7.21: Time walk curve measured in a 5 GeV particle beam. Depicted is a non-irradiated epitaxial chip with n-gap modification. On the left is the uncorrected data, on the right the result after position-dependent correction of the delay. Outliers occur because of low number of hits in some columns and wrongly matched pixel and `HitOr` data.

into account. This leads both to fewer hits of small charges and a larger tail towards higher charges due to the underlying Landau distribution that extends further than the charge injection range. Noticeable outliers can occur due to low number of hits in some columns for the correction or due to mismatched pixel and `HitOr` data. However, the color scale in Figure 7.21 is logarithmic, and the background plays an insignificant role for the further analysis.

The in-time ratio, as defined in Section 4.2.3, is the percentage of hits that are registered within 25 ns with respect to the incident particle passing. Projecting the curve from Figure 7.21 onto the y-axis gives the trigger delay distribution which is independent of the deposited charge. It is visualized in Figure 7.22. It should be noted that the measurement is performed by sampling

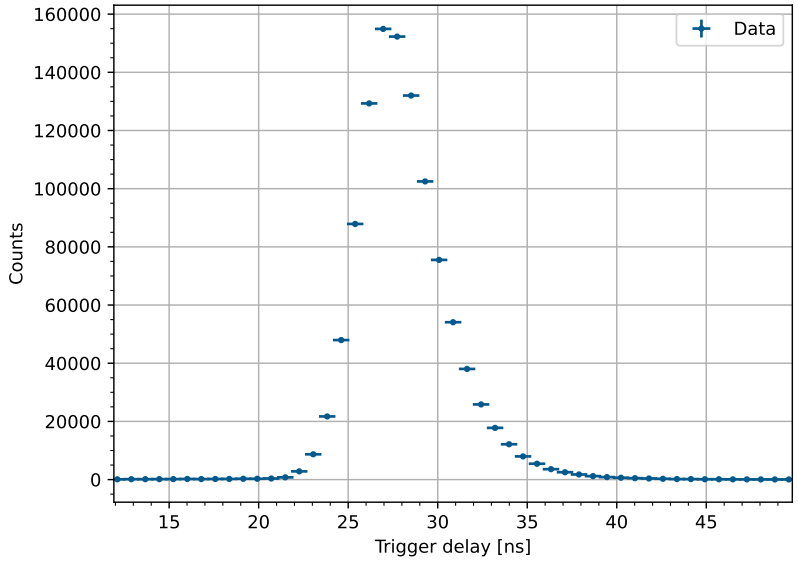

Figure 7.22: Distribution of the trigger delay between `HitOr` and scintillator hit in a 5 GeV electron beam for a non-irradiated epitaxial silicon sample with n-gap modification. Its asymmetric shape arises from time walk as depicted in Figure 7.24 that introduces long trigger delays for small charges.

the trigger delay with a 640 MHz clock. Therefore, the uncertainty is:

$$\sigma_{\mathrm{TDC}} = \frac{1}{640\,\mathrm{MHz}} \cdot \frac{1}{\sqrt{12}} = \frac{1.5625\,\mathrm{ns}}{\sqrt{12}} = 0.46\,\mathrm{ns}\,. \tag{7.11}$$

Due to the delay propagation correction that introduces floating point numbers instead of integer bins, the trigger delay can be sampled with smaller bins for illustration purposes, although the resolution remains the same. A more pronounced tail is visible on the right side of the maximum that originates from time walk, especially from small signals with large delay. While a quantitative approach with a fit is not useful due to the unknown functional relationship, it can be seen that the width of the distribution is less than 10 ns.

In a high-energy physics experiment, the trigger signal for the detector is typically distributed from a complex trigger system and is tuned such that the maximum amount of hits is read out. The time window for signal detection is set with respect to the initial interaction, e.g., collision of two particle bunches, to maximize the number of related hits that are read out. Due to this constraint, not only the detector performance in terms of hit efficiency, but also the time performance are of interest for characterization studies. Since no combined data with time information and tracking is available for this work, they are measured and analyzed

independently. From both measurements, the combined performance can be estimated to a good extent.

The distribution shown in Figure 7.22 is used to find the trigger delay for the maximum ratio of recorded hits. A window of 25 ns is slid across the distribution and for every step, the amount of entries within the 25 ns interval is computed. For the same epitaxial silicon sample as before, the resulting ratio versus the window position is depicted in Figure 7.23. In addition to the ATLAS requirement of 25 ns, the results for 15 ns and 20 ns are included. Because of

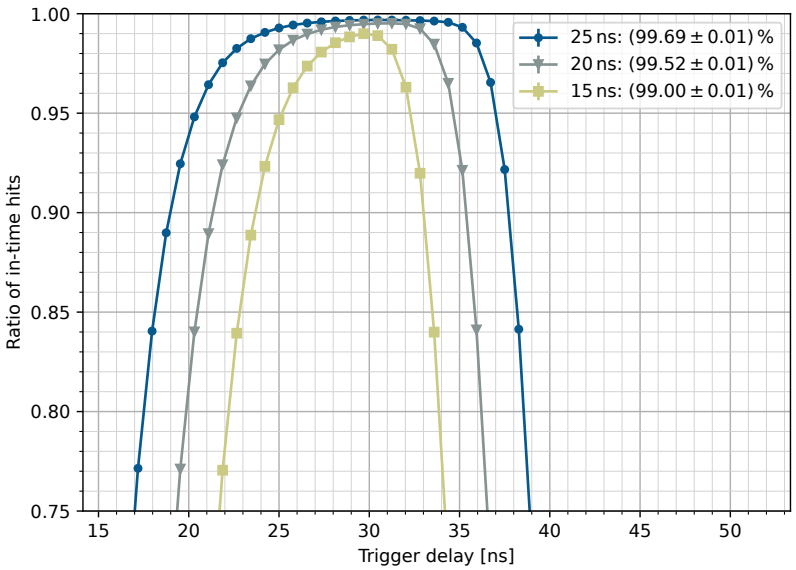

Figure 7.23: In-time ratios for the non-irradiated epitaxial silicon sample with n-gap modification and different time requirements.

the shape of the trigger delay distribution as in Figure 7.22, it is asymmetric with a steeper falling slope than the rising one. The results for all investigated samples of different substrate materials and front-end variations are summarized in Table 7.1. For the 25 ns time window,

Chip type	15 ns window [%]	20 ns window [%]	25 ns window [%]
epi (n-gap), DC std. front-end	99.00 ± 0.01	99.52 ± 0.01	99.69 ± 0.01
epi (n-gap), DC casc. front-end	99.25 ± 0.01	99.64 ± 0.01	99.76 ± 0.01
epi (n-gap), AC casc. front-end	98.00 ± 0.11	99.34 ± 0.06	99.69 ± 0.05
Cz (n-gap), DC std. front-end	97.45 ± 0.02	98.97 ± 0.01	99.38 ± 0.01
Cz (n-gap), DC casc. front-end	98.11 ± 0.02	99.12 ± 0.01	99.41 ± 0.01
Cz (n-gap), AC casc. front-end	95.30 ± 0.20	98.21 ± 0.13	99.23 ± 0.08

Table 7.1: Overview of achievable in-time ratios for different sensor materials and front-ends. None of the samples have been irradiated. The maximum value for the ATLAS specification of 25 ns time window is shown alongside the ones for 15 ns and 20 ns.

the in-time ratio is consistently larger than 99 %. It should be noted that the distribution as shown in Figure 7.22 still contains uncorrelated data that show up as outliers from the time walk curve depicted in Figure 7.21. Eliminating those could potentially increase the in-time ratio, although not on a significant level. In general, the in-time ratio is more stable for the epitaxial silicon chips than the Czochralski silicon ones when going to smaller time windows. A possible reason is the available depletion depth, that influences the time resolution as described in Section 4.2.3. Further discussion about the contributing factors and the depletion depth can be found in Section 7.3 and Section 7.5.4. With the hit detection efficiencies as reported in Section 7.4.3, 99.1 % to 99.7 % of hits are detected within 25 ns depending on the pixel flavor and substrate type.

7.5.4 Time resolution

The time resolution of TJ-Monopix2 is determined from the same measurement performed in Section 7.5.3. In order to calculate the achievable time resolution on a pixel level as opposed to an actual beam measurement as presented in Figure 7.22, the charge dependence has to be eliminated. Since the time walk contribution in (4.2) depends on the signal amplitude which is measured at the same time as the trigger delay, it can be corrected in the recorded data. While it is possible to perform the correction on a hardware or firmware level, the recorded data is corrected offline after data taking. The shape of the time walk curve is interpolated, and the trigger delay distribution of every amplitude bin is shifted accordingly. Figure 7.24 shows the corrected time walk curve. Depicted is the same data as in Figure 7.21. As expected, the charge dependence is mostly eliminated except for the small background of uncorrelated hits around the MPV and for small charges due to the limited statistics in those bins.

The resulting trigger delay distribution, depicted in Figure 7.25, is symmetric around the peak and follows a Gaussian shape. Because time walk effects are eliminated by the correction, its width is then described by:

$$\sigma_t^2 = \sigma_{\mathrm{TDC}}^2 + \sigma_{\mathrm{noise}}^2 + \sigma_{\mathrm{arrival}}^2 + \sigma_{\mathrm{distortion}}^2 \,. \tag{7.12}$$

A fit with a Gaussian function yields:

$$\sigma_t = (1.25 \pm 0.46)\,\mathrm{ns}\,. \tag{7.13}$$

As discussed before, the large uncertainty originates from the resolution of the TDC measurement that cannot be improved with the available equipment. The σ_{TDC} component in (7.12) is known and σ_{noise} has been measured in Section 7.5.2 which allows for calculation of the sensor-related contributions to the temporal resolution. For σ_{noise}, a value of 250 ps was used according to Figure 7.19, which is the upper limit for σ_{noise} based on the observed charge range

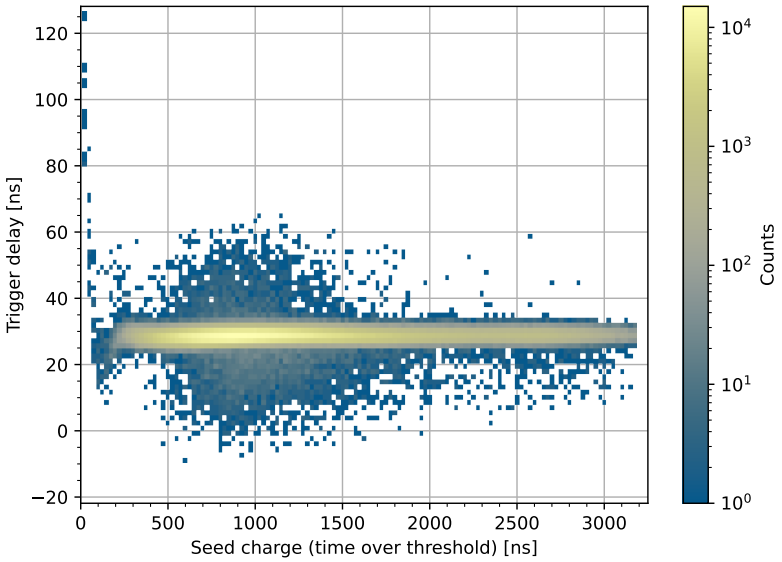

Figure 7.24: Two-dimensional histogram of the trigger delay versus signal amplitude after time walk correction. The curve is flat with no significant charge dependence. The behavior for small seed charges (below 200 ns, corresponding to a TOT value of 8) results from low statistics in those bins.

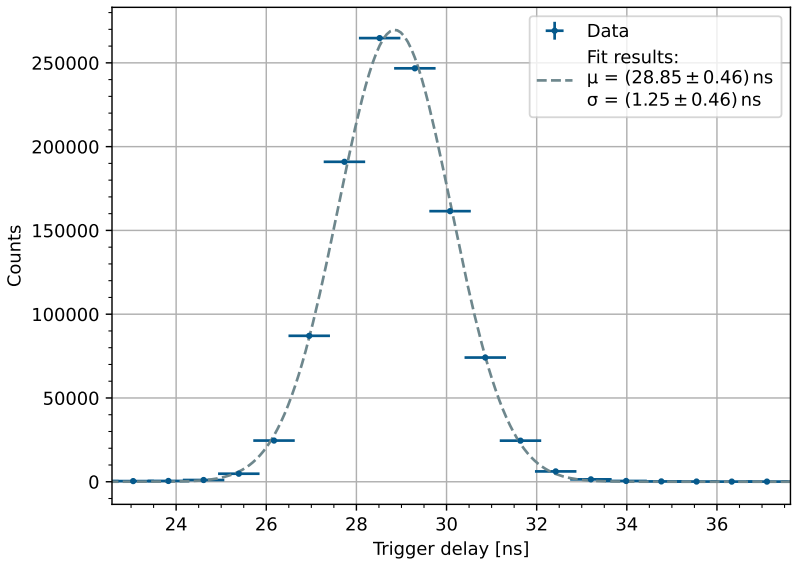

Figure 7.25: Trigger delay distribution for time walk and propagation delay corrected data of the non-irradiated epitaxial silicon chip with n-gap modification. The y-errors are too small to be visible, while the x-errors are dominated by the resolution of the available measurement device compared to the measured values. A Gaussian fit is used to extract the time resolution.

in 7.24. Subtracting these values in quadrature results in:

$$\sigma_t^{\text{corr}} = \sqrt{\sigma^2_{\text{arrival}} + \sigma^2_{\text{distortion}}} = (1.14 \pm 0.46)\,\text{ns}\,. \tag{7.14}$$

While this is not the total time residual of the pixel, the given value is the contribution to the time resolution arising from the electron-hole pair creation as discussed in Section 4.2.3. The unknown time resolution of the trigger scintillator (typically in the order of 0.1 ns) is also included in the result. Still, compared to the front-end resolution reported in 7.10, σ_{arrival} and $\sigma_{\text{distortion}}$ are the dominating factors to the total time resolution that can only be reduced by modifying the sensor in terms of geometry and weighting field shape. Measurements with tracking data in the related MALTA2 chip indicate an additional position dependency of trigger delay within the pixel cell [100] that supports this conclusion. Table 7.2 summarizes the time resolution after `HitOr` propagation delay and time-walk correction for epitaxial and Czochralski silicon samples and different front-end flavors. As in (7.14), the TDC and noise component are subtracted from the respective fit result to obtain the values given in Table 7.2. Additionally, the contribution from the trigger scintillator has been subtracted for which a typical value of 0.25 ns has been used. While the uncertainty is large compared to the measured values,

	Epitaxial silicon, n-gap [ns]	Czochralski silicon, n-gap [ns]
DC std. front-end	1.14 ± 0.46	1.50 ± 0.46
DC casc. front-end	1.16 ± 0.46	1.56 ± 0.46
AC casc. front-end	1.38 ± 0.46	1.89 ± 0.46

Table 7.2: Time resolution (propagation delay and time-walk corrected) for different substrates and front-end flavors. Contributions from the TDC, trigger scintillator and front-end are subtracted. For the time resolution of the trigger scintillator, a typical value of 0.25 ns has been used.

a tendency towards worse time resolution can be observed in the Czochralski silicon samples. This can potentially be attributed to the larger depletion depth as measured in Section 7.3. The variation of the charge deposition along the thickness of the device and consequently the time characteristic of the induced charge is expected to increase for thicker devices, where the contribution due to diffusion in the undepleted silicon is small. To a smaller extent and still within the uncertainty, the AC-coupled front-end indicates a worse time resolution. A possible explanation is a different electric field shape since the configuration of the applied bias differs (see Section 4.2.5 and Section 4.1.1).

In-depth studies are necessary to investigate the observed tendencies mentioned above. A more precise time-to-digital converter can reduce the uncertainty, which is limited by the available equipment for the presented measurements. It could allow to explicitly identify variations between the substrates and front-ends that are currently in agreement with each other within the stated uncertainties. Combining the trigger delay information with reconstructed tracks could additionally resolve a possible dependency of the impact position within the pixel. Albeit, for the application purpose under consideration, the measured time resolution and in-time ratio is well within the specifications.

8 Summary

Depleted monolithic active pixel sensors (DMAPS) are a recent development in the field of high-energy particle physics detectors, employing commercial CMOS technologies implemented in high-resistivity silicon. In the depleted sensor volume, charge is collected by drift in the electrical field that is substantial for radiation hardness and a fast signal, rendering the device capable of operation in high-radiation and high-rate environments such as the ATLAS ITk outer pixel layer. They do not require an interconnection assembly step and exhibit less material budget compared to hybrid pixel detectors, but to date they cannot meet the requirements for the harshest conditions such as the ITk innermost pixel layers. Additionally, the use of commercial processes offers fast turnaround times and high production capacity.

In this work, the radiation hardness of the TJ-Monopix1 DMAPS prototype with an enhanced sensor geometry over the original design has been studied. The experimental confirmation of the increased radiation tolerance led to the sensor geometry being adopted for the next prototype. TJ-Monopix2, with integrated readout logic, command-based communication, and encoded data stream, has been characterized in this thesis. The 2 cm × 2 cm chip consists of a 16.9 mm × 16.9 mm matrix composed of 512 × 512 square pixels with a pitch of 33.04 µm and a digital periphery at the chip bottom. Its small-collection-electrode design yields a power consumption of approximately 1 µW per pixel for the analog circuitry at a high signal-to-noise ratio, resulting in a typical operational threshold of 200 e^-. The equivalent noise charge of the front-end is around 6 e^-, which represents a significant improvement compared to the predecessor chip in the TJ-Monopix line. The hit detection efficiency of the sensor has been investigated for TJ-Monopix1 chips irradiated to a NIEL fluence of $10^{15}\,n_{eq}\,cm^{-2}$ in multiple beam test campaigns. For 30 µm and 100 µm highly resistive silicon, mean hit detection efficiencies of $(87.29 \pm 0.04_{sys} \pm 0.03_{stat})$ % and $(98.28 \pm 0.04_{sys} \pm 0.02_{stat})$ %, respectively, have been measured. Losses have been identified in cases of a small ratio of signal to threshold. Refining the electrical circuitry for TJ-Monopix2 results in a hit detection efficiency before irradiation between $(99.65 \pm 0.04_{sys} \pm 0.01_{stat})$ % and $(99.96 \pm 0.04_{sys} \pm 0.01_{stat})$ % for all tested samples, varying with the matrix flavor and thickness of the charge-sensitive layer. In combination with the tested radiation hardness of the sensor geometry as implemented in both iterations of TJ-Monopix, a hit detection efficiency larger than 99 % can be expected for TJ-Monopix2 at a NIEL fluence of $10^{15}\,n_{eq}\,cm^{-2}$. The time resolution of TJ-Monopix2 has been evaluated for its analog front-end and in conjunction with charge deposition in the sensor. The former achieves a resolution of down to (93.3 ± 0.1) ps for a charge less than the most probable value of a minimum-ionizing particle. Exploiting the charge

information of individual pixel hits, the charge dependency has been eliminated to quantify the time resolution. For minimum-ionizing particles, time resolutions as low as (1.14 ± 0.46) ns have been measured.

The obtained results show a good performance of TJ-Monopix2 and demonstrate its suitability for high-energy particle physics experiments. Studies with non-irradiated devices and the radiation hardness of the sensor geometry in TJ-Monopix1 suggest a radiation tolerance to NIEL fluences of at least $10^{15}\,\mathrm{n_{eq}\,cm^{-2}}$. While the experimental confirmation is still pending, there are advances for an integration of the TJ-Monopix2 design in particle physics experiments. The VTX collaboration is actively engaged in constructing an all-silicon tracking detector for an upgrade of the Belle II experiment [101] with a DMAPS derived from TJ-Monopix2. This research work contributed significant results to leverage the TJ-Monopix development line for fully integrated detector systems.

A Supplementary figures

A.1 Process modification for increased radiation hardness

Figure A.1 depicts the concentration of trapped charge carriers after 25 ns in a non-irradiated sensor with a geometry comparable to the one of TJ-Monopix.

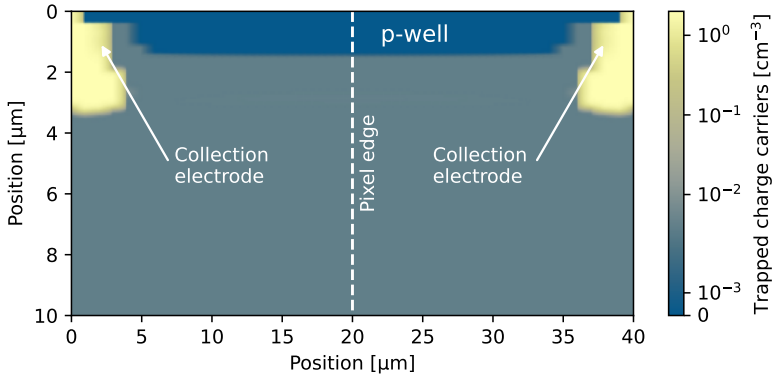

Figure A.1: TCAD simulation showing trapped charge carriers in the small-collection-electrode design after 25 ns before irradiation. The geometry and doping are comparable values to those of TJ-Monopix1. Yellow areas on the edges are the locations of the charge collection electrodes. Notably, the color scale is different from the one in Figure 4.2. Reproduced with data from [70].

A.2 Timing measurements

Figure A.2 exemplarily shows the `HitOr` propagation delay along one column. The slope of the line fit yields a delay of 86.4 ps delay per row, i.e. the delay of the implemented logical `OR`.

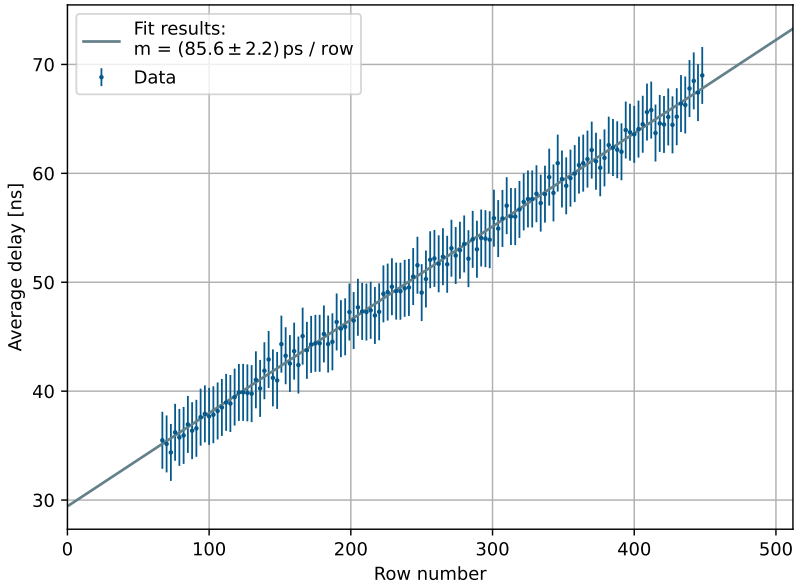

Figure A.2: Average propagation delay of the `HitOr` signal for a single column versus the row number. A column-wise line fit is used to correct the delay based on the pixel position in the matrix. Not all rows are enabled in the scan.

Bibliography

[1] H. Bethe. "Zur Theorie des Durchgangs schneller Korpuskularstrahlen durch Materie." In: *Annalen der Physik* 397.3 (1930), pp. 325–400. DOI: 10.1002/andp.19303970303.

[2] F. Bloch. "Zur Bremsung rasch bewegter Teilchen beim Durchgang durch Materie." In: *Ann. Phys.* 408.3 (Jan. 1933), pp. 285–320. DOI: 10.1002/andp.19334080303.

[3] R. L. Workman et al. "Review of Particle Physics." In: *PTEP* 2022 (2022), p. 083C01. DOI: 10.1093/ptep/ptac097.

[4] Hermann Kolanoski and Norbert Wermes. *Particle Detectors: Fundamentals and Applications*. Oxford University Press, June 2020. DOI: 10.1093/oso/9780198858362.001.0001.

[5] M.J. Berger et al. *ESTAR, PSTAR, and ASTAR: Computer Programs for Calculating Stopping-Power and Range Tables for Electrons, Protons, and Helium Ions*. Version 1.2.3. National Institute of Standards and Technology, Gaithersburg, MD. 2005. (Visited on May 11, 2023).

[6] W. Heitler. *The Quantum Theory of Radiation*. International series of monographs on physics. Oxford University Press, 1944.

[7] Enrico Fermi. "The Ionization Loss of Energy in Gases and in Condensed Materials." In: *Phys. Rev.* 57 (6 Mar. 1940), pp. 485–493. DOI: 10.1103/PhysRev.57.485.

[8] Claude Leroy and Pier-Giorgio Rancoita. *Principles of radiation interaction in matter and detection*. 2nd ed. Singapore: World Scientific, 2009.

[9] Lev Davidovich Landau. "On the energy loss of fast particles by ionization." In: *J. Phys.* 8.4 (1944), pp. 201–205.

[10] M.J. Berger et al. *XCOM: Photon Cross Sections Database*. National Institutue of Standards and Technology. DOI: 10.18434/T48G6X.

[11] O. Klein and Y. Nishina. "Über die Streuung von Strahlung durch freie Elektronen nach der neuen relativistischen Quantendynamik von Dirac." In: *Zeitschrift für Physik* 52.11 (1929), pp. 853–868. DOI: 10.1007/BF01366453.

[12] H. Bethe and W. Heitler. "On the stopping of fast particles and on the creation of positive electrons." In: *Proc. R. Soc. Lond.* 146 (856 1934), pp. 83–112. DOI: 10.1098/rspa.1934.0140.

[13] Gert Moliere. "Theorie der Streuung schneller geladener Teilchen II Mehrfach- und Vielfachstreuung." In: *Zeitschrift für Naturforschung A* 3.2 (1948), pp. 78–97. DOI: 10.1515/zna-1948-0203.

[14] Gerald R. Lynch and Orin I. Dahl. "Approximations to multiple Coulomb scattering." In: *Nuclear Instruments and Methods in Physics Research Section B: Beam Interactions with Materials and Atoms* 58.1 (1991), pp. 6–10. DOI: 10.1016/0168-583X(91)95671-Y.

[15] J.-P. Colinge and C.A. Colinge. *Physics of Semiconductor Devices*. Springer, 2005.

[16] Robert F. Pierret. *Advanced Semiconductor Fundamentals*. 2nd Edition. Prentice Hall, 2002.

[17] Rolf Enderlein and Norman J. M. Horing. *Fundamentals of semiconductor physics and devices*. World Scientific, 1997.

[18] W. Shockley. "The Theory of p-n Junctions in Semiconductors and p-n Junction Transistors." In: *Bell System Technical Journal* 28.3 (1949), pp. 435–489. DOI: 10.1002/j.1538-7305.1949.tb03645.x.

[19] D.M. Caughey and R.E. Thomas. "Carrier mobilities in silicon empirically related to doping and field." In: *Proceedings of the IEEE* 55.12 (1967), pp. 2192–2193. DOI: 10.1109/PROC.1967.6123.

[20] Adolf Fick. "Ueber Diffusion." In: *Annalen der Physik* 170.1 (1855), pp. 59–86. DOI: 10.1002/andp.18551700105.

[21] Ken A. Dill and Sarina Bromberg. *Molecular Driving Forces: Statistical Thermodynamics in Biology, Chemistry, Physics, and Nanoscience*. 2nd ed. Garland Science, 2010.

[22] W. Shockley. "Currents to Conductors Induced by a Moving Point Charge." In: *Journal of Applied Physics* 9.10 (May 1938), pp. 635–636. DOI: 10.1063/1.1710367.

[23] S. Ramo. "Currents Induced by Electron Motion." In: *Proceedings of the IRE* 27.9 (1939), pp. 584–585. DOI: 10.1109/JRPROC.1939.228757.

[24] David-Leon Pohl. *Scarce*. 2017. URL: https://github.com/SiLab-Bonn/Scarce (visited on Aug. 15, 2024).

[25] Zhong He. "Review of the Shockley–Ramo theorem and its application in semiconductor gamma-ray detectors." In: *Nuclear Instruments and Methods in Physics Research Section A: Accelerators, Spectrometers, Detectors and Associated Equipment* 463.1 (2001), pp. 250–267. DOI: 10.1016/S0168-9002(01)00223-6.

[26] Claude Leroy and Pier-Giorgio Rancoita. "Particle interaction and displacement damage in silicon devices operated in radiation environments." In: *Reports on Progress in Physics* 70.4 (2007), p. 493. DOI: 10.1088/0034-4885/70/4/R01.

[27] K. Iniewski. *Radiation Effects in Semiconductors*. CRC Press, 2011. DOI: 10.1201/9781315217864.

[28] Viktor S. Vavilov and Nikolaj A. Uchin. *Radiation effects in semiconductors and semiconductor devices*. New York: Consultants Bureau, 1977.

[29] C. Claeys and E. Simoen. *Radiation Effects in Advanced Semiconductor Materials and Devices*. Springer, 2002. DOI: 10.1007/978-3-662-04974-7.

[30] W. Shockley and W. T. Read. "Statistics of the Recombinations of Holes and Electrons." In: *Phys. Rev.* 87 (5 Sept. 1952), pp. 835–842. DOI: 10.1103/PhysRev.87.835.

[31] R. N. Hall. "Electron-Hole Recombination in Germanium." In: *Phys. Rev.* 87 (2 July 1952), pp. 387–387. DOI: 10.1103/PhysRev.87.387.

[32] D. Pitzl et al. "Type inversion in silicon detectors." In: *Nuclear Instruments and Methods in Physics Research Section A: Accelerators, Spectrometers, Detectors and Associated Equipment* 311.1 (1992), pp. 98–104. DOI: 10.1016/0168-9002(92)90854-W.

[33] Jacobi Werner. "Halbleiterverstärker." DE833366C. Siemens AG. June 30, 1952.

[34] F. Wanlass and C. Sah. "Nanowatt logic using field-effect metal-oxide semiconductor triodes." In: *1963 IEEE International Solid-State Circuits Conference. Digest of Technical Papers*. Vol. VI. 1963, pp. 32–33. DOI: 10.1109/ISSCC.1963.1157450.

[35] B. Hyams et al. "A silicon counter telescope to study short-lived particles in high-energy hadronic interactions." In: *Nuclear Instruments and Methods in Physics Research* 205.1 (1983), pp. 99–105. DOI: 10.1016/0167-5087(83)90177-1.

[36] Arturo Rodriguez Rodriguez. *The ATLAS Strip Detector System for the High-Luminosity LHC*. Tech. rep. Geneva: CERN, 2020. URL: https://cds.cern.ch/record/2718001.

[37] J.-L Agram et al. "The silicon sensors for the Compact Muon Solenoid tracker-design and qualification procedure." In: *Nuclear Instruments and Methods in Physics Research Section A: Accelerators, Spectrometers, Detectors and Associated Equipment* 517.1 (2004), pp. 77–93. DOI: 10.1016/j.nima.2003.08.175.

[38] A. Ahmad et al. "The silicon microstrip sensors of the ATLAS semiconductor tracker." In: *Nuclear Instruments and Methods in Physics Research Section A: Accelerators, Spectrometers, Detectors and Associated Equipment* 578.1 (2007), pp. 98–118. DOI: 10.1016/j.nima.2007.04.157.

[39] S. Albergo, A. Alberigi, and Erik H. M. Heijne. *RD19: status report on activities in 1996-1997. Development of hybrid and monolithic semiconductor micropattern pixel detectors*. Tech. rep. Geneva: CERN, 1997. URL: http://cds.cern.ch/record/345010.

[40] M. Mironova and on behalf of the RD53 collaboration. "X-ray irradiation measurements of the radiation tolerance of the ITkPixV1 ATLAS pixel readout chip." In: *Journal of Instrumentation* 17.02 (Feb. 2022), p. C02028. DOI: 10.1088/1748-0221/17/02/C02028.

[41] J. Lange et al. “Radiation hardness of small-pitch 3D pixel sensors up to a fluence of 3×1016 neq/cm2.” In: *Journal of Instrumentation* 13.09 (Sept. 2018), P09009. DOI: 10.1088/1748-0221/13/09/P09009.

[42] Sherwood Parker. “A proposed VLSI pixel device for particle detection.” In: *Nuclear Instruments and Methods in Physics Research Section A: Accelerators, Spectrometers, Detectors and Associated Equipment* 275.3 (1989), pp. 494–516. DOI: 10.1016/0168-9002(89)90736-5.

[43] W. Snoeys et al. “A new integrated pixel detector for high energy physics.” In: *IEEE Transactions on Nuclear Science* 39.5 (1992), pp. 1263–1269. DOI: 10.1109/23.173188.

[44] R. Turchetta et al. “A monolithic active pixel sensor for charged particle tracking and imaging using standard VLSI CMOS technology.” In: *Nuclear Instruments and Methods in Physics Research Section A: Accelerators, Spectrometers, Detectors and Associated Equipment* 458.3 (2001), pp. 677–689. DOI: 10.1016/S0168-9002(00)00893-7.

[45] L. Greiner et al. “A MAPS based vertex detector for the STAR experiment at RHIC.” In: *Nuclear Instruments and Methods in Physics Research Section A: Accelerators, Spectrometers, Detectors and Associated Equipment* 650.1 (2011). International Workshop on Semiconductor Pixel Detectors for Particles and Imaging 2010, pp. 68–72. DOI: 10.1016/j.nima.2010.12.006.

[46] M. Mager. “ALPIDE, the Monolithic Active Pixel Sensor for the ALICE ITS upgrade.” In: *Nuclear Instruments and Methods in Physics Research Section A: Accelerators, Spectrometers, Detectors and Associated Equipment* 824 (2016). Frontier Detectors for Frontier Physics: Proceedings of the 13th Pisa Meeting on Advanced Detectors, pp. 434–438. DOI: 10.1016/j.nima.2015.09.057.

[47] Ivan Perić. “A novel monolithic pixelated particle detector implemented in high-voltage CMOS technology.” In: *Nuclear Instruments and Methods in Physics Research Section A: Accelerators, Spectrometers, Detectors and Associated Equipment* 582.3 (2007). VERTEX 2006, pp. 876–885. DOI: 10.1016/j.nima.2007.07.115.

[48] Sinuo Zhang et al. “Breakdown performance of guard ring designs for pixel detectors in 150 nm CMOS technology.” In: *Nuclear Instruments and Methods in Physics Research Section A: Accelerators, Spectrometers, Detectors and Associated Equipment* 1063 (2024), p. 169287. DOI: 10.1016/j.nima.2024.169287.

[49] Andre Schoening et al. “MuPix & ATLASpix: Architectures and Results.” In: *Proceedings of The 28th International Workshop on Vertex Detectors — PoS(Vertex2019)*. Vol. 373. 2020, p. 024. DOI: 10.22323/1.373.0024.

[50] P. Sieberer et al. “RD50-MPW3: a fully monolithic digital CMOS sensor for future tracking detectors.” In: *Journal of Instrumentation* 18.02 (Feb. 2023), p. C02061. DOI: 10.1088/1748-0221/18/02/C02061.

[51] E.J. Schioppa et al. "Measurement results of the MALTA monolithic pixel detector." In: *Nuclear Instruments and Methods in Physics Research Section A: Accelerators, Spectrometers, Detectors and Associated Equipment* 958 (2020). Proceedings of the Vienna Conference on Instrumentation 2019, p. 162404. DOI: 10.1016/j.nima.2019.162404.

[52] Piotr Rymaszewski et al. "Development of Depleted Monolithic Pixel Sensors in 150 nm CMOS technology for the ATLAS Inner Tracker Upgrade." In: *Proceedings of Topical Workshop on Electronics for Particle Physics — PoS(TWEPP-17)*. Vol. 313. 2018, p. 045. DOI: 10.22323/1.313.0045.

[53] T. Noulis et al. "Noise Analysis of Radiation Detector Charge Sensitive Amplifier Architectures." In: (2008). DOI: 10.5170/CERN-2008-008.486.

[54] I. Caicedo et al. "Development and testing of a radiation-hard large-electrode DMAPS design in a 150 nm CMOS process." In: *Nuclear Instruments and Methods in Physics Research Section A: Accelerators, Spectrometers, Detectors and Associated Equipment* 1040 (2022), p. 167224. DOI: 10.1016/j.nima.2022.167224.

[55] T. Wang et al. "Development of a Depleted Monolithic CMOS Sensor in a 150 nm CMOS Technology for the ATLAS Inner Tracker Upgrade." In: *Journal of Instrumentation* 12.01 (Jan. 2017), p. C01039. DOI: 10.1088/1748-0221/12/01/C01039.

[56] Miroslav Havránek et al. "Measurement of pixel sensor capacitances with sub-femtofarad precision." In: *Nuclear Instruments and Methods in Physics Research Section A: Accelerators, Spectrometers, Detectors and Associated Equipment* 714 (2013), pp. 83–89. DOI: 10.1016/j.nima.2013.02.038.

[57] Toko Hirono et al. "Depleted fully monolithic active CMOS pixel sensors (DMAPS) in high resistivity 150 nm technology for LHC." In: *Nuclear Instruments and Methods in Physics Research Section A: Accelerators, Spectrometers, Detectors and Associated Equipment* 924 (2019). 11th International Hiroshima Symposium on Development and Application of Semiconductor Tracking Detectors, pp. 87–91. DOI: 10.1016/j.nima.2018.10.059.

[58] Jacobus Willem van Hoorne. "The upgrade of the ALICE Inner Tracking System - Status of the R&D on monolithic silicon pixel sensors." In: *Proceedings of Technology and Instrumentation in Particle Physics 2014 — PoS(TIPP2014)*. Vol. 213. 2015, p. 125. DOI: 10.22323/1.213.0125.

[59] Konstantinos Moustakas. "Design and Development of Depleted Monolithic Active Pixel Sensors with Small Collection Electrode for High-Radiation Applications." PhD thesis. Rheinische Friedrich-Wilhelms-Universität Bonn, Sept. 2021. URL: https://hdl.handle.net/20.500.11811/9315.

[60] B. Abelev et al (The ALICE Collaboration). “Technical Design Report for the Upgrade of the ALICE Inner Tracking System.” In: *Journal of Physics G: Nuclear and Particle Physics* 41.8 (July 2014), p. 087002. DOI: 10.1088/0954-3899/41/8/087002.

[61] T. Kugathasan et al. “Explorer-0: A Monolithic Pixel Sensor in a 180 nm CMOS process with an 18 µm thick high resistivity epitaxial layer.” In: *2013 IEEE Nuclear Science Symposium and Medical Imaging Conference (2013 NSS/MIC)*. 2013, pp. 1–5. DOI: 10.1109/NSSMIC.2013.6829476.

[62] C. Cavicchioli et al. “Design and characterization of novel monolithic pixel sensors for the ALICE ITS upgrade.” In: *Nuclear Instruments and Methods in Physics Research Section A: Accelerators, Spectrometers, Detectors and Associated Equipment* 765 (2014). HSTD-9 2013 - Proceedings of the 9th International "Hiroshima" Symposium on Development and Application of Semiconductor Tracking Detectors, pp. 177–182. DOI: 10.1016/j.nima.2014.05.027.

[63] P. Yang et al. “MAPS development for the ALICE ITS upgrade.” In: *Journal of Instrumentation* 10.03 (Mar. 2015), p. C03030. DOI: 10.1088/1748-0221/10/03/C03030.

[64] W. Snoeys et al. “A process modification for CMOS monolithic active pixel sensors for enhanced depletion, timing performance and radiation tolerance.” In: *Nuclear Instruments and Methods in Physics Research Section A: Accelerators, Spectrometers, Detectors and Associated Equipment* 871 (2017), pp. 90–96. DOI: 10.1016/j.nima.2017.07.046.

[65] Ruth Magdalena Muenker. “Test beam and simulation studies on High Resistivity CMOS pixel sensors.” PhD thesis. Rheinische Friedrich-Wilhelms-Universität Bonn, Sept. 2018. URL: https://hdl.handle.net/20.500.11811/7634.

[66] Bojan Hiti et al. “Development of the monolithic "MALTA" CMOS sensor for the ATLAS ITK outer pixel layer.” In: *Proceedings of Topical Workshop on Electronics for Particle Physics — PoS(TWEPP2018)*. Norbert: Sissa Medialab, May 21, 2019. DOI: 10.22323/1.343.0155.

[67] I. Caicedo et al. “The Monopix chips: depleted monolithic active pixel sensors with a column-drain read-out architecture for the ATLAS Inner Tracker upgrade.” In: *Journal of Instrumentation* 14.06 (June 2019), p. C06006. DOI: 10.1088/1748-0221/14/06/C06006.

[68] R. Cardella et al. “MALTA: an asynchronous readout CMOS monolithic pixel detector for the ATLAS High-Luminosity upgrade.” In: *Journal of Instrumentation* 14.06 (June 2019), p. C06019. DOI: 10.1088/1748-0221/14/06/C06019.

[69] M. Munker et al. “Simulations of CMOS pixel sensors with a small collection electrode, improved for a faster charge collection and increased radiation tolerance.” In: *Journal of Instrumentation* 14.05 (May 2019), p. C05013. DOI: 10.1088/1748-0221/14/05/C05013.

[70] Sinou Zhang. “Charge Collection Efficiency Simulation of Irradiated Monolithic Silicon Pixel Detectors with TCAD.” MA thesis. University of Bonn, 2019.

[71] D. Kim et al. "Front end optimization for the monolithic active pixel sensor of the ALICE Inner Tracking System upgrade." In: *Journal of Instrumentation* 11.02 (Feb. 2016), p. C02042. DOI: 10.1088/1748-0221/11/02/C02042.

[72] C. Gao et al. "A novel source–drain follower for monolithic active pixel sensors." In: *Nuclear Instruments and Methods in Physics Research Section A: Accelerators, Spectrometers, Detectors and Associated Equipment* 831 (2016). Proceedings of the 10th International "Hiroshima" Symposium on the Development and Application of Semiconductor Tracking Detectors, pp. 147–155. DOI: 10.1016/j.nima.2016.03.074.

[73] Marco Ferrero et al. *An Introduction to Ultra-Fast Silicon Detectors*. CRC Press, July 7, 2021. DOI: 10.1201/9781003131946.

[74] W. Snoeys. "Monolithic pixel detectors for high energy physics." In: *Nuclear Instruments and Methods in Physics Research Section A: Accelerators, Spectrometers, Detectors and Associated Equipment* 731 (2013). PIXEL 2012, pp. 125–130. DOI: 10.1016/j.nima.2013.05.073.

[75] Zhong Yuan Chang and Willy M. C. Sansen. *Low-Noise Wide-Band Amplifiers in Bipolar and CMOS Technologies*. 1st ed. The Springer International Series in Engineering and Computer Science. Springer New York, NY, Mar. 9, 2013. DOI: 10.1007/978-1-4757-2126-3.

[76] Michael Athanassios Karagounis. "Analog integrated CMOS Circuits for the readout and powering of highly segmented detectors in particle physics applications." en. PhD thesis. Hagen, 2010. URL: https://ub-deposit.fernuni-hagen.de/receive/mir_mods_00000029.

[77] Roberto Cardella et al. "LAPA, a 5 Gb/s modular pseudo-LVDS driver in 180 nm CMOS with capacitively coupled pre-emphasis." In: *Proceedings of Topical Workshop on Electronics for Particle Physics — PoS(TWEPP-17)*. Sissa Medialab, Mar. 5, 2018. DOI: 10.22323/1.313.0038.

[78] A. X. Widmer and P. A. Franaszek. "A DC-Balanced, Partitioned-Block, 8B/10B Transmission Code." In: *IBM Journal of Research and Development* 27.5 (1983), pp. 440–451. DOI: 10.1147/rd.275.0440.

[79] Maurice Garcia-Sciveres, Flavio Loddo, and Jorgen Christiansen. *RD53B Manual*. Tech. rep. Geneva: CERN, 2019. URL: http://cds.cern.ch/record/2665301.

[80] Ivan Perić et al. "The FEI3 readout chip for the ATLAS pixel detector." In: *Nuclear Instruments and Methods in Physics Research Section A: Accelerators, Spectrometers, Detectors and Associated Equipment* 565.1 (2006). Proceedings of the International Workshop on Semiconductor Pixel Detectors for Particles and Imaging, pp. 178–187. DOI: 10.1016/j.nima.2006.05.032.

[81] M. Daas et al. "BDAQ53, a versatile pixel detector readout and test system for the ATLAS and CMS HL-LHC upgrades." In: *Nuclear Instruments and Methods in Physics Research Section A: Accelerators, Spectrometers, Detectors and Associated Equipment* 986 (2021), p. 164721. DOI: 10.1016/j.nima.2020.164721.

[82] Silizium Labor Bonn. *basil - A data acquisition framework in Python and Verilog.* Version 3.2.1dev0. 2023. URL: https://github.com/SiLab-Bonn/basil (visited on Aug. 15, 2024).

[83] Tomohisa Uchida. "Hardware-Based TCP Processor for Gigabit Ethernet." In: *IEEE Transactions on Nuclear Science* 55.3 (2008), pp. 1631–1637. DOI: 10.1109/TNS.2008.920264.

[84] I. Rubinskiy. "An EUDET/AIDA Pixel Beam Telescope for Detector Development." In: *Physics Procedia* 37 (2012), pp. 923–931. DOI: 10.1016/j.phpro.2012.02.434.

[85] Pascal Wolf. "Testing and extending a Python-based readout system for a high-resolution pixel detector telescope." Universität Bonn, Sept. 2016.

[86] J. Baudot et al. "First test results Of MIMOSA-26, a fast CMOS sensor with integrated zero suppression and digitized output." In: *2009 IEEE Nuclear Science Symposium Conference Record (NSS/MIC)*. 2009, pp. 1169–1173. DOI: 10.1109/NSSMIC.2009.5402399.

[87] Hendrik Jansen et al. "Performance of the EUDET-type beam telescopes." In: *EPJ Techniques and Instrumentation* 3.1 (2016), p. 7. DOI: 10.1140/epjti/s40485-016-0033-2.

[88] M. Garcia-Sciveres et al. "The FE-I4 pixel readout integrated circuit." In: *Nuclear Instruments and Methods in Physics Research Section A: Accelerators, Spectrometers, Detectors and Associated Equipment* 636.1, Supplement (2011), S155–S159. DOI: 10.1016/j.nima.2010.04.101.

[89] Marlon Barbero. "FE-I4 pixel readout chip and IBL module." In: *Proceedings of The 20th Anniversary International Workshop on Vertex Detectors — PoS(Vertex 2011)*. Vol. 137. 2012, p. 038. DOI: 10.22323/1.137.0038.

[90] David Cussans. *Description of the JRA1 Trigger Logic Unit (TLU), v0.2c.* Sept. 11, 2009. URL: https://www.eudet.org/e26/e28/e42441/e57298/EUDET-MEMO-2009-04.pdf (visited on Aug. 9, 2023).

[91] R. Diener et al. "The DESY II test beam facility." In: *Nuclear Instruments and Methods in Physics Research Section A: Accelerators, Spectrometers, Detectors and Associated Equipment* 922 (2019), pp. 265–286. DOI: 10.1016/j.nima.2018.11.133.

[92] Houdaifa Lahbil. "Charakterisierung und Optimierung eines Stickstoffkühlsystems für Detektortestanwendungen." Bachelor's thesis. Universität Bonn, Dec. 2022.

[93] Yannick Dieter, Jens Janssen, and David-Leon Pohl. *Beam Telescope Analysis.* 2023. URL: https://github.com/SiLab-Bonn/beam_telescope_analysis (visited on Aug. 15, 2024).

[94] Yannick Dieter. "Development and Characterisation of Passive CMOS Sensors for Pixel Detectors in High Radiation Environments." PhD thesis. Rheinische Friedrich-Wilhelms-Universität Bonn, Oct. 2022. URL: https://hdl.handle.net/20.500.11811/10346.

[95] Eric O. Lebigot. *Uncertainties: a Python package for calculations with uncertainties*. Version 3.1.7. June 19, 2022. URL: https://github.com/lebigot/uncertainties (visited on Aug. 15, 2024).

[96] David-Leon Pohl. "3D-Silicon and Passive CMOS Sensors for Pixel Detectors in High Radiation Environments." PhD thesis. Rheinische Friedrich-Wilhelms-Universität Bonn, Oct. 2020. URL: https://hdl.handle.net/20.500.11811/8743.

[97] M. Dyndal et al. "Mini-MALTA: radiation hard pixel designs for small-electrode monolithic CMOS sensors for the High Luminosity LHC." In: *Journal of Instrumentation* 15.02 (Feb. 2020), P02005. DOI: 10.1088/1748-0221/15/02/P02005.

[98] Luka Snoj, Gašper Žerovnik, and Andrej Trkov. "Computational analysis of irradiation facilities at the JSI TRIGA reactor." In: *Applied Radiation and Isotopes* 70.3 (2012), pp. 483–488. DOI: 10.1016/j.apradiso.2011.11.042.

[99] Hans Bichsel. "Straggling in thin silicon detectors." In: *Rev. Mod. Phys.* 60 (3 July 1988), pp. 663–699. DOI: 10.1103/RevModPhys.60.663.

[100] Milou van Rijnbach et al. "Performance of the MALTA telescope." In: *The European Physical Journal C* 83.7 (2023), p. 581. DOI: 10.1140/epjc/s10052-023-11760-z.

[101] Francesco Forti. *Snowmass Whitepaper: The Belle II Detector Upgrade Program*. 2022. DOI: 10.48550/arXiv.2203.11349.

List of Figures

List of Tables

Acronyms

CMOS complementary metal-oxide-semiconductor.

DAC digital-to-analog converter.

DAQ data acquisition.

DMAPS depleted monolithic active pixel sensor.

DUT device under test.

ENC equivalent noise charge.

ITk (ATLAS) Inner Tracker detector.

LHC Large Hadron Collider.

LVDS low voltage differential signaling.

MIP minimum-ionizing particle.

MPV most probable value.

NIEL non-ionizing energy loss.

PCB printed circuit board.

TDC time-to-digital converter.

TLU trigger logic unit.

TOT time over threshold.

Acknowledgments

I would like to express my gratitude to Jochen Dingfelder, who gave me the opportunity to do research and write this thesis in his working group. He provided an environment that allowed me to make my own decisions and offered support for all the problems that came up. Additionally, I want to thank Florian Bernlochner for taking over the role of my second advisor.

A lot of my work was only possible thanks to the many people who provided their expertise and skills, be it wirebonding sensors, ordering computer parts, or thinking of how to make a portable cooling system for test beams. The fact that all the technicians and "helping hands" are always open for questions and propose good solutions or input is an invaluable benefit that let me focus on my actual research.

My journey in the Silab started with my Bachelor's thesis and David-Leon Pohl who supervised me during that time. It is not by chance that I returned for my Master's thesis and stayed for my PhD; it is because of the people I shared time with and the memories I made along the way. I cannot list every name from the many years that I am part of Silab, but want to explicitly mention my long-time office partners and partners in (Monopix-) crime, Ivan, Lars and Toko. Tomek taught me a lot about digital electronics and chip characterization and, in addition, provided me with some life lessons. I want to express my deepest appreciation to the Silab crew, Botho, Georgios, Ivan, Jannes, Lars, Niko, Pascal, Patrick, and Yannick. You are the people that I "grew up" with over the years, and who I will not forget, no matter if you already moved on or still gather around the coffee machine twice a day. It is not only the technical (and not so technical) discussions during work, during lunch breaks, and our free time that I cherished, but I made great memories with every one of you over a drink, at a birthday celebration, or even when vacationing together. I would not want to miss any part of it. A special mention goes out to Yannick. In total, we spent many months at DESY for test beams, from early mornings to late at night. No matter how exhausting the hours got over each test beam campaign, I enjoyed both the so-called test beam madness that one inevitably runs into, and the steak nights and darts watch parties. Thank you for making these times worthwhile!

Last but not least, I want to thank my friends, my girlfriend, my family, and especially my parents for supporting me from the very beginning. Ihr habt mir erlaubt, diesen Weg einzuschlagen, mich motiviert, wenn es nötig war, und meine beruflichen Entscheidungen nie in Frage gestellt. Danke!